Geometry and Material Nonlinearity Effects on Static and Dynamics Performance of MEMS

M. Amin Changizi

A Thesis

In

The Department Of Mechanical and Industrial Engineering

Presented in Partial Fulfillment of the Requirements

For the Degree of Doctor of Philosophy (Mechanical Engineering)

Concordia University

Montreal, Quebec, Canada

2011

CONCORDIA UNIVERSITY
SCHOOL OF GRADUATE
STUDIES

This is to certify that the thesis prepared

By: M.Amin Changizi

Entitled: Geometry and Material Nonlinearity Effects on Static and Dynamics Performance of MEMS

and submitted in partial fulfillment of the requirements for the degree of

complies with the regulations of the University and meets the accepted standards with respect to originality and quality.

Signed by the final examining committee:

Dr. Brigitte Jaumard	Chair
Dr. Dan Neculescu	External Examiner
Dr. Yousef Shayan	External to Program
Dr. Rama B.Bhat	Examiner
Dr. A.K. Waizuddin Ahmed	Examiner
Dr. Ion Stiharu	Thesis Supervisor

Approved by

Dr. Martin Pugh
Chair of Department or Graduate Program Director

Dr. Rabin Drew
Dean of Faculty

Abstract

Geometry and Material Nonlinearity Effects on Static and Dynamic Performance of MEMS

M. Amin Changizi, Ph.D.
Concordia University, 2011

Nonlinear behavior of micro-mechanical systems is an interesting and little explored area of research. Although, micro-system technologies is new and fast developing area, there is little work carried out on modeling and simulation of MEMS devices which concerns their non-linear behavior. Nonlinear modeling of MEMS devices is based on observations related to the micro-systems performance which is often far away from linearity in MEMS devices.

There are two types of components that are extensively used in MEMS design: micro-beams (cantilever type) and micro-plates. Manufacturing as well as usage of these components are advantageous to MEMS applications. The main applications of such structures include micro-sensors and micro-actuators.

Large deflection of micro-cantilever beams under electrostatic force is studied. Pull in voltage as a phenomenon was widely studied in conjunction with MEMS. Large deflection of micro-cantilever beams under electrostatic field with the application of a voltage very close to pull in voltage is studied in this thesis and it is shown that pull in voltage provided by the nonlinear analysis is different from the one yielded by the linear analysis and more accurate when compared to the experimental values.

Large deflection of curved micro-cantilever beams sometimes encountered as AFM probes was studied to investigate the variation of sensitivity under large deflection of

originally curved micro-cantilever beams. Results show that curved or straight beams experience same sensitivity which decreases with the increase of deflection.

Micro-plate pressure sensors are widely used in industrial applications. Deposition of several different layers creates residual stress in those layers. The residual stress is measured indirectly by Stoney equation. It is shown that Stoney equation yields under normal circumstances up to 40% error in the value of the predicted stress and the experimental results do not match any numerical analysis. An extraction method was developed to calculate the stress distribution in each layer based on the experimentally measured deflection.

In summary, the work proves on few general configurations that the non-linear analysis of microstructures yields results that are closer to the results of the experimental investigations when compared to the ones yielded by the linear analyses. Analytical solutions of the differential equations were sought using Lie symmetry method.

Acknowledgment

I wish to express deeply sincere thanks to my supervisor, Professor Ion Stiharu for his invaluable lessons and energetic encouragement. I am very thankful to Professor Stiharu for his kind understanding of people he works with. I am also very grateful to him, as I always found his office door open to me to discuss any problems. It has been a pleasure and privilege to carry out research under his supervision.

I wish to acknowledge Maple Software technical support team for their professionalism. I have to extend my great words of thanks to my M.Sc. supervisors, late Professor Ali Sinaye and Professor S. Hossein Mansouri who guided me and also encourage me to study Lie groups.

In memory of my father,

Haidar Changizi

Dedicate to my mother,

Azam K. Amin

With All Love to My Wife,

Farnaz

Anyone who has never made a mistake has never tried

anything new.

Albert Einstein

Table of Contents

List of Acronyms

AC	**A**lternating-**C**urrent
AFM	**A**tomic-**F**orce-**M**icroscope
BEM	**B**oundary **E**lement **M**ethod
CCNF	**C**ontinues-**C**antilever-**N**atural-**F**requency
CONCACE	**C**oncordia-**C**enter-for-**A**dvanced-**V**ehicle-**E**ngineering
DC	**D**irect-**C**urrent
DCNF	**D**iscrete- **C**antilever-**N**atural-**F**requency
FEM	**F**inite-**E**lement-**M**ethod
HeNe	**H**elium-**N**eon
LTCC	**L**ow-**T**emperature **C**o-fired **C**eramic
MEMS	**M**icro-**E**lectro-**M**echanics-**S**ystems
MicraGeM	**Micra**lyne-**Ge**neralized-**M**EMS
ODE	**O**rdinary **D**ifferential **E**quation
PDE	**P**artial **D**ifferential **E**quation

List of Symbols

A	Area
A_{eff}	Effective area
a	Length of Plate
a_0	Unit vector
B	Material property of Ludwick
b	Strain in spatial coordinate
b	Width of Cantilever beam
b_{eff}	Effective width
C	Cauchy-Green tensor
$C_{10}, C_{01}, C_{20}, C_{11}, C_{02}$ $C_{30}, C_{21}, C_{12}, C_{03}$	Material constants
$C_1, C_2, C_3, C_4, C_5, C_6$	Constant of infinitesimal transformation
D	Rigidity of Plate
d	Material incompressibility, Material constants
d_k	Material constants
E	Green-Lagrange tensor, Young modulus
E^*	Modified Young's modulus

$E(x)$	Young modulus as function of x
e	Euler-Amansi tensor
$F(X,t)$	Deformation gradient
$f(t)$	Force
F	Point Force
G	A Lie group
g	Gap
H	Horizontal point force
h	Thickness of beam
I	Moment of inertia
I_1, I_2, I_3	Invariants of C
k	Spring stiffness
k_{eff}	Spring effective stiffness
L	Initial length
l	Length
M	Manifold
M_0	Initial Moment
$M(x)$	Moment in section
m	Mass
N	Manifold, Material constant
n	Normal direction
P	Point force

P_0	Pressure
$q(x,y)$	Force on a plate
R^n	n-dimensional Euclidean space
r,s	Canonical coordinates
$\hat{r},\hat{s}$	Canonical Coordinates for p and q
S	Second Piola-Kirchhoff stress tensor
T	Thickness of wafer
T_P	First Piola-Kirchhoff traction vector
t	Time
t_C	Cauchy traction vector
th	Thickness of beam
U	Transformation operator on the function
$u(v)$	A Function of derivative of $y(x)$
V	Voltage
V_f	Vertical point force
$v(r)$	A function of r
v_0	Initial velocity
W	Strain energy function per unit un-deformed volume
w	Vertical deflection of plate
w	Width of Cantilever beam
$w_{\max}$	Maximum vertical deflection of a plate
X	Transformation operator on the function

X_P	Position vector
x	Independent variable
$\dot{x}$	Time derivative of x
(x_1, y_1)	Coordinate of a point in Euclidean space
y	Deflection
α	Correction factors of area x direction
α_a	Angles
α_i	Material constants
β	Correction factors of area y direction
β_a	Angles
δ_h	Horizontal deflection
δ_v	Vertical deflection
δ_x	Deflection in x direction
ε_0	Permittivity
ε	Parameter of Lie group
ε_A	One dimension Euler-Alman strain
ε_G	Green-Lagrange strain
$\eta(x, y)$	Infinitesimal transformation
θ_0	Angle with horizontal
θ	Angle of curvature

λ	Stretch
$\lambda_1^2, \lambda_2^2, \lambda 2_3$	Eigenvalues of C
μ	Initial shear modulus of materials
μ_i	Material constants
υ	Poisson's ratio
$\xi(x, y)$	Infinitesimal transformation
ξ	Damping coefficient
ρ	Curvature
ρ_d	Density
σ	Cauchy stress tensor
σ_f	Residual stress
$\tau(\varepsilon)$	Parameter of a Lie group
ϕ	Transformation functions
Ψ	A function of r
Ψ	Airy stress function
ψ	Transformation functions
$\omega(x, y, \frac{dy}{dx})$	A function of $x, y, \frac{dy}{dx}$
ω_n	Natural frequency

List of Figures

List of Tables

Preview of the Thesis

The work included in the thesis is mostly based on a method of reduction of the order of differential equations by one unit. The method is purely mathematical and it has been rarely used in engineering. One of the overall objectives of this dissertation is to evaluate the capability of Lie group symmetry in solving problems related to microsystems technology.

Microsystems were selected as they offer a large variety of problems involving nonlinearities and thus nonlinear differential equations which are usually solved only after linearization. Lie symmetry group method was selected as the method although cumbersome, it enables to create receipts that once applied, yields a solution. On another hand, the method has its own limitations as a solution could be found only if symmetry of the group is found. This is the case of the problem solved in the chapter 2 where the dynamic characterization of a micro-cantilever beam subjected to an electric filed close to the instability is applied. The reduction of the second order stiff ODE was possible to a first order ODE. No symmetry was found for the first order DOF. However, the appropriate numerical method used to solve the initial equation yield same result as the reduced differential equation. The results match the experimental measurements.

Same Lie symmetry group method was used in chapter 3 to determine the nonlinear deflection of a micro-cantilever beam subjected to multiple types of loads. In this case, the reduction of the order of the differential equation was possible to expressing the solution in close form.

For certain problems, Lie symmetry group method is not applicable. However, the classical approach was considered to elaborate an optimization algorithm that helps to determine the inter-laminar stress in multilayered micro-plates that exhibit large deflections under dynamic pressure.

In the author's opinion, Lie symmetry group method is a powerful tool in solving problems that have been approached by linearization. The microsystems filed is largely populated of such type of problems.

Chapter 1

Nonlinearity Effects on Static and Dynamics Performance of MEMS

Rationale

MEMS is a relatively new area in engineering. Experimental and analytical systematic research on MEMS started around 1970s as an investigative interest of Si foundry engineering to the quite peculiar properties of mono-crystalline Si. MEMS gained significant momentum when useful devices became commercially available. The research on MEMS gained more significance through the subdivision of interest which has created a solid base of knowledge that is spread over modeling, simulation, manufacturing and the liaison among design, fabrication and performances. Each research area has brought light over either fabrication methods (extension of MEMS from Si to metal or/and polymer), modeling principles, mathematical description of multi-physics phenomena, test methodology and characterization, etc. The new designs target specific applications that originally were strongly bonded to mass production systems. The significant

advancement made by the fabrication technologies including the multi-user concept made possible to conceive MEMS for lower production applications. The unusual physics of microstructures played a major role mainly in the development of new MEMS used for detection and sensing.

The modeling of MEMS comes with some significant challenges. The unusual influences of specific field forces or the significantly relative large defections encountered by the mechanical micro-structures make the researchers assume that the macro model constituent equations may not always accurately describe some of the phenomena. Most of the present works in modeling assume that micro-structures behave as large scaled structures of the same type while scaled down. It is apparent from here that using nonlinear formulations may enhance the accuracy of the models. The nonlinear mechanics is a well-established area in which the contributions are usually brought by theoreticians. Practical investigations on MEMS have been so far focused by experimentalists.

The objective of this research is to investigate how nonlinearities affect both static and dynamic performance of the micro-structures in comparison with the linearity assumptions. The specific objective of the research is to prove that the assumption of nonlinearity significantly improves the model accuracy. The results of the nonlinear models will be compared with the experimental data and weigh against the linear based modeling of a few popular microstructures including cantilever beams, cantilever bridges and micro-plates will be evaluated and accurate nonlinear models will be proposed.

1.1. Nonlinearity

First, one has to define the meaning of nonlinearity in mechanics analysis. For a physical phenomenon in which a single input variable is targeted and a single output is sought, a generic mathematical model can be written. This mathematical model is usually an algebraic equation like:

$$x_{k+1} = f(x_k) \tag{1.1}$$

which is called discrete-time system[4]. For continuous – time systems the mathematical model is a differential equation in the form:

$$\dot{x} = f(x,t) \tag{1.2}$$

that is called non-autonomous system[4]. In an autonomous system the differential is of the form:

$$\dot{x} = f(x,M) \tag{1.3}$$

where in all of above equations, f is a map from manifold M to manifold$N$, $M \subset R^n$ *and* $N \subset R^n$ [4]. If in a continuum mechanics the differential equations describing the governing phenomena are linear, the problem will be called linear. Otherwise they are called nonlinear. There are two sources of nonlinearity in mechanical engineering

modeling. (a) Geometric (b) Material [5]. Geometrical nonlinearity is due to the nonlinear stress-strain relation or to large deformation while material nonlinearities are assigned to the nonlinear behavior of material properties [5].

However, in most cases, simplifying the problem to linear differential equation helps to solve the model much easier than nonlinear differential equations and in most cases the results are acceptable within certain range. However, there are some cases that simplifying of differential equations to linear form creates incorrect answers. These cases are difficult to point before the validation against experimental results is performed.

1.2. Geometric nonlinearities

Geometric nonlinearities [6] are mainly due to the fact that the deformation gradient is very large in comparing to the size of the body or otherwise said, the stress and the strain do not keep a linear relation like Hook's law. So it is necessary to define new strain and stress relationship. To define the strain in material coordinate, it is necessary first to define stretch ratio:

$$\lambda_{a_0}(X_P, t) = F(X_P, t)a_0 \tag{1.4}$$

where:

λ_{a_0} stretch rate

F is the deformation gradient,

X_P is the position vector,

a_0 is the unit vector,

where F is defined as:

$$F = [\frac{\partial X_P}{\partial x}] \tag{1.5}$$

Green deformation tensor (Right Cauchy-Green tensor) is defined as:

$$C = F^T F \tag{1.6}$$

And Green-Lagrange strain tensor is defined as:

$$E = \frac{1}{2}(F^T F - I) \tag{1.7}$$

One dimension Green-Lagrange strain is:

$$\varepsilon_G = \frac{l^2 - L^2}{2L^2} \tag{1.8}$$

where L is initial length and l is final length. Strain in spatial coordinate, defined as:

$$b = FF^T \tag{1.9}$$

b is left Cauchy-Green tensor. Euler-Almansi strain tensor is defined as:

$$e = \frac{1}{2}(I - F^{-T}F^{-1}) \tag{1.10}$$

One dimension Euler-Almansi strain is:

$$\varepsilon_A = \frac{l^2 - L^2}{2l^2} \tag{1.11}$$

At this point, stress tensor should be defined for nonlinear stress analysis.

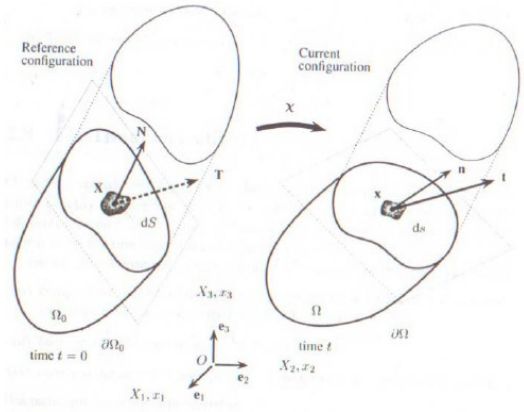

Figure 1.2.1. Traction vectors acting on a surface element [3]

As it is clear from the above figure, for an element one can write:

$$df = t_C ds = T_P ds \tag{1.12}$$

$$t_C = t_C(x, \tau, n) T_P = T_P(X, \tau, N) \tag{1.13}$$

where df is the applied force on the surface and t_C is Cauchy (or true) traction vector (force measured per unite surface area defined in the current configuration) exerted on ds with normal n. T_P is the first Piola-Kirchhoff (or normal) traction vector. There exist unique second-order tensor field σ and P so that:

$$t_C(x,t,n) = \sigma(x,t)n \tag{1.14}$$

$$T_P(x,t,N) = P(X_P,t)N \tag{1.15}$$

where σ is called Cauchy stress tensor. These equations show that, if traction vectors depend on unit normal then they must be linear in normal.

1.3. Material nonlinearity

Material nonlinearity is due to nonlinear constitutive behavior of material of the system [4]. Among the nonlinearity of materials, hyperelasticity of materials has a import role in micro-structures. Many micro-structures can be simulated by hyperelastic behavior of materials. These kinds of materials have large elastic strain which is recoverable [7]. It is shown that [6] the stress response of hyperelastic material is derived from the given strain-energy function W. Numerous forms of strain-energy functions have been introduced. For using these forms, we have to define strain potential energy. W is a scalar function of strain or deformation tensors which one can write:

$$S_{ij} = \frac{\partial W}{\partial E_{ij}} = 2\frac{\partial W}{\partial C_{ij}} \tag{1.16}$$

where:

S_{ij} are components of second Piola-Kirchhoff stress tensor

W is strain energy function per unit undeformed volume

E_{ij} *are components of the Green-Lagrange strain tensor*

C_{ij} are components of right Cauchy-Green tensor

Under the assumption that material response is isotropic, it is convenient to express the strain energy function in terms of strain invariants:

$$W = W(I_1, I_2, I_3) = W(I_1, I_2, \lambda) = W(\lambda_1, \lambda_2, \lambda_3) \tag{1.17}$$

where:

$$I_1 = \lambda_1^2 + \lambda_2^2 + \lambda_3^2 \tag{1.18}$$

$$I_2 = \lambda_1^2\lambda_2^2 + \lambda_2^2\lambda_3^2 + \lambda_3^2\lambda_1^2 \tag{1.19}$$

$$I_3 = \lambda_1^2\lambda_2^2\lambda_3^2 = J^2 \tag{1.20}$$

and I_1 , I_2 , I_3 are invariants of C, also $\lambda_1^2, \lambda_2^2, \lambda_3^2$ are eigen-values of C. By defining the volume-preserving part of, F :

$$\bar{F} = J^{-\frac{1}{3}} F \tag{1.21}$$

where:

$$J = \det(F) \tag{1.22}$$

It can be shown that[6]:

$$\bar{\lambda}_p = J^{-\frac{1}{3}} \lambda_p \qquad p = 1,2,3 \tag{1.23}$$

$$\bar{I}_p = J^{-\frac{2}{3}} I_p \tag{1.24}$$

Therefore, the strain potential energy is:

$$W = W(\bar{I}_1, \bar{I}_2, J) = W(\bar{\lambda}_1, \bar{\lambda}_2, \bar{\lambda}_3, J) \tag{1.25}$$

Here, we introduce some models that are defined for strain energy potential applications. These models proved to be quite appropriate to model strong non-linear strain-stress relationships.

A) - <u>Neo-Hookean model:</u>

$$W = \frac{\mu}{2}(\bar{I}_1 - 3) + \frac{1}{d}(J-1)^2 \tag{1.26}$$

where:

μ = initial shear modulus of materials

d = material incompressibility

B) – <u>Mooney-Rivlin:</u>

$$W = C_{10}(\bar{I}_1 - 3) + C_{01}(\bar{I}_2 - 3) + C_{20}(\bar{I}_1 - 3)^2 + C_{11}(\bar{I}_1 - 3)(\bar{I}_2 - 3) + C_{02}(\bar{I}_2 - 3)^2 + C_{30}(\bar{I}_2 - 3)^3 + C_{21}(\bar{I}_1 - 3)^2(\bar{I}_2 - 3) + C_{12}(\bar{I}_1 - 3)(\bar{I}_2 - 3)^2 + C_{03}(\bar{I}_2 - 3)^3 + \frac{1}{d}(J-1)^2 \quad (1.27)$$

where:

$C_{10}, C_{01}, C_{20}, C_{11}, C_{02}, C_{30}, C_{21}, C_{12}, C_{03}, d$ = material constants

C) – <u>Ogden potential</u>

$$W = \sum_{i=1}^{N} \frac{\mu_i}{\alpha_i}(\bar{\lambda}_1^{\alpha_i} + \bar{\lambda}_2^{\alpha_i} + \bar{\lambda}_3^{\alpha_i} - 3) + \sum_{k=1}^{N} \frac{1}{d_k}(J-1)^{2k} \quad (1.28)$$

where:

N, μ_i, α_i, d_k = material constant

1.4. Cantilever beams nonlinear static deflection

Most of mathematical close forms formulations on nonlinear deflections of cantilever beams are just for point force on the tip [1, 8-11]. The only different aspect is the approach of the formulation of the solving algorithm. For a moment on the beam, it is possible to reduce one degree of ODE by Lie symmetry. The result is:

$$\frac{2E \times I(y - xy')}{\sqrt{1 + y'^2}} - M \times (x^2 + y^2) - (E \times I)^2 = const \tag{1.29}$$

M is moment in each section

For general type of forces on cantilever, suitable numerical methods were used [12, 13].

1.4.1. Micro-cantilever beams

There has been significant research carried out on micro-cantilever beams. Most of these studies are on the influence of the electrostatic forces and the adhesion or stiction of beams [14-18]. All works in which the models were formulated in nonlinear equations were solved by numerical methods and compared with experimental results. Many investigations in micro-level modeling are looking at the dynamic properties and behavior of micro-cantilevers beams [19-26]. Natural frequency as well as the quality factor are used for controlling, for example, voltage [21], and switches [22], in acoustic wave resonators [19]. Bimorph micro-cantilevers are more sensitive than anamorphic beams. In some works, researches showed that sensitivity increases in bimorph materials

significantly [27]. Bimorph micro-cantilever beams are mostly used in thermal sensing and for this purpose the tip deflection of the bimorph cantilever beams [27-33], large deflections, stress analysis [34-36] and experimental validations [37, 38] were carried out. Bimorph micro-cantilever beams are also used as actuators. The mathematical model [39], of the deflection is studied [40]. Thermal actuators are studied widely, theoretically [41, 42], experimental[43] applications [44] and for their dynamic behavior [45].

1.4.2. Nonlinear behavior of micro-plates

Large deflection of plates received much more attention during 1940-1950 [46], but still there are many researches working on closed form solution of nonlinear deflection of plates under different boundary conditions [46-53]. Although the dynamic behavior of plates is very important, nonlinear dynamic behavior of plates is studied and regardless of the formulation, the solution of the constitutive equations is sought through numerical methods [54, 55].

1.4.3. Micro-plates

Nonlinear dynamical behavior of micro-plates has been studied in Virginia Polytechnic Institute recently by professor Nayfeh and his team [56-58]. Mostly the work is focusing on nonlinear response of micro-plates. Other mathematical methods are used in micro-plates such as BEM[59] where the method is used just for electrical field formulation and then tractions on the plate surface.

1.5. Thesis layout

The thesis is divided into 5 chapters and 6 appendices. Chapter 1 presents the rationale of the present work and a brief introduction on the open literature in the non-linear micro-systems formulations as well as the solution of the constitutive equations. In this chapter the geometric and the material non-linarite are presented along with the models that are usually employed in the open literature for such type of non-linearity. A brief review of the literature on the non-linear approaches used in micro beams and micro-plates is presented.

Chapter 2 presents the dynamic analysis of micro-cantilever beams electrically charged and subjected to electrostatic filed. Under higher fields higher attraction forces are generated such that the elastic structures may be projected on the substrate electrode. This phenomena known as snap-on is analyzed through the perspective of the non-linear dynamics. The conclusions of the investigations carried out using Lie groups method to reduce the order of the differential equation is that the linear model indicates more conservatory solution for the snap-on critical gap. The model was validated by experiments and indirect measurement of the resonant frequency of micro-structures exposed to electrostatic field. The study was extended through a parameter analysis on the influence of the geometric parameters on the performance characteristics of micro-structures.

Chapter 3 presents the static nonlinear model of a microstructure – micro-cantilever beam under multiple point loads. The solution to the problem was formulated for curved or straight beams and an exact analytical solution for the deflection was presented. Material

non-linears is assumed. The solution was derived based on Lie group symmetries. An example application is presented as an AFM probe and the numerical solution was presented. The results were validated against the existing literature which presents exact results for single point load conditions. A sensitivity analysis related to geometry and material is also presented in this chapter.

Chapter 4 presents an extraction method that enables to determine with higher accuracy the inter-laminar stress developed in micro-plates made from multiple thin films of different materials. Here, the experimental results were assumed as baseline and the matching solution would require varying the pre-selected values of the internal stresses to match the aimed deflection. The stress in each layer was assumed to vary by $\pm$ 40% of the nominal value. The extraction of the value of stress was performed using the gradient method optimization. An algorithm that performs the extraction is presented.

Chapter 5 presents the conclusions and the future work. The present study indicates the fact that linear static or dynamic assumption on MEMS microstructures will introduce significant errors in models of MEMS. The need to extend the present work is evident.

Chapter 2

Linear Versus Nonlinear Dynamic Analysis of Micro-Structures under Electrostatic Field

Rationale

Dynamic performance of micro-systems is altered significantly when subjected to electrostatic fields. MEMS are often operating under such condition. The resonant frequency would dramatically drop while the structures may suffer significant damage if the difference of potential between the structure and the electrode exceeds a critical value. The findings reported in the open literature are related to linearized models of the "pull-in" phenomenon in micro-structures subjected to electric field. The mathematical formulation of such a phenomenon makes use of the one degree of freedom lump mass model, which is expressed as a nonlinear ordinary differential equation (ODE). The chapter presents a method of reduction by one the order of the nonlinear ordinary

differential equation that models such microstructures by using Lie symmetry groups. Cantilever beams are used as example of structures in this analysis. The reduced order equation shows two terms of the non-linear ODE equation. Linearized models of the "pull-in" voltage indicate that the structures become unstable and are attracted by the fixed electrode when they reach a position that corresponds to 2/3 of the original gap. However, the nonlinear model indicates a critical distance at which the structure reached a saddle point which corresponds to 11/20 (55% of the original gap instead of 66.6%) after which it settles at a stable position corresponding to a deflection of 9/40 of the original gap (22.5% instead of 33.33%). The pull-in voltage assessed through the nonlinear model indicates higher value than the one calculated through the linear approach. Potential exceeding the critical values will lead to the instability of the structure. Few equivalent stiffness models used in this assessment yield identical results from the critical gap point of view. The analysis of the "pull-in" voltage for the non-linear model versus linear models or simplified non-linear models indicates a very close correlation with experiments carried out in the lab or presented in the open literature. It is also proved that numerical methods might not yield a reasonable solution for problems extracted from microstructure applications subjected to electrostatic filed. Experimental validation of the static deflection and natural frequency decay when subjected to a difference of potential for two microstructures pointed towards the fact that various models match best specific experimental conditions and two different models could yield best results for two different case studies.

2.1. Introduction

At micro-level, mechanical structures are expected to dynamically operate in bandwidth way below their resonant frequency given the fact that micro-structures subjected to electrostatic field encounter their resonant frequency to a significantly lower value than to the identical micro-structures not subjected to electrostatic field. The laws of mechanics that govern the dynamics of micro-structures have been usually based on the Newtonian formulations. For micro-structures have also been proposed Newtonian formulations to model the effect of the electrostatic field on dynamic performance of micro-systems. Micro-cantilever beams are very popular in MEMS design because of several reasons including simplicity to fabricate and release from substrate, good match of their pre-determined performance under the provision that they operate within a limited range, close within the linear domain. Also they use low voltage for measurement purpose while they operate at frequencies significantly below their resonant frequency[60].

Most of the available published works present models that are described by differential equations. These equations have been formulated as linear or nonlinear [61-64]. However, most of the nonlinear equations are linearlized for simplicity [65-69]. However, very little contribution to the influence of the downscaling has been made with regards to the correctness of the linearity assumptions. All formulations of the Newtonian laws could be written either as ODE's or PDE's. A number of publications conclude that specific formulations could be assumed as linear in micro-systems modeling [61, 62, 66, 67, 69-76]. Other publications have recommended the nonlinear models as necessary against the linear models [63-65, 68, 77-80]. In some cases authors consider the system as behaving nonlinear and solve the nonlinear differential equations [63, 65, 77, 78, 80].

In other publications, the micro-systems are considered as nonlinear but linearization methods are used to simplify the path to the solution [64, 67, 68, 71, 74]. However, most of the contributions consider linear models and thus linear equation and solve those [61, 62, 66, 69, 70, 72, 73, 75, 76, 79].

The attractive electrostatic forces are common in the actuating MEMS devices or they intervene during capacitive measurement in small scale electro-mechanical devices. Electrostatic forces have many implications as most of MEMS structures are subjected to electrostatic forces[81, 82]. Capacitive measurement based accelerometer have been widely used [83]. In MEMS, electrostatic forces are often used to actuate micro-structures, including switches [84, 85], micro-grippers [86], micro-relays [87], electrostatic motors[88, 89]. For electrostatic micro-actuators with linear motion, they have been proposed parallel, quad, and comb types of configurations. The use of electrostatic actuation in MEMS is appealing because is quite efficient, produces high energy densities and large micro-scale forces, yet all gathered in simple configurations[90]. Moreover, electrostatic actuators have advantages of inherent simplicity of their design as well as fast response. The fabrication of electrostatic actuators is compatible with integrated circuit (IC) processes in contrast to other type of actuators [81]. Unfortunately, microstructures undergo large deformation when subject to electrostatic actuation. The interaction between a nonlinear electrostatic force and the coupled effects from different energy fields may cause pull-in instability and failure. Effects such as stiction, wear, dielectric changing and breakdown are likely to occur in microstructures subjected to electrostatic field. As a consequence of the popularity and utility of electrostatic MEMS, many aspects related to the effects subject to electrostatic forces in MEMS devices have largely been investigated in recent years. Researchers have

studied the pull-in instability [91-94], characteristics of the displacement during actuation[90, 95-97], shape and location of electrodes [98-100], dynamic response and optimization of the electrostatic force[85, 101], nonlinear dynamics, chaos and bifurcation of the electrostatically actuated systems and analysis methods (FEM) for evaluating the nonlinear electrostatic forces[102-106], simulation software (ANSYS) and systems to simulate the dynamic behavior [105, 107-109], influence of bonding parameters (applied voltage, temperature, etc.) on the electrostatic force[110], inherent nonlinear and stiffness softening effects [82, 102]. Without an understanding of the effects of electrostatic forces in MEMS, many phenomena of practical importance, such as instability, nonlinearity and reliability in MEMS cannot be mathematically modeled and therefore practically predicted, and consequently, the great potential of MEMS technology could neither be effectively explored nor optimally utilized. Therefore, it is important and necessary to investigate the dynamic characteristics of the electrostatic forces and their nonlinear effects on MEMS devices at micro-scale level [102]. In the present chapter, solution of the nonlinear ODE describing vibration of a micro-cantilever beam subjected to electrostatic force was studied by reducing the order of ODE. The nonlinear differential equation does not have any exact solution. It is shown that some common methods [111] which were used to solve such equation introduce significant errors. The problem becomes more complex when micro-level dimensions are considered in the equation, which makes the equation highly stiff. As an example, it was shown that numerical methods embedded within Maple could not solve such stiff ODE problem as illustrated in the appendix A. In the present work, an exact method is used to reduce the order of ODE such that no error is introduced through the reduction calculations. The reduced (first order ODE) yields identical results with the second order non-linear ODE.

The first order ODE is further solved using A-stable numerical methods as the resulting ODE can be proved as non-reducible.

Lie symmetry method is a well-known mathematical method that can be used to solve or reduce the order of nonlinear ODEs and PDEs. Lie symmetry will be used below to reduce the order of the nonlinear ODE that is used to model the nonlinear mass-damping-spring model of a cantilever beam subjected to a uniform electrostatic force.

2.2. The vibration of a micro cantilever beam subjected to uniform electrostatic field

The electrostatically actuated micro-cantilevers in MEMS and the equivalent lump mass dynamic model are illustrated in figures 2.1.1 and 2.1.2. For this simplified mass spring damping system, the governing equation of motion for the dynamics of the system in MEMS is [102] :

$$\frac{d^2y(t)}{dt^2} + 2\zeta\omega_n \frac{dy(t)}{dt} + \omega_n{}^2 y(t) = \frac{f(t)}{m} \tag{2.1}$$

where:

f(t) is the electrostatic force

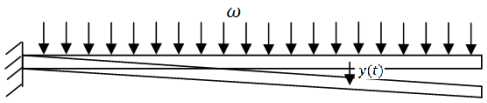

Figure 2.1.1. Fixed–free beam subjected to distributed uniform load (electrostatic attraction)

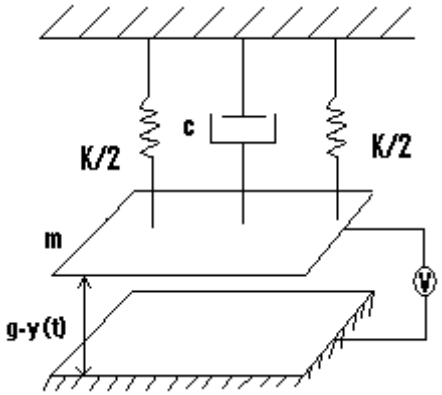

Figure 2.1.2. The schematic of a mass-spring damper system of a beam

The energy balance yields the force, which applies on the two parallel surfaces due to the electrostatic effect, which is[101]:

$$f(t) = \frac{\varepsilon_0 A V^2}{2(g - y(t))^2} \tag{2.2}$$

g is gap between the beam and base

A is area of cantilever beam

So the equation (2.1) will be:

$$\frac{d^2y(t)}{dt^2} + 2\zeta\omega_n \frac{dy(t)}{dt} + \omega_n{}^2 y(t) = \frac{\varepsilon_0 A V^2}{2m(g - y(t))^2} \tag{2.3}$$

where the initial conditions (initial speed at reference position and time) for this ODE is assumed as:

$$y\big|_{t=0} = 0 \qquad \text{and} \qquad \left.\frac{dy}{dt}\right|_{t=0} = v_0 \tag{2.4}$$

This is a nonlinear equation and there is no analytical formulation to express so far the result in close form. This equation becomes more complicated when one extends it to micro level dimensions, which may include very high stiff ODE. There have been many contributions in the literature towards solving this problem by using numerical methods [102, 111, 112] . In the current work, by using Lie symmetry method the order of equation (2.3) will reduce by one order. Therefore, instead of a second order ODE, one has to cope with a first order ODE that by all means is easier to solve. The solution of second order of the ODE is presented below. However, Lie symmetry method requires some definitions and terminologies.

2.3.1. One-parameter groups

The mathematical groups which are considered in this paper are point symmetric transformations [113] which means that each point (x, y) on the curve move into (x_1, y_1) :

$$x_1 = \phi(x, y, \alpha) \qquad y_1 = \psi(x, y, \alpha) \tag{2.5}$$

where ϕ, ψ are diffeomorphism (C^{∞}). If any transformation preserves the shape of a curve and it maps the curve on itself, the transformation is called symmetry [114]. The transformations (2.5) which satisfies the group properties is called one-parameter group [114] and α is called the parameter of the group.

2.3.2. Infinitesimal transformation

For a one-parameter group the infinitesimal transformation is defined as [115] :

$$Uf = \xi(x, y)\frac{\partial f}{\partial x} + \eta(x, y)\frac{\partial f}{\partial y} \tag{2.6}$$

where:

$$\xi(x, y) = \left.\frac{\partial \phi}{\partial \alpha}\right|_{\alpha=0} \qquad \eta(x, y) = \left.\frac{\partial \psi}{\partial \alpha}\right|_{\alpha=0} \qquad f = f(x, y) \tag{2.7}$$

U is the transformation operator on the function.

The necessary and sufficient condition that a group is a symmetry transformation for a function $f(x, y)$ is [115] :

$$Uf = 0 \tag{2.8}$$

This equation will be used to calculate the infinitesimal transformation of an ODE in next part.

2.3.3. Canonical coordinates

Any pair functions $r(x, y)$, $s(x, y)$ that satisfy the conditions below are called canonical coordinates [114]:

$$\begin{gathered} \xi(x, y) r_x + \eta(x, y) r_y = 0 \\ \xi(x, y) s_x + \eta(x, y) s_y = 1 \\ \begin{vmatrix} r_x & r_y \\ s_x & s_y \end{vmatrix} \neq 0 \end{gathered} \tag{2.9}$$

The canonical coordinates for a function $f(x, y)$ can be found by the characteristic equation [114]:

$$\frac{dx}{\xi(x, y)} = \frac{dy}{\eta(x, y)} = ds \tag{2.10}$$

The solution of the below ODE is $r(x, y)$:

$$\frac{dy}{dx} = \frac{\eta(x,y)}{\xi(x,y)} \tag{2.11}$$

and $s(x,y)$ will be:

$$s(r,x) = (\int \frac{dx}{\xi(x,y(r,x))})\Big|_{r=r(x,y)} \tag{2.12}$$

2.3.4. Algorithm for Lie symmetry point

There have been investigations on calculation of Lie symmetry point [116-121]. There are, however, several methods to calculate Lie symmetry [121]. One method is the prolonged vector field [116, 120, 121]. It can be shown that [115, 116] for a second order differential equation like:

$$\frac{d^2y}{dx^2} = \omega(x, y, \frac{dy}{dx}) \tag{2.13}$$

If an infinitesimal group is applied as an operator on (2.13), both ξ and η in (2.7), must satisfy the below equation:

$$\begin{aligned}&\eta_{xx} + (2\eta_{xy} - \xi_{xx})y' + (\eta_{yy} - 2\xi_{xy})y'^2 - \xi_{yy}y'^3 + (\eta_y - 2\xi_x - 3\xi_y y')\omega = \\ &\xi\omega_x + \eta\omega_y + (\eta_x + (\eta_y - \xi_x)y' - \xi_y y'^2)\omega_{y'}\end{aligned} \tag{2.14}$$

By decomposing (2.14) into a system of PDEs, ξ and η can be calculated. The example below will present the calculation methodology. So from (2.5) the transformation φ and ψ can be found. For a first order differential equation like:

$$\frac{dy}{dx} = \omega(x, y) \tag{2.15}$$

ξ and η in (2.7) must satisfy the below equation:

$$\eta_x + (\eta_y - \xi_x)\omega - \xi_y \omega^2 = \xi\omega_x + \eta\omega_y \tag{2.16}$$

There are several commercial software packages such as Maple [116, 122] or Mathematica [118], that have built-in algorithms to calculate Lie point symmetry group, which means calculating ξ and η. After calculating ξ and η, one can calculate canonical coordinates by (2.10), (2.11), (2.12). Further, thought adequate selection of variables, the order of the ODE can be reduced by one unit.

2.3.5. Reduction of the order of the ODE

Let a one-parameter group G be the symmetry of a differential equation. The relations (2.10), (2.11), (2.12) which represent canonical coordinates can be calculated and further

$v = \frac{ds}{dr}$ can be calculated. By considering v as a new variable and substituting in ODE, the new ODE will have one order less than the original ODE.

2.3.6. Solution of first order ODE with Lie symmetry

If the first order ODE (2.15) has a Lie symmetry, which can be calculated by (2.16), then the ODE (2.16) based on canonical coordinates can be written as[114]:

$$\frac{ds}{dr} = \frac{s_x + \omega(x,y)s_y}{r_x + \omega(x,y)r_y} \tag{2.17}$$

This ODE will be in the form of:

$$\frac{ds}{dr} = \Psi(r) \tag{2.18}$$

The general solution of (2.18) can be expressed as:

$$s - \int \psi(r)dr = c \tag{2.19}$$

where c is an integration constant. Further, by substituting (s,r) by (x,y) one can calculate y as a function of x.

2.4. Identification

Lie symmetry method is further used to solve the linear free vibration of a mass spring-damper system. The equation in (2.20) defines free vibration of a system (see figure.2.2.2)

$$\frac{d^2y(t)}{dt^2} + 2\zeta\omega_n \frac{dy(t)}{dt} + \omega_n{}^2 y(t) = 0 \tag{2.20}$$

This ODE is easy to solve and there are known many methods to do it. One can find the solution of (2.20) in any vibration textbooks. Below, for illustration purpose, Lie point symmetry is used to solve the above ODE [111]. Equation (2.20) is therefore converted in:

$$\frac{d^2y(t)}{dt^2} = -(2\zeta\omega_n \frac{dy(t)}{dt} + \omega_n{}^2 y(t)) \tag{2.21}$$

from (2.13):

$$\omega(x, y, \frac{dy}{dx}) = -(2\zeta\omega_n \frac{dy(t)}{dt} + \omega_n{}^2 y(t)) \tag{2.22}$$

For this form, condition (2.14) expresses the Lie symmetry point condition, because it satisfies:

$$\eta_{xx} + (2\eta_{xy} - \xi_{xx})y' + (\eta_{yy} - 2\xi_{xy})y'^2 - \xi_{yy}y'^3 + (\eta_y - 2\xi_x - 3\xi_y y')(\alpha y' + \beta y) = \eta\beta + (\eta_x + (\eta_y - \xi_x)y' - \xi_y y'2)\alpha \tag{2.23}$$

where:

$$\alpha = -2\xi\omega_n$$
$$\beta = -\omega_n^2$$
$$\omega = \alpha y' + \beta y$$
$$\omega_x = 0$$
$$\omega_y = \beta$$
$$\omega_{y'} = \alpha$$

It is important to note that, the variables x, y, y' are considered independent [113-115, 120] which would not reduce the generality of the formulation. Most of Lie symmetries including rotating translation and scaling could be found with the below transformations:

$$\xi = C_1 + C_2 x + C_3 y$$
$$\eta = C_4 + C_5 x + C_6 y \tag{2.24}$$

Substitution of (2.24) in (2.23) gives:

$$(C_6 - 2C_2 - 3C_3 y')(\alpha y' + \beta y) = \beta(C_4 + C_5 x + C_6 y) + (C_5 + (C_6 - C_2)y' - C_3 y'^2)\alpha \tag{2.25}$$

By comparing y' coefficients power, one can show that (see appendix B):

$$C_2 = C_3 = C_4 = C_5 = 0 \tag{2.26}$$

Hence,

$$\begin{aligned} \xi &= C_1 \\ \eta &= C_6 y \end{aligned} \tag{2.27}$$

Equations (2.27) give the general transformation for (2.20). It is possible to consider ξ and η as:

$$\begin{aligned} \xi &= 0 \\ \eta &= y \end{aligned} \tag{2.28}$$

Where:

$$C_1 = 0, \quad C_6 = 1$$

$$Uf = yf_y \tag{2.29}$$

From (2.10) and (2.11) one can finds the canonical coordinates as:

$$\begin{aligned} r &= t \\ s &= \ln(y) \end{aligned} \tag{2.30}$$

For reducing the order of ODE:

$$v = \frac{ds}{dr} = \frac{y'}{y} \tag{2.31}$$

$$\frac{d^2 s}{dr^2} = \frac{y''}{y} - \frac{y'^2}{y} \tag{2.32}$$

From (2.31) and (2.32), one can calculate y', y'' as:

$$\begin{aligned} y' &= vy \\ y'' &= y(\frac{dv}{dr} + v^2) \end{aligned} \tag{2.33}$$

Substitution of (2.33) in (2.20) gives:

$$\frac{dv}{dr} + v^2 + 2\zeta\omega_n v + \omega_n^2 = 0 \tag{2.34}$$

This is the reduced form of (2.20). Equation (2.34) has also Lie symmetry (this problem is solvable by separating the variables, but just for illustrating the Lie symmetry method, this method is further used):

$$\begin{aligned} \xi &= 1 \\ \eta &= 0 \end{aligned} \tag{2.35}$$

Equations (2.35) can be calculated by considering (2.24) as Lie symmetry and substituting them in (2.15) where:

$$\frac{dv}{dr} = -(v^2 + 2\zeta\omega_n v + \omega_n{}^2) = \omega(v, r) \tag{2.36}$$

and:

$$\begin{aligned} \omega_v &= -(2v + 2\zeta\omega_n) \\ \omega_r &= 0 \end{aligned} \tag{2.37}$$

Therefore:

$$Uf = f_r \tag{2.38}$$

For avoiding confusion between parameters (2.34) written with other notation as below:

$$\frac{dp}{dq} = -(p^2 + 2\zeta\omega_n p + \omega_n{}^2) = \omega(p, q) \tag{2.39}$$

where:

$$\begin{aligned} p &= v(r) \\ q &= r \end{aligned} \tag{2.40}$$

Canonical coordinates of this infinitesimal transformation by using (2.10), (2.11) are:

$$\begin{aligned} \hat{r} &= p \\ \hat{s} &= q \end{aligned} \tag{2.41}$$

Equation (2.17) can be formulated as:

$$\frac{d\hat{s}}{d\hat{r}} = \frac{1}{p^2 + 2\zeta\omega_n p + \omega_n^2} \tag{2.42}$$

$\hat{r} = p$ is substituted in (2.39) such that:

$$\frac{d\hat{s}}{d\hat{r}} = \frac{1}{\hat{r}^2 + 2\zeta\omega_n \hat{r} + \omega_n^2} \tag{2.43}$$

This equation is separable, so for $\xi < 1$ the solution of this ODE is:

$$\hat{r} = \omega_n\sqrt{1-\zeta^2}\,\tan(\omega_n(\sqrt{1-\zeta^2}\,\hat{s} - \sqrt{1-\zeta^2}\,C_1) - \omega_n\zeta) \tag{2.44}$$

By considering (2.40) and (2.41):

$$v(r) = \omega_n\sqrt{1-\zeta^2}\,\tan(\omega_n(\sqrt{1-\zeta^2}\,r - \sqrt{1-\zeta^2}\,C_1) - \omega_n\zeta) \tag{2.45}$$

where C_1 is the constant of integration. Substituting $v(r)$ from (2.31) and r from (2.30) in (2.45) yields:

$$\frac{\frac{dy}{dt}}{y} = \omega_n\sqrt{1-\zeta^2}\,\tan(\omega_n(\sqrt{1-\zeta^2}\,t - \sqrt{1-\zeta^2}\,C_1) - \omega_n\zeta) \tag{2.46}$$

The solution of this ODE is:

$$y = C_2 e^{-\zeta\omega_n t}\cos(\omega_n\sqrt{1-\zeta^2}\,(t+C_1)) \tag{2.47}$$

This equation is the general solution of (2.20). Although Lie symmetry method looks more laborious then classical methods used in solving the second order linear differential equation, it also bears an important advantage versus the well-known methods. This is, Lie symmetry method could yield to the solutions of nonlinear differential equations that cannot be solved by other classical approach.

2.5. Reducing in the order of the ODE representing the vibration of a micro-cantilever beam under electrostatic field

In the Appendix C it was proved that (2.3) has an infinitesimal transformation according to (2.24) as:

$$Uf = f_x \tag{2.48}$$

which satisfies (2.9) and therefore:

$$\xi = 1 \text{ and } \eta = 0 \tag{2.49}$$

From (2.10), (2.11) and (2.12) the canonical coordinates can be calculated as:

$$(r,s) = (y,t) \tag{2.50}$$

by considering:

$$r(y,t) = y \tag{2.51}$$

and defining v as:

$$v = \frac{1}{\frac{dy}{dt}} \tag{2.52}$$

As proved in appendix C the equation can be expressed by contact form as:

$$\frac{dv}{dr} = -\frac{\frac{d^2y}{dt^2}}{(\frac{dy}{dt})^2} \tag{2.53}$$

or:

$$\frac{d^2y}{d^2t} = -v^{-3}\frac{dv}{dr} \tag{2.54}$$

Substituting (2.54), (2.55) and (2.56) in (2.50) yields:

$$-\frac{dv}{dr}+2\zeta\omega_n v^2+(\omega_n^2 r-\frac{\varepsilon_0 A V^2}{2(r-g)^2 m})v^3=0 \qquad (2.55)$$

This is a first order ODE with $v(0)=\frac{1}{v_0}$ as the initial condition. According the recent investigations, there is no one-parameter group that satisfies its symmetric condition (2.55). It is the reason for which there is no analytical solution for this ODE. In the appendix D, it is shown that using a transformation like (2.24) the form (2.55) has no scaling or rotation symmetry. This equation has a singularity (where $r=g$) and it cannot be integrated in closed form. Therefore, the numerical method approach is used as shown below.

2.6. Numerical analysis for the first order ODE

To illustrate the above findings, in the example presented below it is proved that the solutions of (2.3) and (2.55) are identical. A practical example is numerically solved using Maple 11. Both second order non-linear ODE and the reduced first order ODE equations are nonlinear and stiff. *Isode* algorithm is used to solve the equation. This algorithm is not provided in ODE Analyzer Assistant. As illustrated in appendix A, none of the algorithms provided within the ODE Analyzer Assistant of Maple 11 could solve the ODE.

2.6.1. Cantilever beam under electrostatic field forces

In this example, geometry with relevance to microstructures is selected. A micro-cantilever beam with the below dimensions and mechanical properties is considered:

Length l =200 [μm]

Width w =20 [μm]

Thickness th =2 [μm]

Density of material ρ= 2300 [$\frac{Kg}{m^3}$]

Damping factor ζ =0.1

Young's modulus E= 169 [GPa]

gap g = 4 [μm]

The moment of inertia of the cross section of the beam and the longitudinal cross section area are:

$$I = \frac{w(th)^3}{12} = 1.333 \times 10^{-23} [m^4] \tag{2.56}$$

$$A = l \times w = 4 \times 10^{-9} [m^2] \tag{2.57}$$

The stiffness of the beam, the mass and the natural frequency of system are:

$$k = \frac{3EI}{l^3} = 0.845[\frac{N}{m}] \;\; m = l \times w \times th \times \rho = 1.84 \times 10^{-11}\,[kg] \tag{2.58}$$

$$\omega_n = 3.515625\sqrt{\frac{EI}{ml^3}} = 4.355133 \times 10^5[\frac{Rad}{Sec}] \tag{2.59}$$

The pull-in voltage can be calculated as:

$$V_{pull-in} = \sqrt{\frac{8k}{27\varepsilon_0 A}g^3} = 21.27\;[V] \tag{2.60}$$

Therefore, the applied voltage must be less than 21.27 [V] in order to achieve a finite solution to the problem. Under this provision, a potential of V=10 [V] is assumed. By considering this voltage, the beam would not induce the pull-in phenomena. Equations (2.3) and (2.55) become:

$$\frac{d^2y(t)}{dt^2} + 87102.67140\frac{dy(t)}{dt} + 1.8967188411 \times 10^{11} y(t) = \frac{9.619565215 \times 10^{-8}}{(4 \times 10^{-6} - y(t))^2} \tag{2.61}$$

$$\frac{dv(r)}{dr} + 87102.67140v^2(r) + (1.8967188411 \times 10^{11} r - \frac{9.619565215 \times 10^{-8}}{(4 \times 10^{-6} - r)^2})v^3(r) = 0 \tag{2.62}$$

For the IC as $y(0) = 0, y'(0) = 0.2[\frac{m}{Sec}], v(0) = 5.0[\frac{Sec}{m}]$ the results produced by numerical methods are shown in the figures below.

Figure 2.6.1 illustrates the solution of equation (2.61). Figure 2.6.2 illustrates the variation of the inverse of velocity v as a function of r, which is displacement. Figure 2.6.3 illustrates the phase diagram of (2.61) and (2.62) while figure 2.6.4 illustrates the

difference between the numerical solutions obtained for the original second order ODE (2.61) and the reduced to the first order ODE equation in (2.62). The maximum absolute error is less than 0.01% which came from numerical round out.

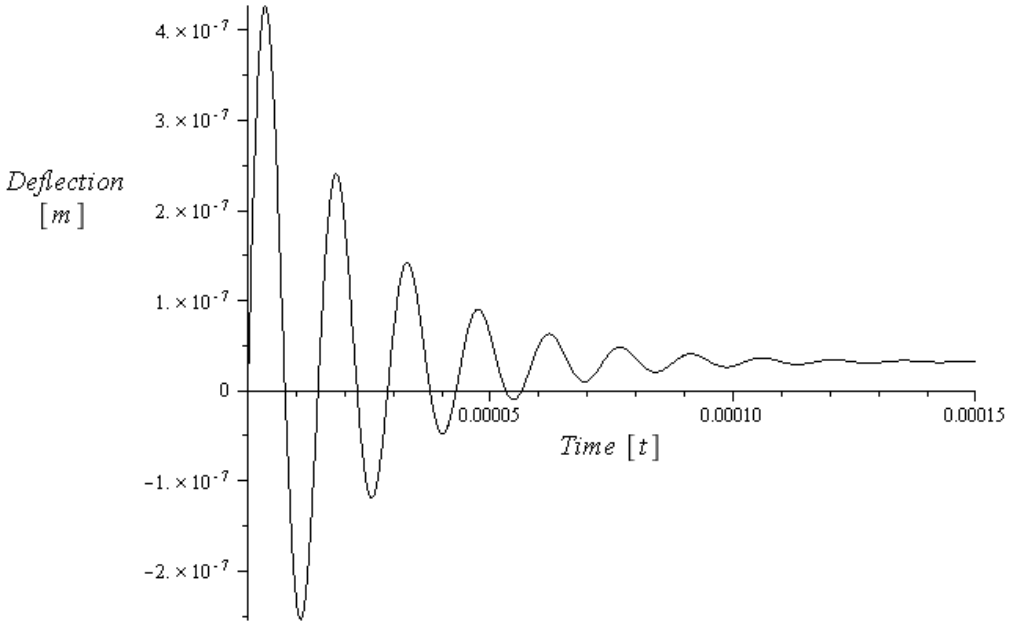

Figure 2.6.1. Time dependency of the deflection - numerical solution of the second order ODE equation (2.61). The potential is set to a low value such that the influence of the pull-in is insignificant.

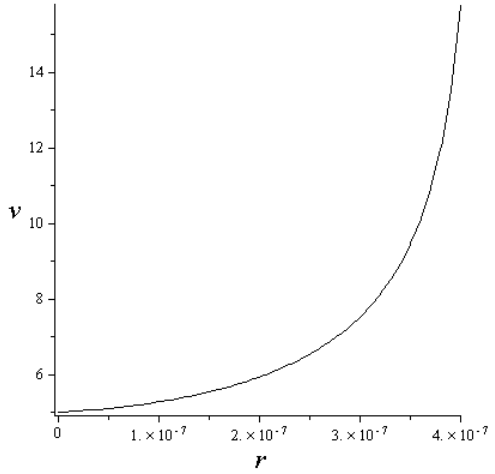

Figure 2.6.1. Numerical solution of the reduced form first order ODE (2.62). (Inverse of velocity "v" versus displacement "r")

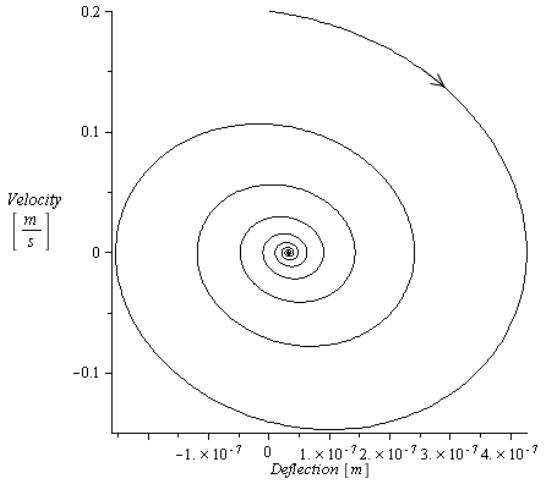

Figure 2.6.13. Phase diagram of the second order ODE and the reduced first equations (2.61) and (2.62)

The phase diagram indicates perfect overlapping of the solution of the second order ODE and first reduced order ODE. The time domain plot in figure 2.6.4 confirms the perfect matching of the solutions of the reduced equation and the initially considered form.

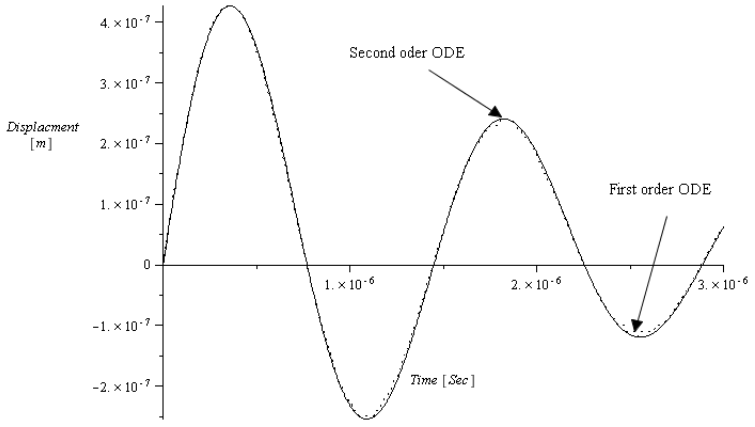

Figure 2.6.14. Numerical solutions for the second order ODE (2.61) and first reduced order ODE (2.62)

2.7. Effective stiffness

One can model vibration of cantilever with vibration of mass-damper-spring model which has a one degree of freedom, as illustrated in figures 2.1.1 and 2.1.2. For this purpose, one has to define equivalent effective stiffness and damping for the model. In some prior work [112] effective stiffness for a cantilever under the electrostatic force is defined. In the current work, effective stiffness is used to model stiffness of the deflection of cantilever as mass-spring-damper model. Equivalent stiffness is used also to evaluate the dynamic performance of the micro-systems. The effective stiffness for distributed force is defined in [112] as:

$$K_{eff} = \frac{2}{3}\frac{E^* b h^3}{l^3} \tag{2.63}$$

where:

$$E^* = \frac{E}{1-\nu^2} \tag{2.64}$$

E is Young's modulus

ν is Poisson's ratio

b is width of the beam

h is thickness of the beam

l is length of the beam

Based on the effective stiffness, pull-in voltage can be calculated like equation (2.60), but with effective values as [112]:

$$V_p = \sqrt{\frac{8K_{eff}g^3}{27\varepsilon_0 A_{eff}}} \tag{2.65}$$

where:

g is gap distance

ε_0 is the absolute permittivity

A_{eff} is effective area

where, from [112] :

$$A_{eff} = \alpha b_{eff} l \tag{2.66}$$

With:

$$b_{eff} = b(1 + 0.65\frac{(1-\beta)d}{b}) \tag{2.67}$$

$$\alpha = \frac{4}{\pi}\frac{1-\beta}{\sqrt{1-2\beta}}\,Arc\tan(\sqrt{1-2\beta}) \tag{2.68}$$

$$0.33 \le \beta \le 0.45 \tag{2.69}$$

The value of β is reselected to range between the two values in (2.69) as proposed in [123].

2.8. Nonlinear behavior and pull-in voltage

Pull-in voltage has widely been investigated [92, 93, 96, 101, 109, 112, 124, 125] . Pull-in voltage is studied based on linearization [125] of the equation (2.3), whereas nonlinear pull-in voltage was calculated in this paper based on the solution of equations (2.3) and (2.55). Comparison between linear and nonlinear analysis shows significant difference between the values in the pull-in voltage yield by the solution of two models. The difference increases by increasing the gap distance. For the micro-cantilever beam, specified in section 4, the pull-in voltages of linear and nonlinear analyses are illustrated in the figure 2.8.1. The numerical values are given in table 2.8.1. In this table, for each gap distance pull-in voltage was calculated by seven different methods. Second column (linear) shows the pull-in voltage based on equation (2.60). Third column (DCNF-Discontinue-Cantilever-Natural-Frequency) shows the pull-in voltage value based on equation (2.3) or (2.55) where $\omega_n = \sqrt{\frac{k}{m}}$, $k = \frac{3EI}{l^3}$. Fourth column (CCNF- Continue-Cantilever-Natural-Frequency) gives the pull-in voltage derived from equation (2.3) or

(2.55) by assuming $\omega_n = 3.515625\sqrt{\frac{EI}{ml^3}}$. Fifth and seventh columns represent the pull-in voltages derived by equation (2.65) for $\beta = 0.33$ and $\beta = 0.45$ respectively. Sixth and eighth columns give the pull-in voltages from equation (2.3) or (2.55) by modifying the area by equation (2.66). As expected and as it can be seen from figure 2.8.1, DCNF in all cases yield results significantly different from the other models. Nonlinear analysis of CCNF model yields the maximum values for the pull-in voltage and the results come almost same as the modified for $\beta = 0.45$ from the equation (2.3) or (2.55). For modified models, in any case the equation gives slightly higher value than nonlinear analysis. Figure 2.8.1 also reveals that DCNF model predicts smallest pull-in voltage when compared to the other models whereas the modified $\beta = 0.45$ yields the largest pull-in voltage. For small gaps, the CCNF model predicts pull-in voltage less than modified $\beta = 0.45$ but by increasing the gap distance the pull-in voltage by CCNF will be higher than the modified $\beta = 0.45$. This is illustrated in second graph of figure 2.8.1 which is a close-up of the indicated region in first graph of figure 2.8.1. This finding is consistent with the dependency of the beam stiffness of various models on the applied potential (figures 2.8.5, 2.8.9, 2.8.13, 2.8.17 and 2.8.21). The figures show that CCNF model yields the stiffest structure while DCNF produces the least stiff structure regardless the gap. Modified $\beta = 0.45$ model yields stiffer systems than the modified $\beta = 0.33$ model. The above is confirmed by the resonant frequencies predicted by the models when structures are subjected to low electrostatic forces. Thus, CCNF model exhibits highest natural frequency while DCNF shows the smallest natural frequency.

The behavior of the system close to pull-in voltage is another aspect that is studied in this work. For the specific micro-cantilever and gap distances, introduced in section 2.8, in figures 2.8.2-2.8.29, four sets of results are shown for these gap distances. These four sets are: the time response of the system under the application of a step potential close to the pull-in voltage, the phase portrait for the applied potential 99.999% very close of the pull-in voltages, deflection under various voltages for different models and resonant frequency variation yield by each of the four selected models with the potential which is perceived as a loss of stiffness of the structure under the application of the potential (weakening phenomena yield by the selected models). These sets are calculated from the solution of equations either (2.3) or (2.55). It is important to mention that equation (2.55) enables extraction of the phase portrait of an easy fashion while same output through equation (2.3) would prove quite laborious. The solutions of each of the four models were derived and plotted. Each graph has four sets of solutions and each set represents the solution of one model. The time domain solution of the ODE describing the dynamics of a microsystems such as a micro-cantilever beam subjected to electrostatic forces reveal interesting trend that has different aspect than the one reported in the open literature. Figure 2.8.2 illustrates the time response of the four selected models for the gap of 2 μm: DCNF (7.1V), CCNF (14.5[V]), non-linear modified $\beta = 0.33$ (14.3[V]) and non-linear modified $\beta = 0.45$ (14.6[V]). It is seen that after the potential is applied, the system responds with a ramp followed by a flat which is same for all models (deflection representing 4/9 or 45% of the initial gap). It is important to mention here that the quasi-static analysis yield a unique limit position that corresponds to a deflection of 1/3 of the original gap [126]. The duration of the flat which is a saddle point in the stability of the structure is dependent on the model. Thus, the duration of the marginal stability is inverse

proportional with the instant stiffness; lower stiffness yields longer duration to settlement. Once the system leaves the marginal stability seen in the phase portrait as the saddle point, the equilibrium position is attain regardless the model in a position representing 2/9 of the initial gap or half of the marginal stability position. Although CCNF model proves to exhibit the lowest resonant frequency at the applied potential, this is due to the fact that the rate of decay of the resonant frequency of the CCNF model is higher than of the other models. It is important to mention that if the critical voltage is assumed in any of the models, no solution is found.

Table 2.8.1. Pull-in voltage in linear and nonlinear analysis

Gap distance [μm]	Linear model [V]	DCNF [V]	CCNF [V]	Modified $\beta = 0.33$ [V]	Non linear Modified by $\beta = 0.33$ [V]	Modified $\beta = 0.45$ [V]	Non linear Modified by $\beta = 0.45$ [V]
2	7.52	7.17	14.57	14.36	13.69	15.38	14.66
4	21.27	20.28	41.22	39.80	37.95	42.78	40.79
6	39.80	37.26	75.73	71.70	68.36	77.32	73.72
8	60.17	57.37	116.59	108.33	103.28	117.16	111.71
10	84.09	80.18	162.94	148.66	141.74	161.24	153.73

Phase portraits in figure 2.8.3 show that the system described by the four models is still stable but it has developed sharp edge along the x-axis. This edge is the saddle point that is seen in the time response as a flat at the peak deflection point or as previously described as the marginal stability duration. Table 2.8.2 illustratess the crytical distance, which is independent on the selectd model, at which the poll-in occurs as calculated through the present formulation.

Table 2.8.2. Pull-in distance

	2 µm	4 µm	6 µm	8 µm	10 µm
Pull-in distance	0.9 µm	1.8 µm	2.7 µm	3.6 µm	4.5 µm
Ratio	45%	45%	45%	45%	45%

All phase diagrams regardless the model show the saddle point at the critical pull-in distance. Further, the plot indicates a convergence point which is the settling position as illustrated in figure 2.8.2 The settlement distance represents 50% of the pull-in distance. The maximum velocity occurs in DCNF whereas minimum velocity is encountrerd in CCNF while velocities of the modified models are sensitively similar.

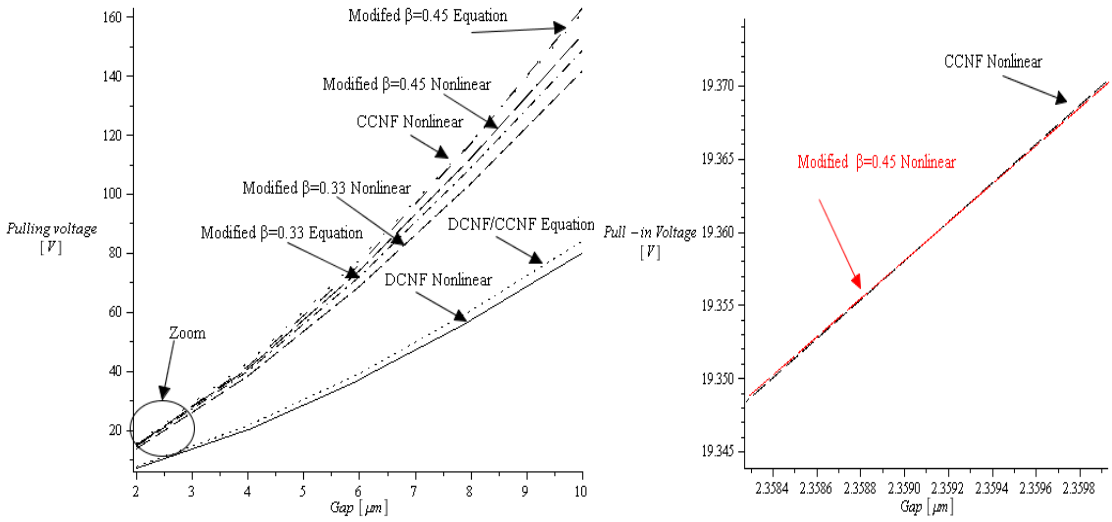

Figure 2.8.1. The pull-in voltage for different gap distance and various models under discussion

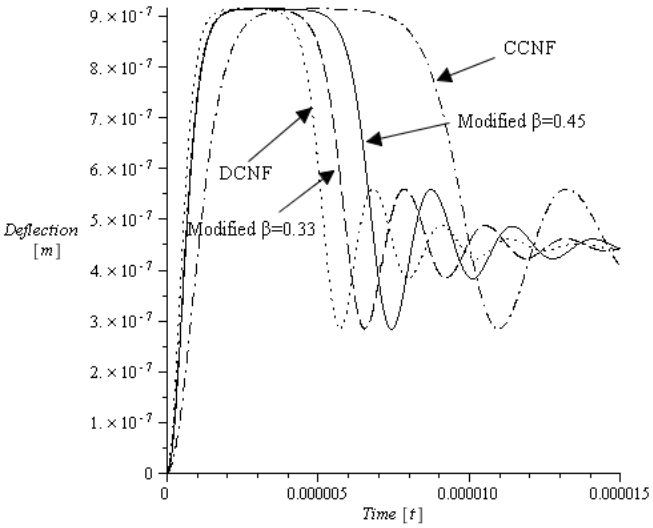

Figure 2.8.2. Time response of the system near the pull-in voltage for the four selected models (gap= 2 μm)

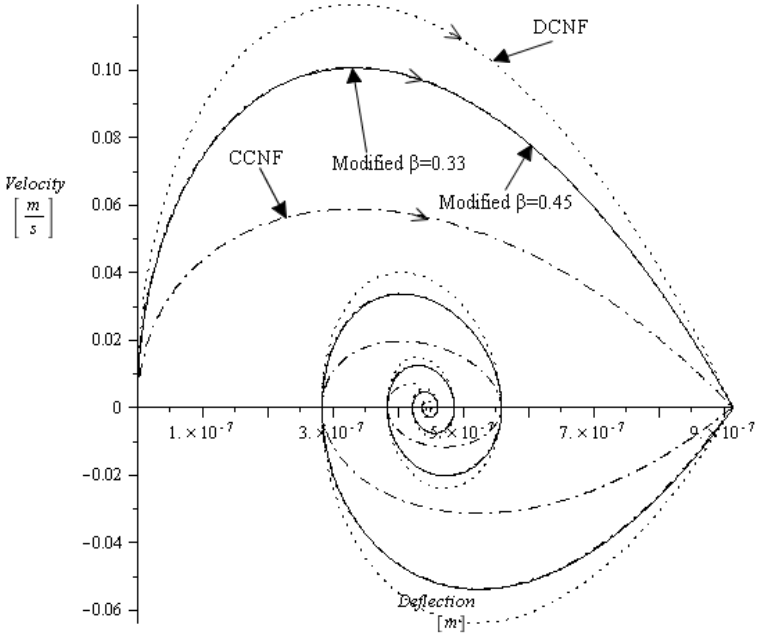

Figure 2.8.3. Phase portrait of the four models for potentials near the pull-in voltage (gap= 2 μm)

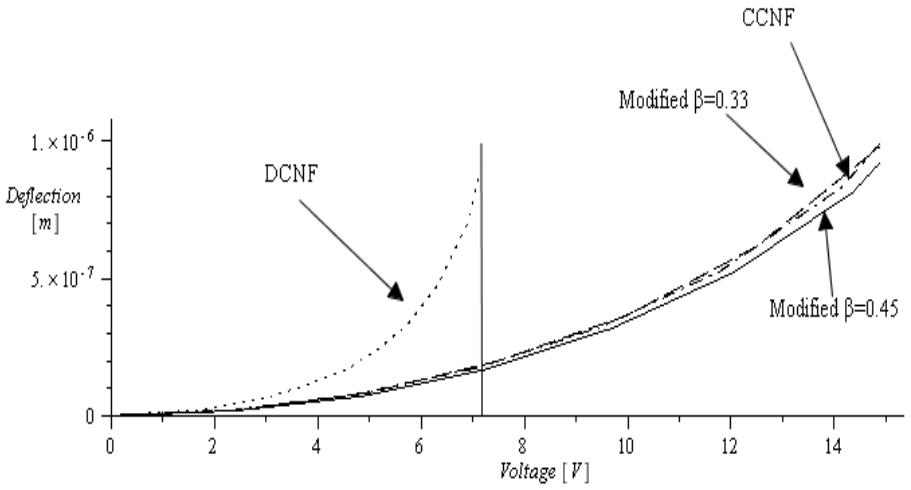

Figure 2.8.4. Dependency of the deflection with the applied voltage for the four different models (gap= 2 μm)

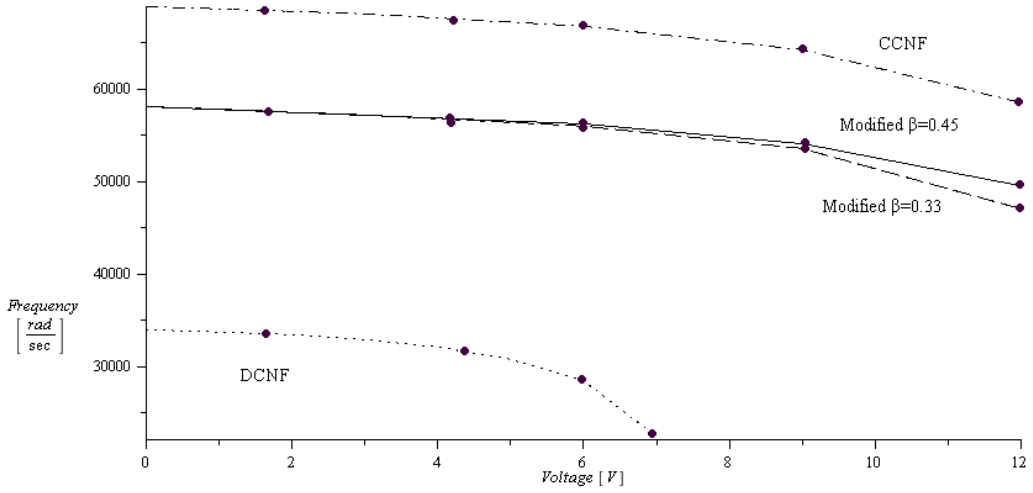

Figure 2.8.5. Variation of the resonant frequency of the system for the four models with the applied voltage (gap= 2)

The structure deflects when subjected to a difference of potential, as illustrated in figure 2.8.4. The four models yield different deflections for same potential difference. DCNF model exhibit the highest deflection. However, the pull-in voltage exhibited by this model is closer to the linear model and about half of any other three discussed models. The other three models (CCNF, modified $\beta = 0.33$ and $\beta = 0.45$) exhibit the pull-in voltage to similar values. The deflection increases with the applied potential. The least

deflection is exhibited by the modified $\beta = 0.45$ and the most by the modified $\beta = 0.33$. The plot showing the resonant frequency of the system according to the formulations of the four models is illustrated in figure 2.8.5 CCNF model yields the highest resonant frequency, which comes consistent with the other findings. The modified models yield about same resonant frequency and similar pull-in voltage. The resonant frequency of the two models branches out when the structure is subjected to potentials closer to the pull-in voltage. The modified $\beta = 0.45$ reduces less than modified $\beta = 0.33$ and the difference grows once the models are to potentials closer to the pull-in voltage. The DCNF model exhibits significantly the lowest resonant frequency.

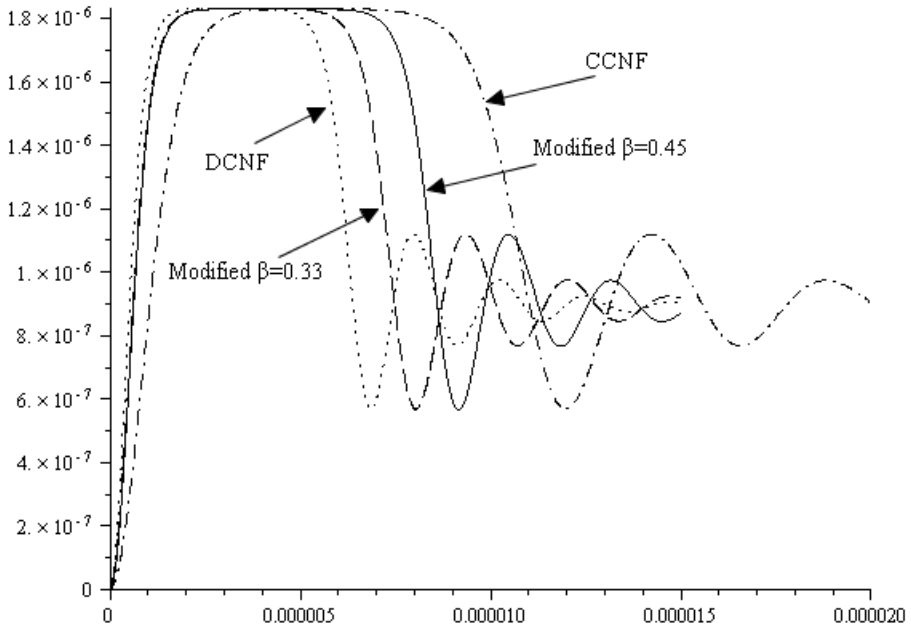

Figure 2.8.6. Time response of the system near the pull-in voltage for the four selected models (gap= 4 μm)

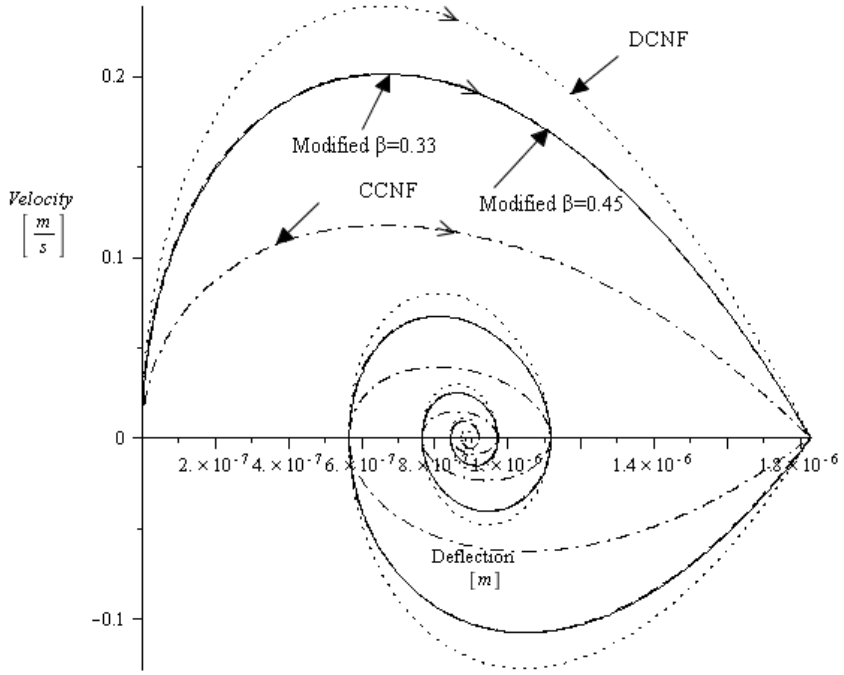

Figure 2.8.7. Phase portrait of the four models for potentials near the pull-in voltage (gap= 4 μm)

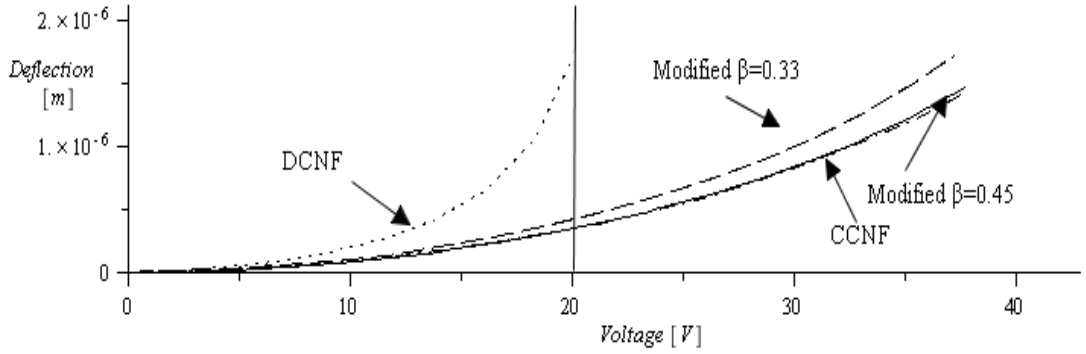

Figure 2.8.8. Dependency of the deflection with the applied voltage for the four different models (gap= 4 μm)

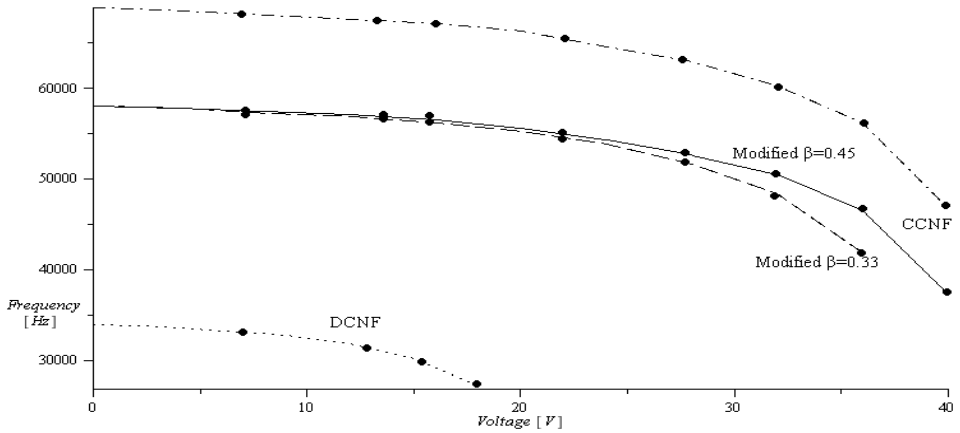

Figure 2.8.9. Variation of the resonant frequency of the system for the four models with the applied voltage (gap = 4 μm)

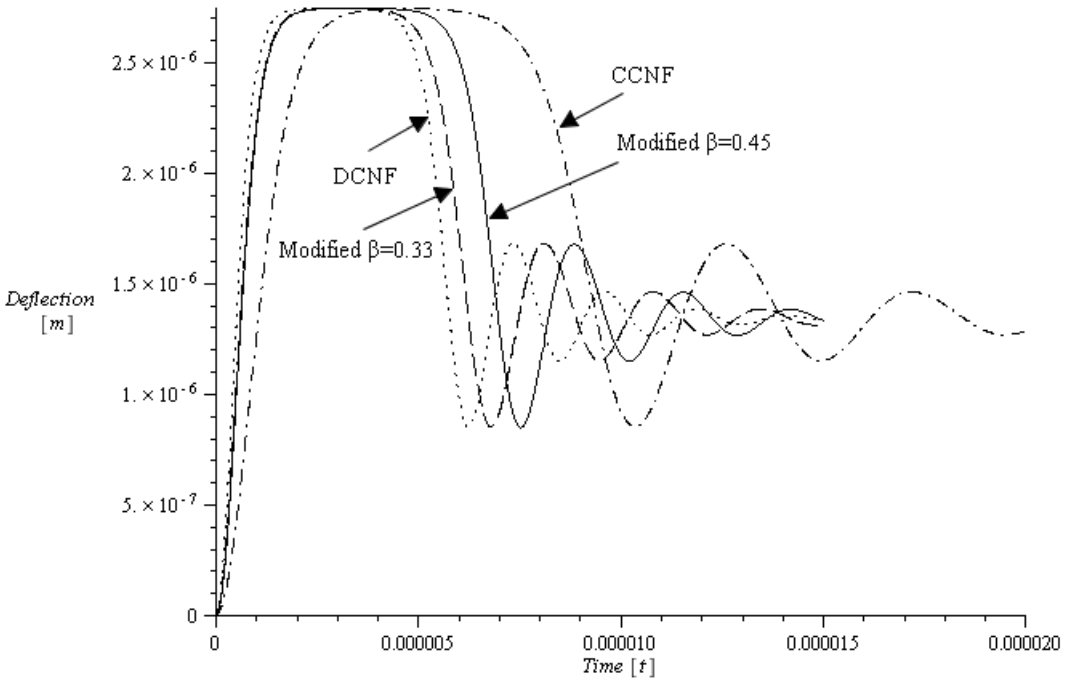

Figure 2.8.10. Time response of the system near the pull-in voltage for the four selected models (gap= 6 μm)

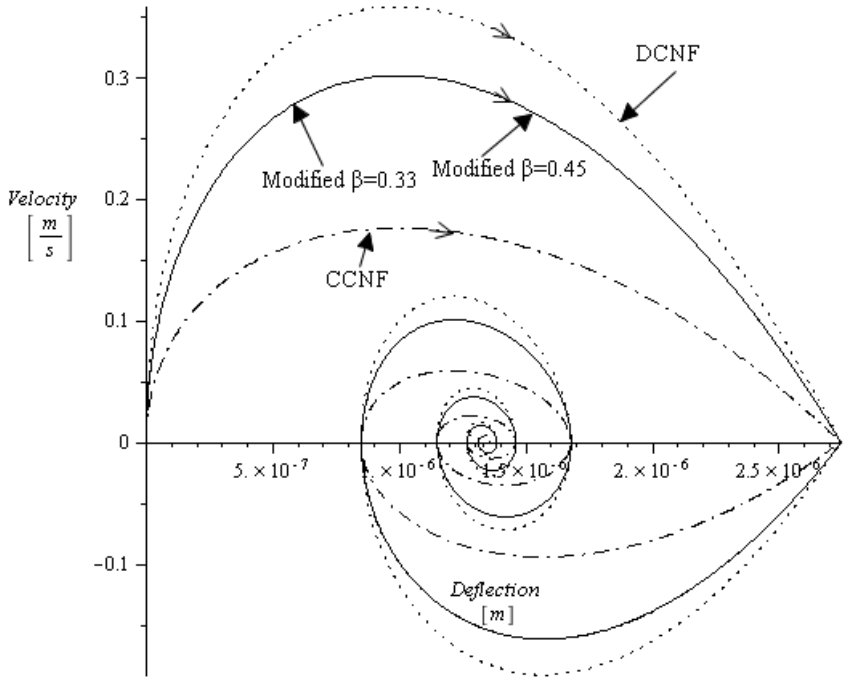

Figure 2.8.11. Phase portrait of the four models for potentials near the pull-in voltage (gap= 6 μm)

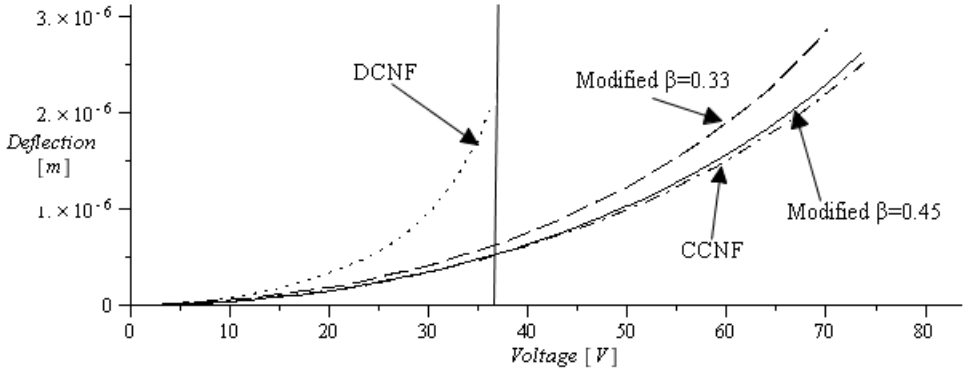

Figure 2.8.12. Dependency of the deflection with the applied voltage for the four different models (gap= 6 μm)

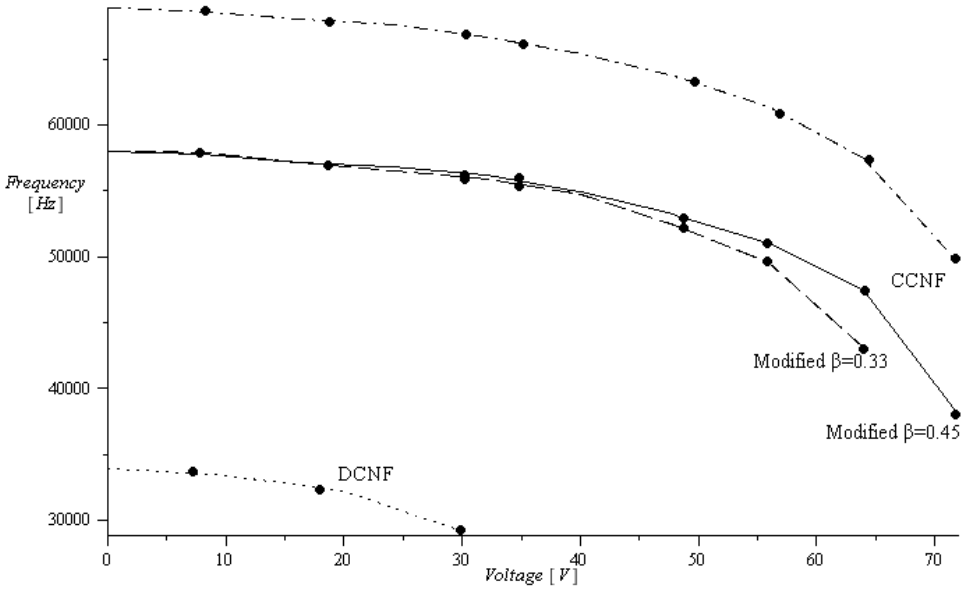

Figure 2.8.13. Variation of the resonant frequency of the system for the four models with the applied voltage (gap = 6 μm)

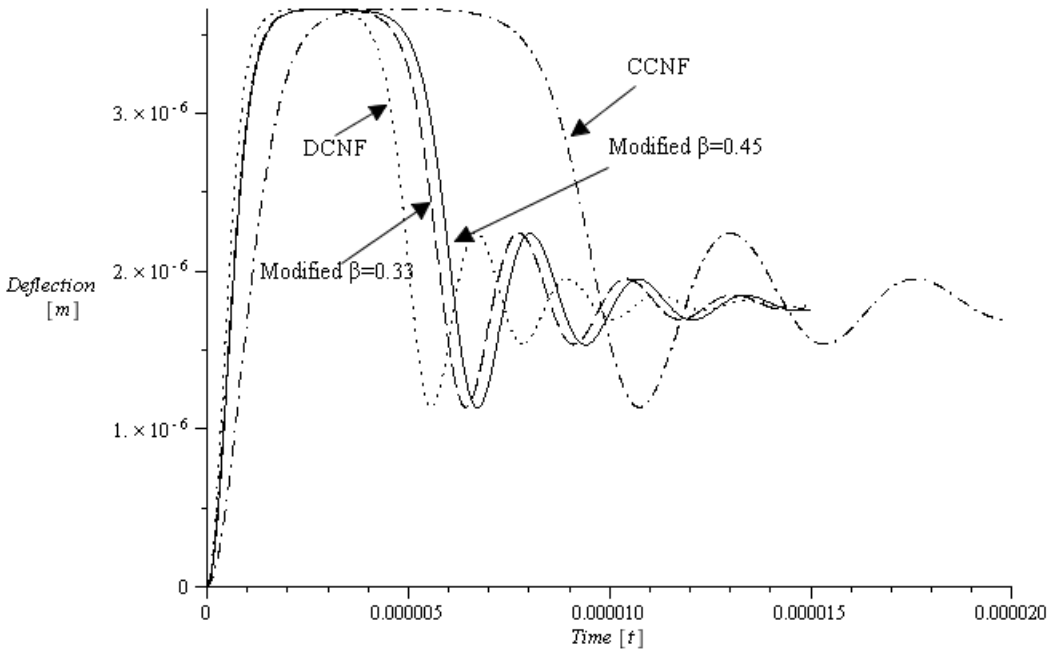

Figure 2.8.14. Time response of the system near the pull-in voltage for the four selected models (gap= 8 μm)

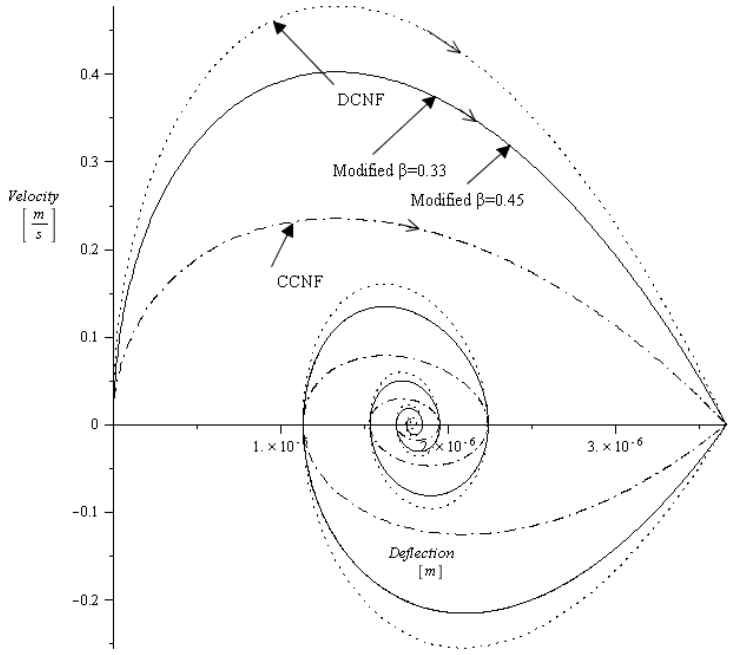

Figure 2.8.15. Phase portrait of the four models for potentials near the pull-in voltage (gap= 8 μm)

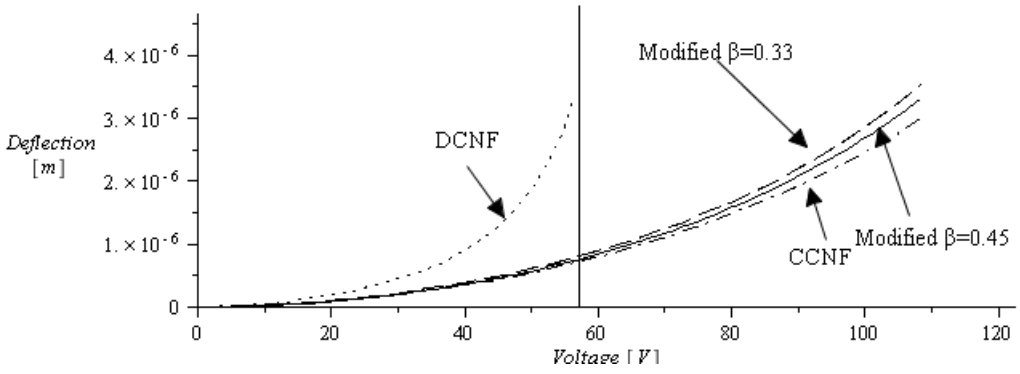

Figure 2.8.16. Dependency of the deflection with the applied voltage for the four different models (gap=8 μm)

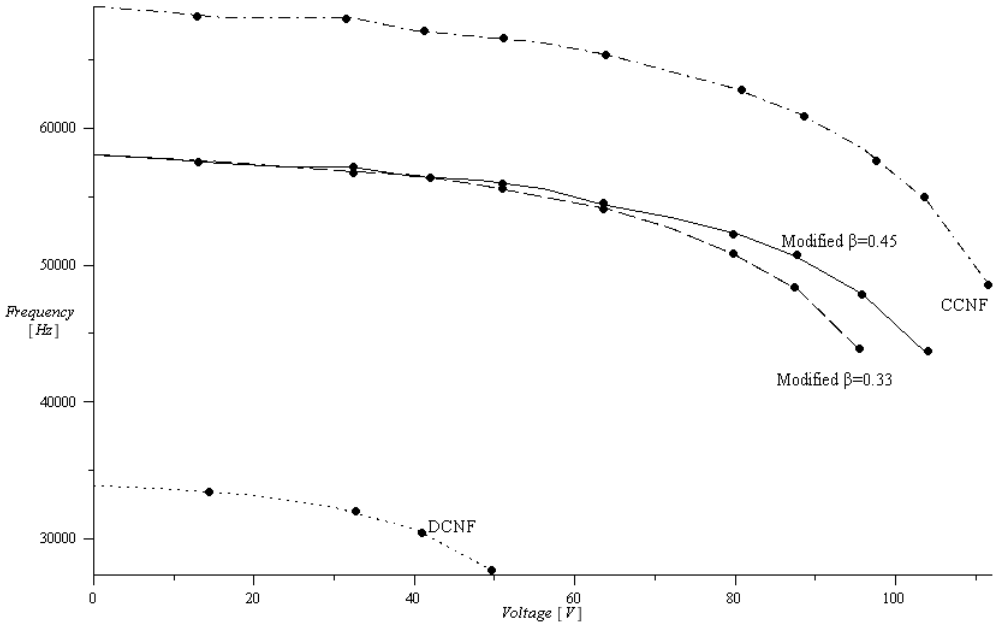

Figure 2.8.17. Variation of the resonant frequency of the system for the four models with the applied voltage (gap = 8 μm)

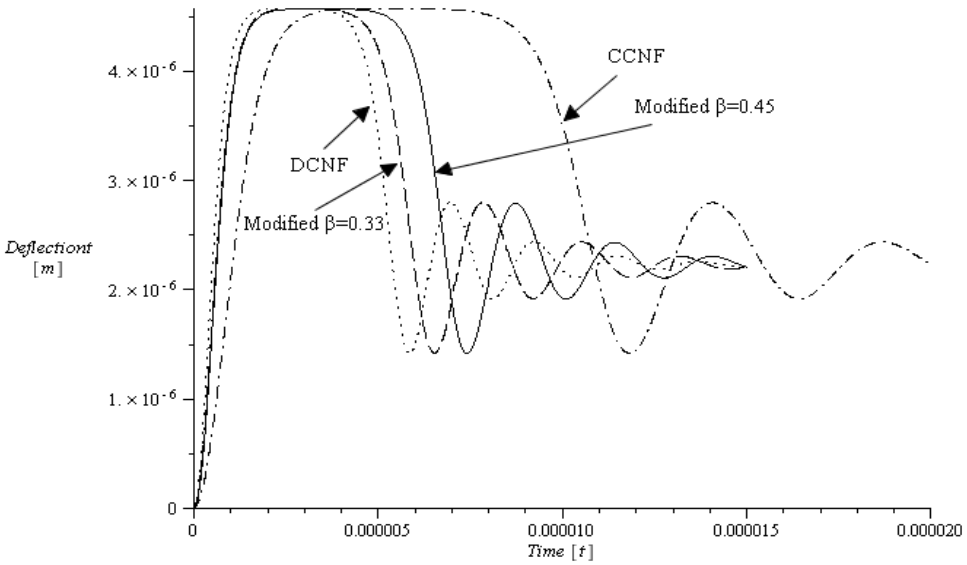

Figure 2.8.18. Time response of the system near the pull-in voltage for the four selected models (gap= 10 μm)

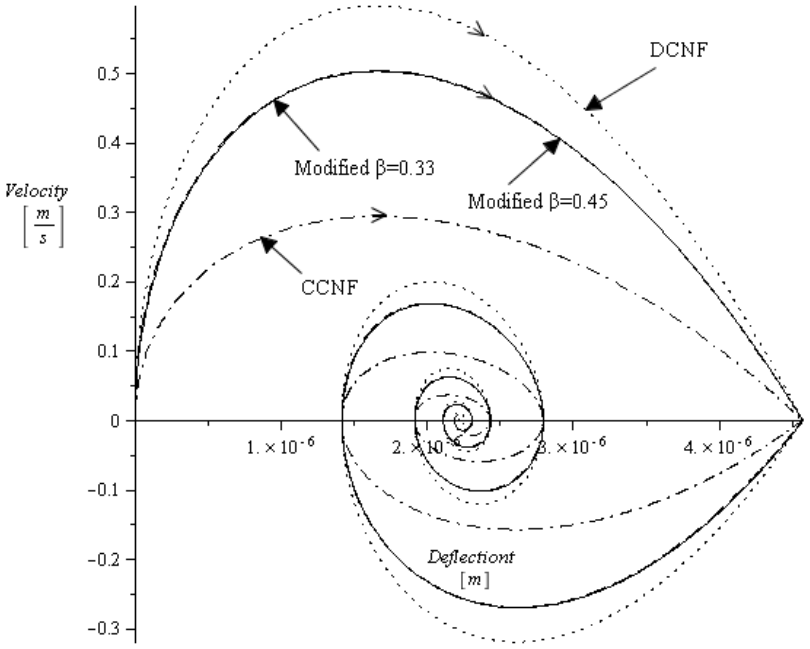

Figure 2.8.19. Phase portrait of the four models for potentials near the pull-in voltage (gap= 10 μm)

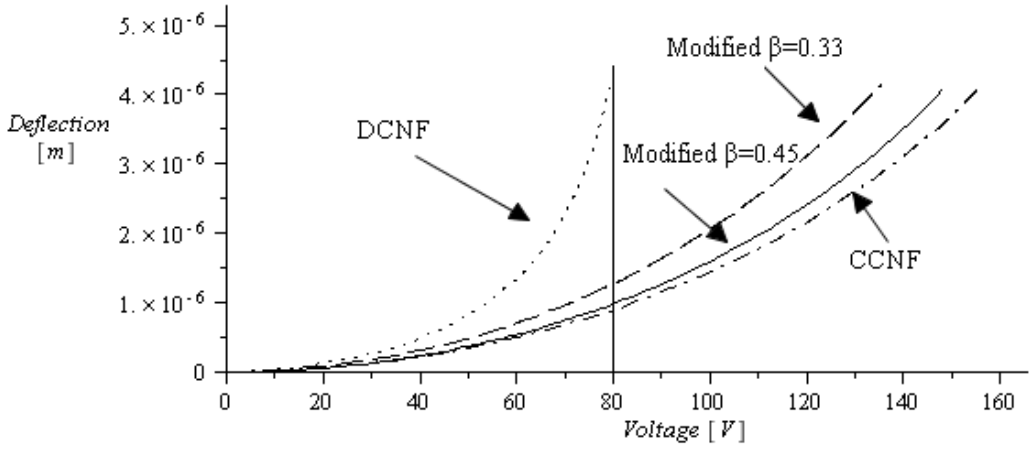

Figure 2.8.20. Dependency of the deflection with the applied voltage for the four different models (gap= 10 μm)

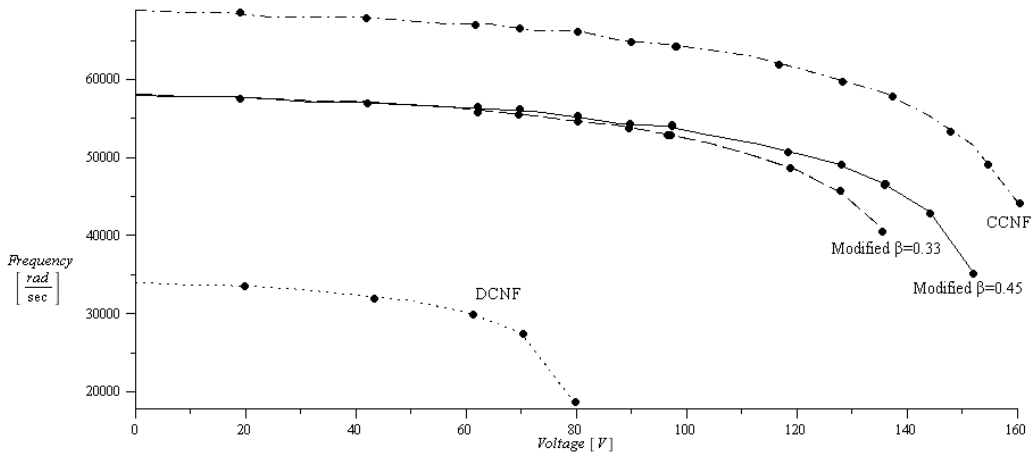

Figure 2.8.21. Variation of the resonant frequency of the system for the four models with the applied voltage (gap = 10 μm)

Further, figures 2.8.6 to 2.8.21 illustrate the same data as figures 2.8.2 to 2.8.5 but for assumed gap of 4, 6, 8 and 10 [μm]. The pull-in voltage values for the four models and the assumed gap are as those given in table 2.8.1 For the maximum assumed gap distance, the pull-in voltage for DCNF and CCNF increases a little more than 11 times while for the two modified models with $\beta = 0.33$ and $\beta = 0.45$ a bit more than 10 times. Figure 2.8.18 shows that the duration of the marginal stability of CCNF model significantly increases while for the other three models remains about same. This may be due to the fact that the assumed potential for the CCNF case (162.9[V]) is closer to the pull-in voltage than the voltage assumed for 2 [μm] gap. The phase portrait illustrated in figure 2.8.19 is similar with the one plotted for 2 [μm] gap. It is important to mention that the dynamic behavior of the system regardless the model is same. Once the potential close to the pull-in voltage is applied, the structure ramps to a deflection corresponding to 4/9 of the initial gap, and then settles in equilibrium position which corresponds to a deflection of 2/9 of the initial gap. The deflection vs. applied potential illustrated in figure 2.8.20 is similar in trend with that of the model in which the gap was assumed at 2 [μm]

except that the lowest deflection for the same potential is performed by the CCNF model. The dependence of the natural frequency with the applied potential for 10 [μm] gap is illustrated in figure 2.8.21 Similarly as in figure 2.8.5, DCNF model yields the lowest resonant frequency while CCNF the highest.

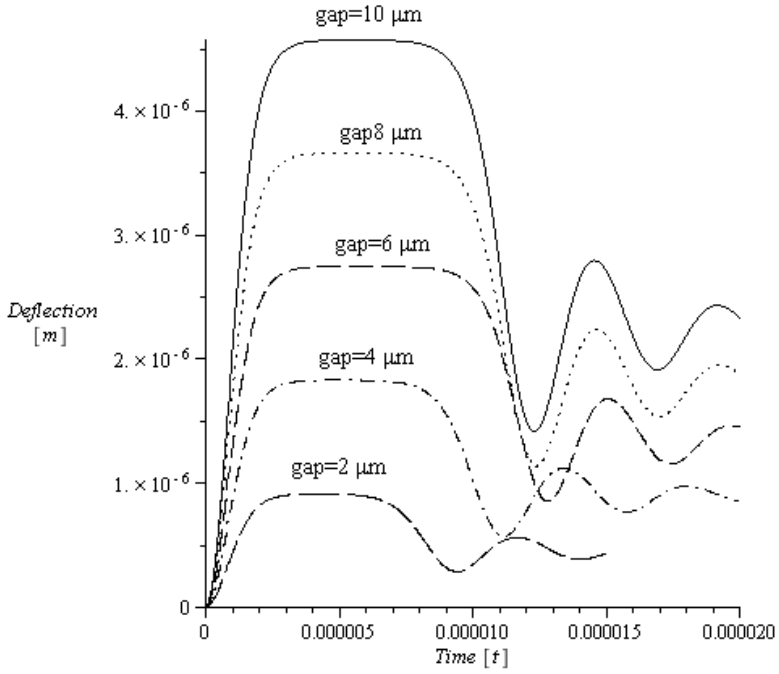

Figure 2.8.22. Dependency of the time response of the DCNF model for various gap distances at applied potentials close to the pull-in voltage.

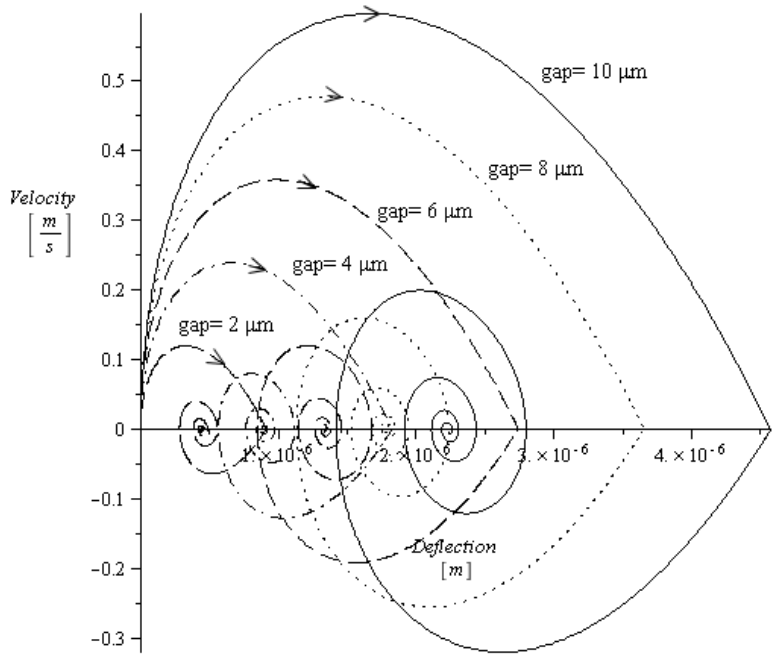

Figure 2.8.23. Phase portraits of the DCNF model for various gaps at potentials close to the corresponding pull-in voltages

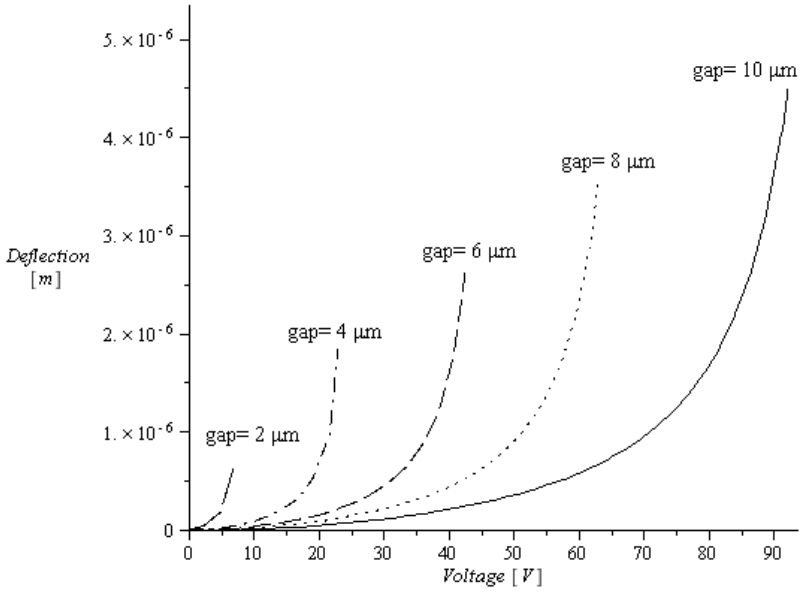

Figure 2.8.24. Voltage vs. deflection in DCNF model for different gaps

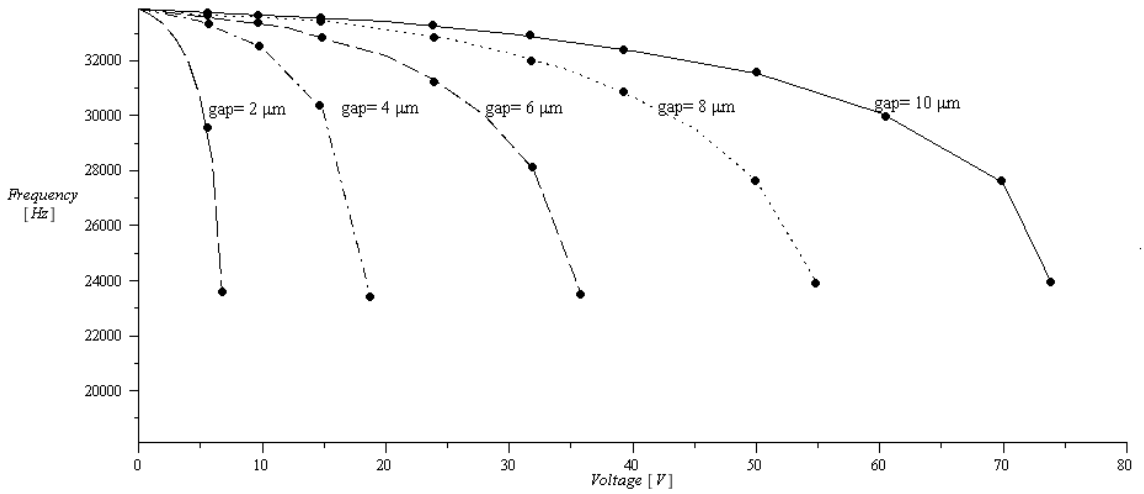

Figure 2.8.25. Variation of the frequency with the applied potential for different gap separation for DCNF model

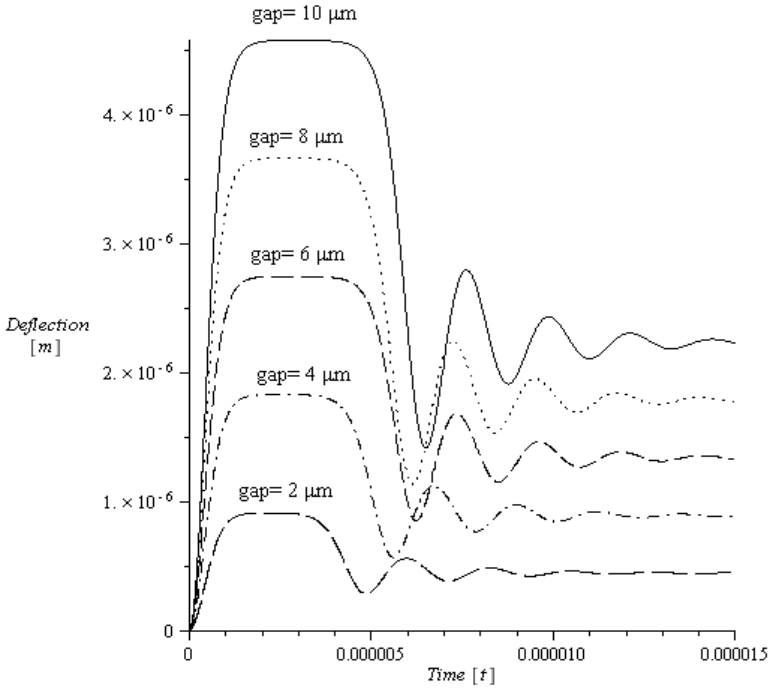

Figure 2.8.26. Effect of gap on time response in CCNF model

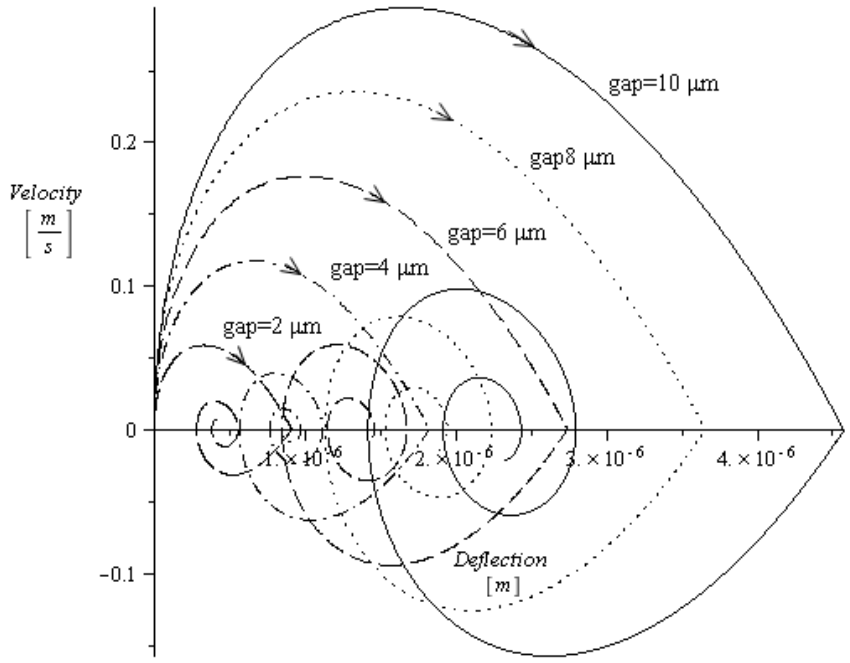

Figure 2.8.27. Effect of gap on phase diagram in CCNF model

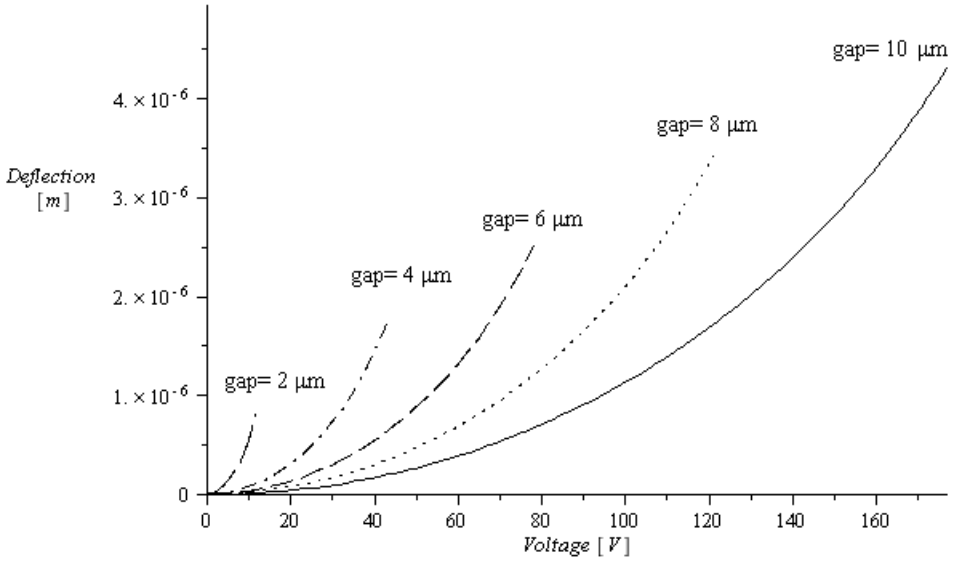

Figure 2.8.28. Voltage vs. deflection in CCNF model for different gaps

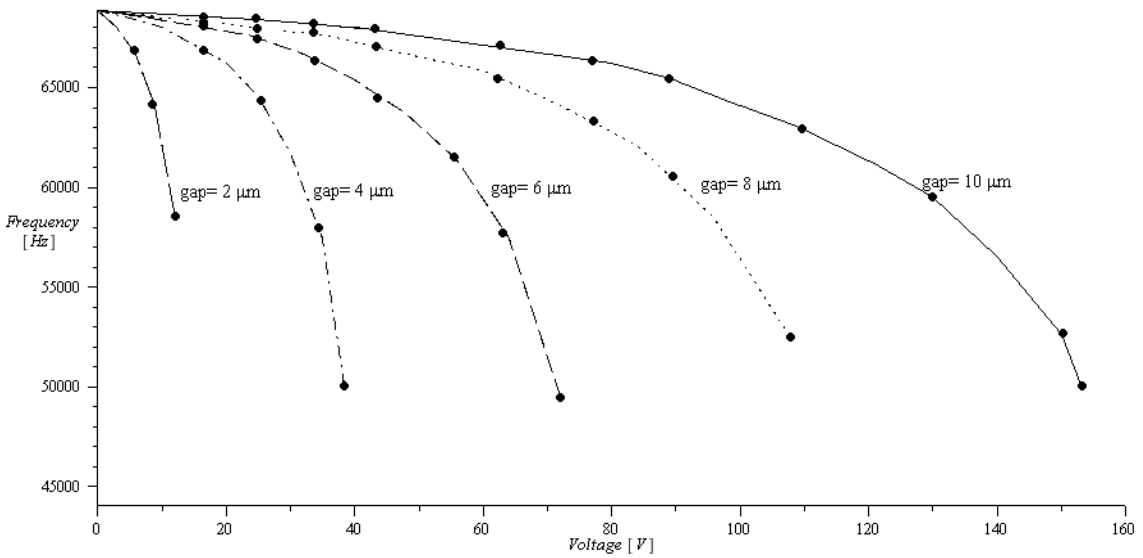

Figure 2.8.29. The variation of the frequency with the applied potential for different gap separation for CCNF model

A parametric study to study the influence of the gap on the time response, critical position and equilibrium position, deflection vs. applied potential and variation of the resonant frequency is carried out for each of the four considered models. However, the results of models are presented in figures 2.8.22 to2.8.37. The general conclusion of the findings is that regardless the selected model and the gap choice, once a potential close enough to the pull-in voltage is applied to the micro-system, the mobile restoring element will ramp, saddle always at the same position which is 4/9 of the initial gap, and will settle in an equilibrium position which corresponds to a deflection of 2/9 of the initial gap and is always same, regardless the model. The duration of the marginal stability for the system is dependent on the effective stiffness of the system which valueis highly sensitive with the applied potential when approaching the pull-in voltage. Thus, the duration of the marginal equilibrium for example in figure 2.8.22, is found to be irrelevant as a slight increase with the gap from 2 to 6 µm and a slight decrease back

form 6 to 10 μm is observed. Closer is the applied voltage to the pull-in voltage, longer is the marginal stability period. The phase portrait for all assumed gap values provides same information as above and the results are illustrated in figures 2.8.3,2.8.7,2.8.11 and 2.8.15. The variation of the deflection with the applied potential illustrated in figures 2.8.4, 2.8.8, 2.8.12 and 2.8.16 show a strong non-linear dependence of the deflection with the potential for any gap value. Hovever, for low potential a linear dependency of the deflection with the voltage is noticed for a range of about 50% o of the pull-in voltage. The resonant frequency of the system is dependent of the model and on the applied potential. For the DCNF model, the resonant frequency of the system decays with the applied potential, faster for the lower gaps. However, the frequency drops significantly when the applied potential is approaching the corresponding value of the pull-in voltage. The decrease is insignificant for only for applied potentials that are remote form the pull-in voltage.

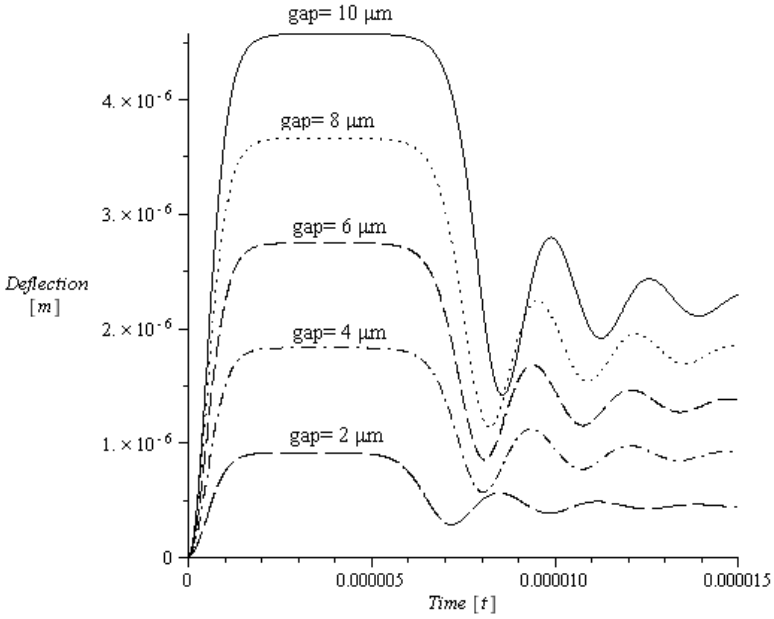

Figure 2.8.30. Effect of gap on time response in Modified β=0.33 model

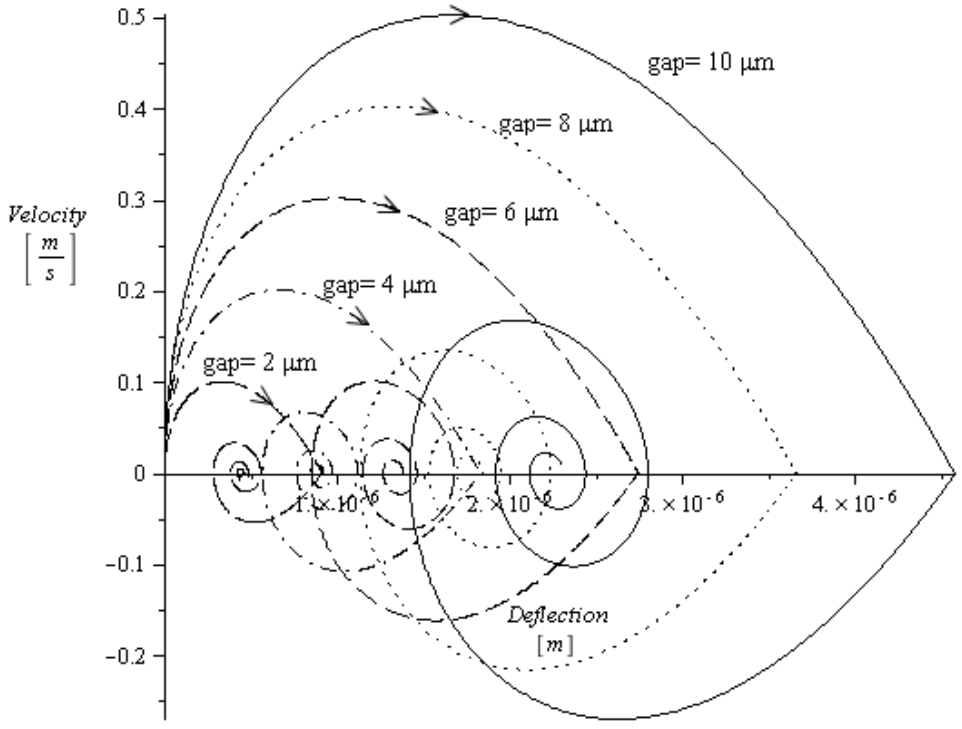

Figure 2.8.31. Effect of gap on phase diagram in β=0.33 model

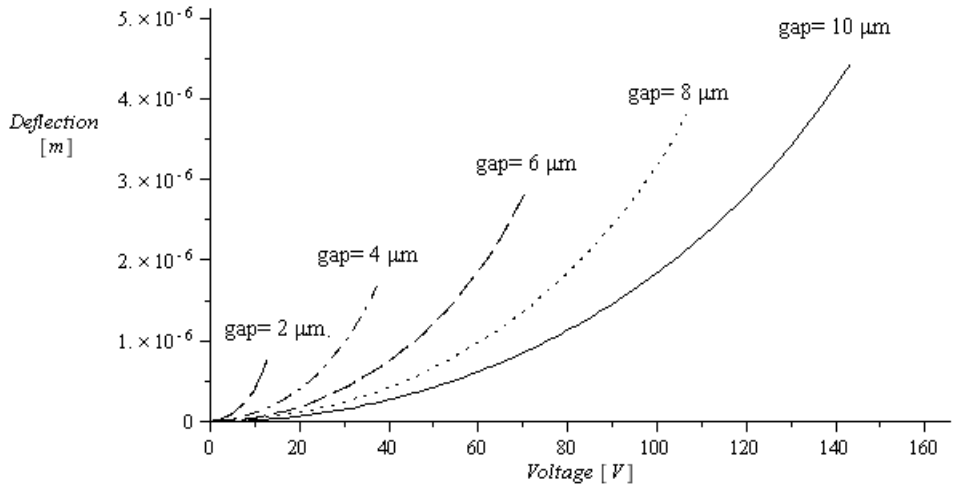

Figure 2.8.32. Voltage vs. deflection in Modified β=0.33 model for different gaps

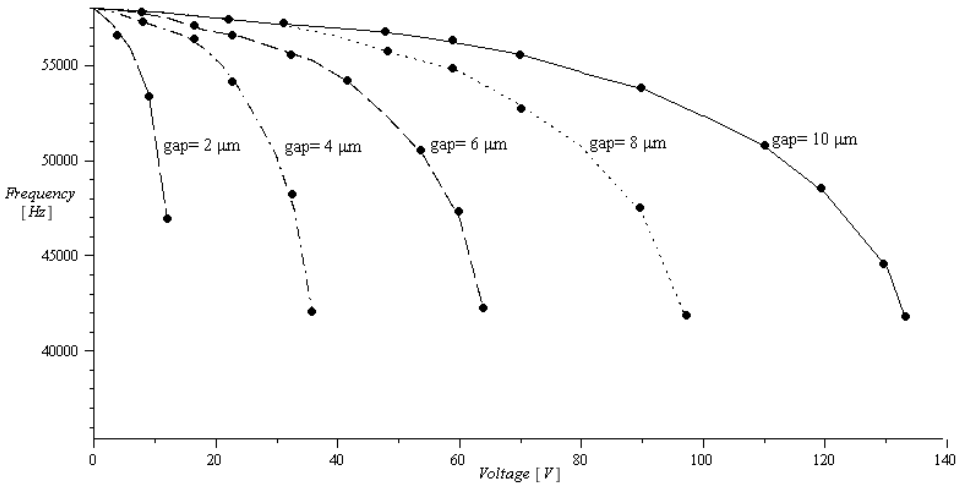

Figure 2.8.33. The variation of the frequency with the applied potential for different gap separation for β=0.33 model

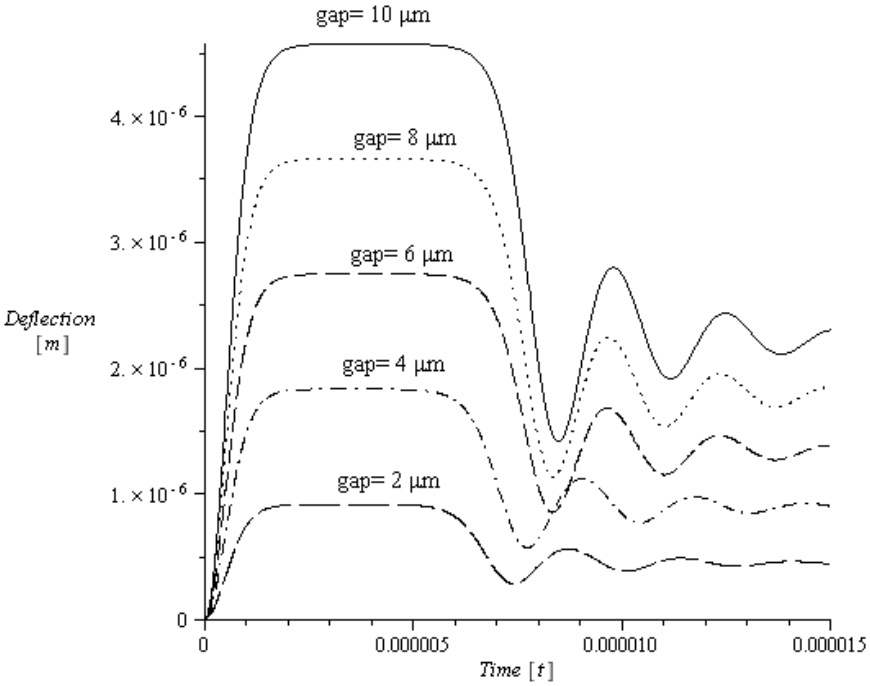

Figure 2.8.34. Effect of gap on time response in Modified β=0.45 model

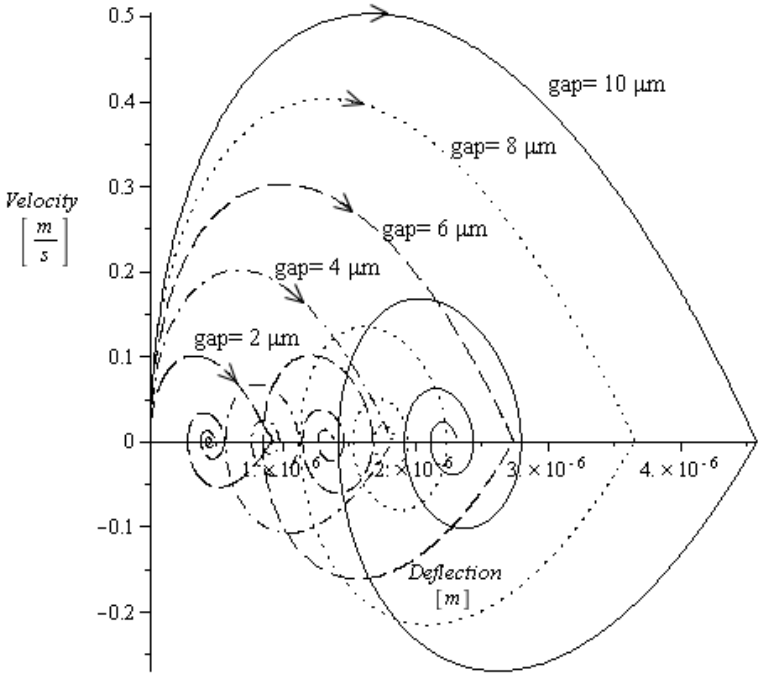

Figure 2.8.35. Effect of gap on phase diagram in β=0.45 model

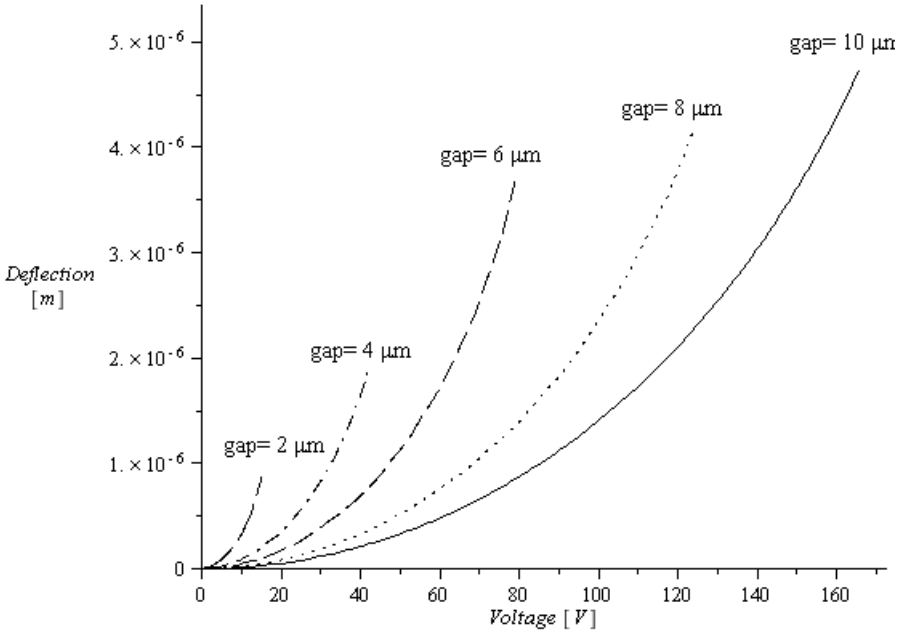

Figure 2.8.36. Voltage vs. deflection in Modified β=0.45 model for different gaps

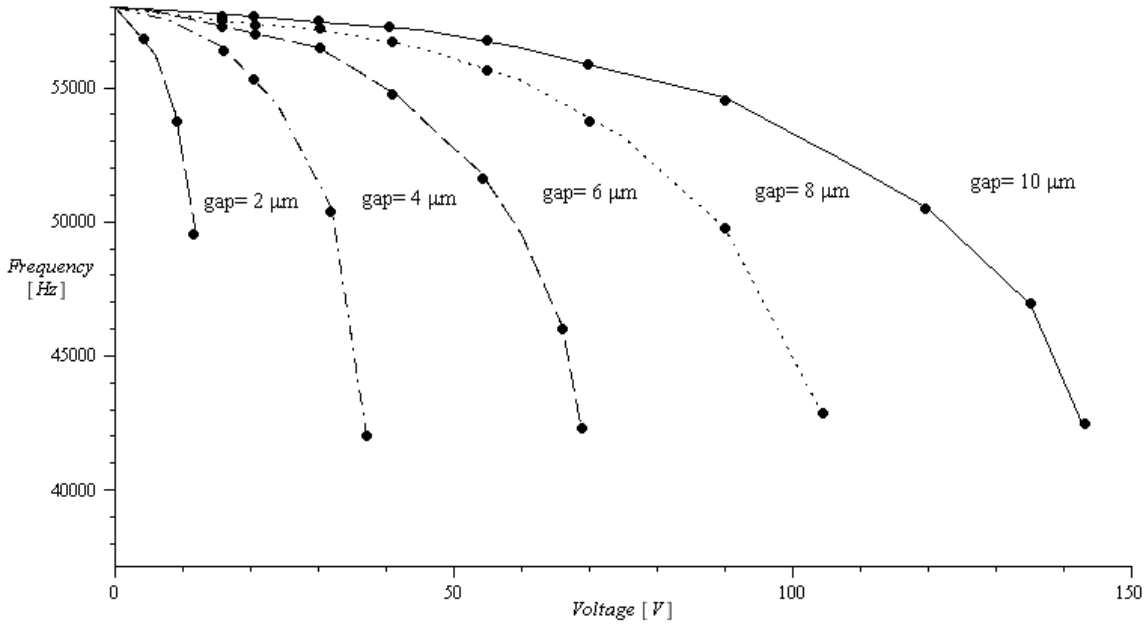

Figure 2.8.37. The variation of the frequency with the applied potential for different gap separation for β=0.45 model

2.9. Experimental validation

Sets of experiments to measure natural frequency and deflection of micro-cantilever beam subjected to electrostatic force were carried out in CONCAVE laboratories [127]. Figure 2.9.1 illustrates the setup of the experiment which includes a HeNe laser and photodiode detector in a laser vibrometer configuration, from Brüel & Kjær. The measurement system made use of an oscilloscope for the time-domain reference and a spectrum analyzer for frequency domain analysis. The micro-structures were excited with sweep harmonic oscillation produced by an audio speaker from the internal signal generator in the frequency analyzer. To measure the frequency response, a swept low amplitude harmonic excitation was used. The test was performed using non-contact measurement, by focusing the laser beam onto the substrate to extract the frequency response of the substrate. Then laser focused onto the micro cantilever while same swept frequency was applied. Finally, micro-cantilever response was calculated with respect to the base response. A DC power supply was used to obtain the deflection of micro cantilever and static deflection was measured under an optical microscope. The deflection was measured from the overlapped pictures of the deflected cantilevers when specific voltages were applied, as illustrated in figure 2.9.2. Two micro-cantilevers with dimensions as presented in table 2.9.1 were studied.

Table 2.9.1. Dimensions of beams

	Length [μm]	Width [μm]	Thickness [μm]	Young's modulus [MPa]
Beam I	351	34.5	0.94	169.5
Beam II	299	35	0.96	169.5

The resonance frequency of the beams subjected to the electrostatic forces was measured using the above-described procedure while a potential field was applied between the substrate and the beam and resonant frequency was determined for the various applied voltages.

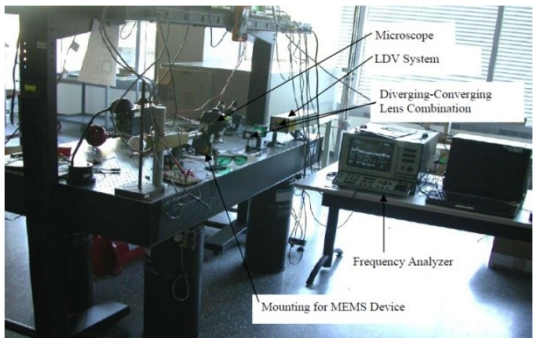

Figure 2.9.1. Experiment set up[127]

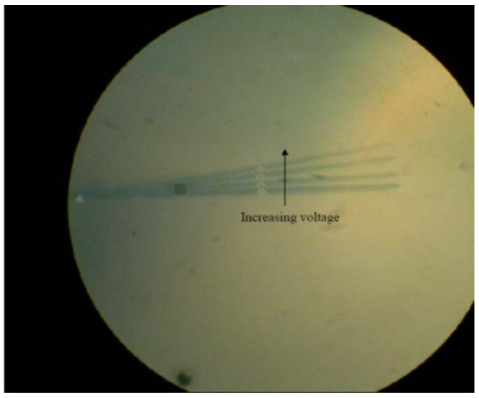

Figure 2.9.2. Positions of micro-cantilever under different applied potentials. The charged electrode (not seen in the picture) was positioned parallel to the micro-beam on the upper side of the picture[127]

The experimental and the calculated deflections under different voltages for two beams are illustrated in figures 2.9.3 and 2.9.4. For both beams, maximum applied voltage for measuring the static deflection was 500 [V]. The four different theoretical models, as detailed in section 2.8 were considered for validation. As illustrated, the best-fit curve for

beam I is for $\beta = 0.755$ and for beam II for $\beta = 0.73$. These values were calculated based on the minimizing the error. The error was calculated by relative error of theoretical deflection with respect to the experimental deflection for each voltage. Summation of squares of these errors was considered as target value to minimize. The range of the effective stiffness values as recommended in [125] are significantly higher than reported values in [112]. By increasing the value of β, the effective area decreases. If effective area decreases, the applied force will decrease. It is clear that by decreasing the force, deflection will decrease. In this experiment, deflection is large so the area under the electrostatic force will reduced; by reducing force deflection will also reduce. It will need to increase the value of beta to match the experimental results with one model. According to the theoretical presented models and considering the above mentioned values for beta, the modified model has proved to yield closer results to experimental values. However, the matching value for β is considerably higher than the range recommended in [112]. The modified model proves to be the most suitable with the experiment for matching the deflection of the micro-cantilever beam.

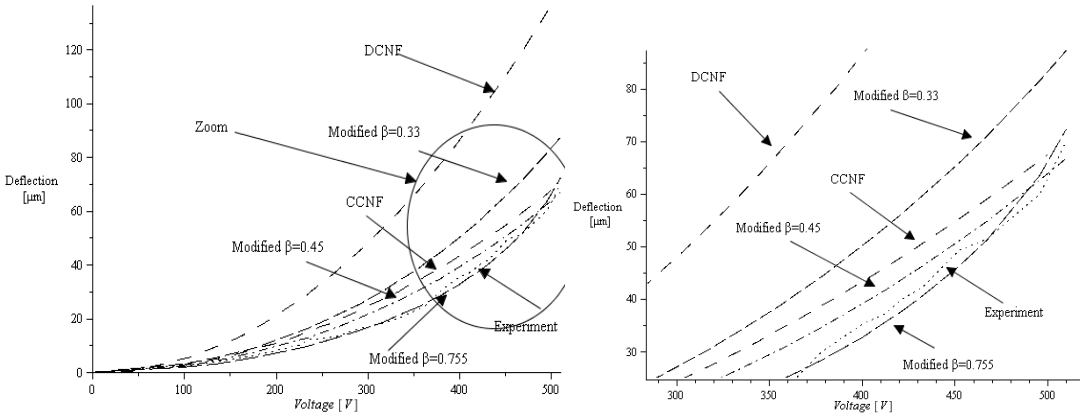

Figure 2.9.3. a) Deflection as a function of the applied potential; theoretical and experimental values of the deflection of the micro-cantilever beam I; **b)** Zoom-in of the indicated zone

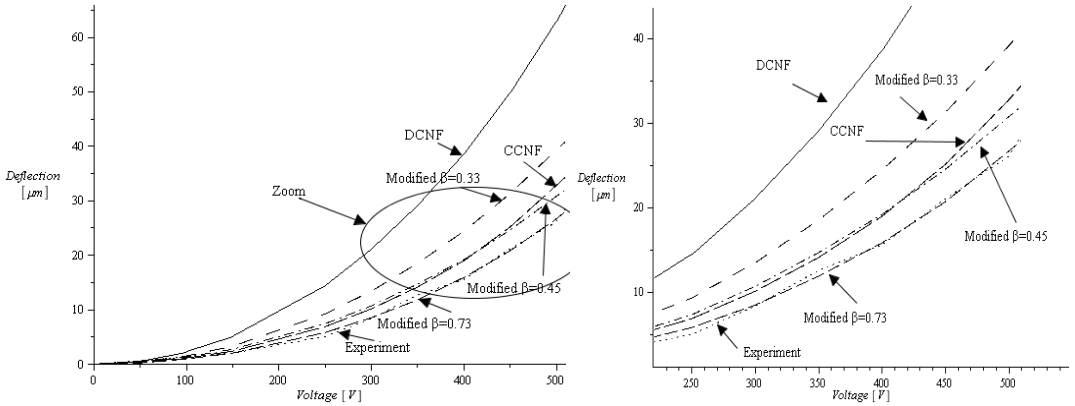

Figure 2.9.4. a) Deflection as a function of the applied potential; theoretical and experimental values of the deflection of the micro-cantilever beam II; **b)** Zoom-in of the indicated zone

The natural frequency changes with the application of the potential field. The theoretical and experimental findings are illustrated in figures 2.9.5 and 2.9.6. The four different models were considered. As one can see from the two figures, the best fit with experimental is not anymore a modified model but the CCNF model. Modified stiffness

selected within its range gives results with small divergence but, however, far from experiments. Both cases yield values of the resonant frequency below the experimental values. Both figures show that, linear approach for the stiffness is much below the experimental values, even less than modified models. In both vibration experiments, maximum applied voltage was 225 [V]. The error for modified stiffness and linear k ranges from about 35% and goes up to 200% with respect to the experimental recorded values.

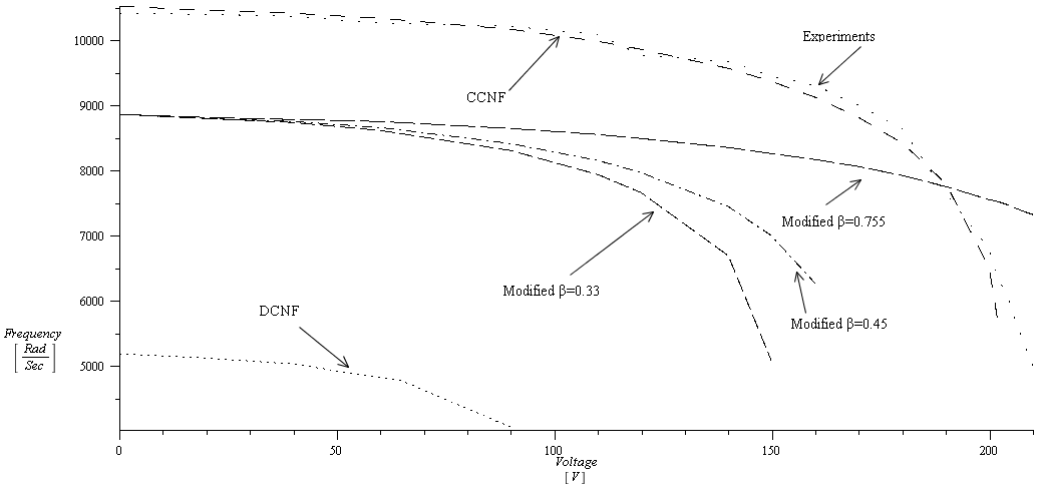

Figure 2.9.5. The frequency dependence on the applied voltage for beam I in comparison with the considered models

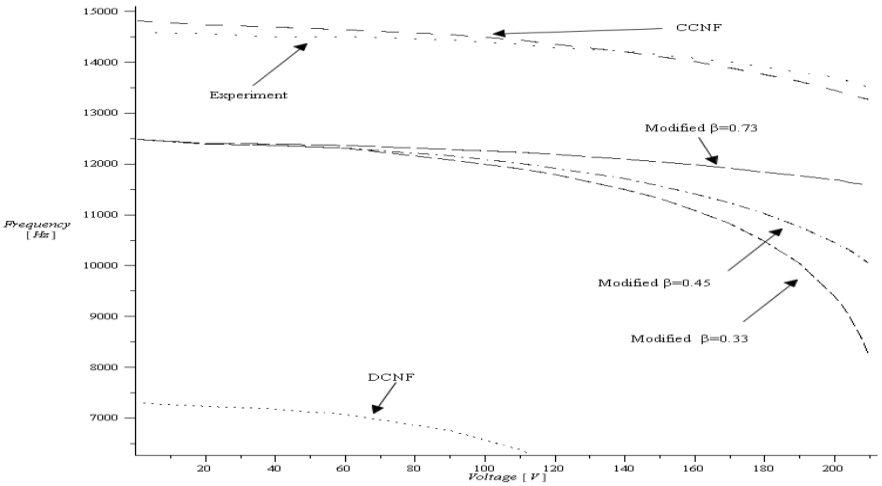

Figure 2.9.6. The frequency dependence on the applied voltage for beam II in comparison with the considered models

The experimental results show that, although modified model can well fit the static deflection due to potential difference in microstructures, the appropriate model would not fit the dynamic response of the structure subjected to electrostatic field. The proposed CCNF can be a good matching model for dynamical model which gives significantly large errors in the static deflection model.

2.10. Conclusion and discussion

The analytical formulations in micro-systems have followed the formulations already available in the human-sized world. The simple explanation to this choice is that no other theories to be applied to micro-sized systems are available. The quantum physics targets a much smaller size. Most of the commonly used models of structures have been linearized for obvious reasons. The linearization would not be suitable with the micro-sized systems and here is the motivation to re-consider the fundamental models not neglecting non-linearities. The non-linear systems are represented either by non-linear ODE or PDE. Both type of equations rise significant challenges when required to be solved somehow by non-numerical methods. The sense of sensitivity of a certain parameter requires significant effort to be perceived. Usually, extensive parametric studies are required to gain such knowledge. Otherwise, one could revisit mathematical methods to try solving the non-linear phenomenon-describing equations given the fact that an exact solution, if available, provides a wide perspective on the analysis of the behavior of the solution function. Under many circumstances, the popular routines for the well-known numerical methods which are embedded in multi-purpose software package such as Matlab, Maple,

Mathematica, MathCAD or, Macsyma would yield no solution to stiff ODE. This is the case of the equation that describes the dynamic behavior of a micro-system subjected to an electrostatic field.

The present work uses Lie group symmetry to reduce the order of the second order ordinary differential equation to a first order differential equation. Unfortunately, the reduced first order ODE has no translation, rotation or scaling symmetry and the solution of the equation cannot be formulated in a close-form. If another type of symmetry is found, the differential equation could be analytically solved. However, certain interesting results are revealed by the reduced first order differential equation. The equation exhibit the non-linearity through two terms. If the third order term is assumed zero, one finds out the solution of the linearized solution for the second order ODE that models a dynamic micro-systems subjected to an electrostatic filed. Further, *Isode* numerical algorithm used for stiff differential equations was used to solve the ODE that describes the dynamics of a micro-system subjected to electrostatic forces. The time response of the system shows that a micro-system such as a micro-cantilever beam will respond to a voltage close to the pull-in value applied as a step input through a ramp that will hold in a marginal equilibrium position that occurs at a deflection that represents 4/9 of the initial gap. The system leaves the saddle point to settle in a position that corresponds to a deflection of 2/9 of the initial gap. Various models built based on the open literature show significant differences. The deflection and the resonant frequency of two micro-cantilever beams are experimentally measured and compared to the numerical methods for static and dynamic models. Different models fit different experimental data.

The findings on this work bring more understanding on the phenomena at micro-size level.

2.11. Summary

This chapter presents an analytical model developed based on Lie Group symmetry that enables reduction of the non-linear ODE that is used to model the dynamic behavior of a micro-cantilever beam. The resulting equation is a first order ODE that could be easier solved. The solution based on numerical formulation for the second order ODE versus the first order show that the proposed method is robust. A detailed parametric study on the dynamic behavior of a micro-cantilever beam subjected to an electrostatic filed is further carried out. The results are finally validated through experimental work. The conclusion of the work is that non-linear models produce more accurate results that are closer to the real world than the linear models. The error yield through linearization is under certain conditions significant.

Chapter 3

The Analysis of the Non-linear Deflection of Straight and Non-straight Beams Using Lie Symmetry Groups

Rationale

The large deflection of beams cannot be described by the linear formulation used for beams experiencing linear deflection. Further, the linear models could in part accommodate large deflections at the cost of significant errors such as those encountered in some applications where bending exceeds three times the thickness of the beam. However, the deflection of cantilever type beams subjected to arbitrary loads that yield non-linear deflection has been solved so far only for two loading conditions, namely, point force and moment. The proposed solutions involve the solving of first and second kind elliptic integrals. The present work presented a general method based on Lie symmetry groups that yields an exact solution to the general problem involving any arbitrary loading. A general solution for the large deflection of a beam arbitrarily supported is provided. The formulation is further fully validated against the two available solutions available in the literature for the cantilever beams subjected to point moment and force. This chapter presents the solution to the non-linear deflection of non-straight cantilever deflection of cantilever beams subjected to concentrated loads, forces and

moment applied all at the free end. The deflections of straight cantilever beams subjected to loads that create deflections in the linear domain have been studied for a long time and the formulations are content of standard textbooks. However, the large deflection of straight cantilever beams problem was solved only seven decades ago and this only for particular type of loads. A generalized solution for the deflection of a non-straight beam subjected to both concentrated force and concentrated moment is presented below. Lie symmetry method is used to reduce the order of the ODE describing the large deflection of the beam. The solution is validated against the particular cases of loading for which the large deflection problem has been solved and presented in the open literature. These cases presented as validation examples are: straight cantilever beam subjected to concentrated free-end normal force, straight cantilever beam subjected to concentrated moment at the free end and straight cantilever beam subjected to both normal and axial forces applied at the free end.

3.1. Introduction

Nonlinear deflection of beams under the various forces and boundary conditions has been widely studied. The prediction of deflection of beams has been of great interest to generations of researchers. This seems to be a mundane problem as it is subject of textbooks on elementary mechanics of materials. Although both analytical and numerical solution have been found for specific type of loads, the general problem for beams that are not geometrically perfectly straight has not been approached so far of a systematic fashion. Despite the interest in the subject, so far there is no general solution to describe

the general case of loading. This chapter presents an approach in solving the general problem based on Lie symmetry groups and a general analytical solution of the problem is presented below. The objective of the present work is to investigate a versatile mathematical method into the deflection of geometrically non-straight cantilever beams subjected point loads and moments applied at the free end while experiencing non-linear deflection. Lie symmetry method presented below can be used to any geometry of the bended beams under to condition that there is no residual stress in the unloaded beam.

Nonlinear deflection of beams subjected to various types of forces and boundary conditions have been extensively studied. The differential equation of large deflection of cantilever beam under a point force at the tip was solved in 1945 [8]. In that approach the differential equation of the slope of the beam versus the length of the deflected curve was formulated and solved based on complete second and first kind elliptic integrals. The differential equation of slope versus length of the deflected curve based on consideration of shear force was numerically solved [128]. The authors used finite difference methods to solve ordinary differential equation (ODE) for distributed force on cantilever and simple supported beams. They also used the same method to solve the ODE of the simple supported beam under a point force. A numerical solution for the tapered cantilever beam under a point force at tip was presented in 1968 [129]. The author converted ODE to non-dimensional ODE and used a computer to solve it. A cantilever beam, made from materials exhibiting nonlinear properties subjected to a point force was also studied [130].

The deflection equation was calculated based on Ludwick experimental strain-stress curve. The integral equation was solved numerically and the end beam deflection and

rotation were calculated. The same problem of large deflection cantilever beams made from materials behaving of non-linear fashion under the tip point force was solved by finite difference methods [10].

The authors solved the nonlinear ODE of curvature for a cantilever made from nonlinear characteristics a material and subjected to point force at the tip by numerical methods. Power series and neural network were used to solve large deflection of a cantilever beam under tip force [9]. Nonlinear ODE were decomposed to a system of ODEs and solved by neural networks. Large deflections of cantilever beams made from nonlinear elastic materials under uniform distributed forces and a point force at tip were also studied [131]. In this work a system of nonlinear ODEs was developed to model the system which was further solved by Runge-Kutta method. Researchers [1] in [1]used almost a similar method that was used in [8] to solve the large deflection of a cantilever under the point force at the tip and they validated their results with experiments. Also they used non-dimensional formulation to simplify the nonlinear deflection to linear analysis. They showed that nonlinear small deflection is same as those found through the linear analysis. Two dimensional loading of cantilever beams with point forces loads at the free end was studied for non-prismatic and prismatic beams [132]. Authors formulated the model for the general loading conditions in beams. The result is a nonlinear PDE which is presented in this paper. Further, the authors numerically solved the non-dimensional equation using a polynomial to define the rotating angle of the beam. They presented some examples applied to their methods. A cantilever beam subjected to a tip moment with nonlinear bimorph material was theoretically and numerically studied [34]. The authors used an exact solution for the deflection of a cantilever with a moment applied at the tip.

Cantilever beam under uniform and tip point force was numerically and experimentally studied [12]. In this study, the authors used a system of ODEs to solve numerically this problem. Finite difference methods for analysis of large deflection of a non-prismatic cantilever beam subjected to different types of continuous and discontinuous loadings was studied [13]. Authors formulated the problem based on [132] and further used quasi-linearization central finite differences method to solve the problem. An explicit solution for large deflection of cantilever beams subjected to point force at the tip was obtained by using the homotopy analysis method (HAM) presented in [133]. Large deflection of a non-uniform spring-hinged cantilever beam under a follower point force at the tip was formulated and solved numerically [134].

3.2. Nonlinear deflection of beams

Deflection of a cantilever can be defined as y in the below nonlinear ODE:

$$\frac{\frac{d^2y}{dx^2}}{(1+(\frac{dy}{dx})^2)^{\frac{3}{2}}} = \frac{M(x)}{E(x)I(x)} \tag{3.1}$$

where:

E is Young modulus of elasticity of the material of the beam

I is bending cross-section moment of inertia

y is the current deflection

x is the current coordinate along the beam

$\omega(x), P(x), M$ are distributed, point forces and moment

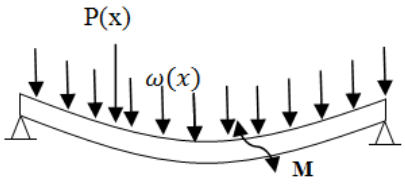

Figure 3.1.1. Deflection of a beam subject to a distributed load and a concentrated moment

As an example $M(x)$ at any point for a point force at the tip of the beam (Fig. 3.1.1) is:

$$M(x) = F(l - \delta_x - x) \tag{3.2}$$

δ_x horizantal deflection

3.3. Lie symmetry analysis of large deflection of beams

One can show that according to (E.6) and (E.7) infinitesimal transformation is defined as[122]:

$$Xf = \xi(x,y)\frac{\partial}{\partial x} + \eta(x,y)\frac{\partial}{\partial y} \tag{3.3}$$

where:

$$\xi(x,y) = \left.\frac{\partial \phi}{\partial \alpha}\right|_{\alpha=0} \quad , \quad \eta(x,y) = \left.\frac{\partial \psi}{\partial \alpha}\right|_{\alpha=0} \tag{3.4}$$

and X is an operator

ϕ,ψ are continues transformation functions

It can be shown [115] that for a second order differential equation like:

$$\frac{d^2y}{dx^2} = \omega(x, y, \frac{dy}{dx}) \tag{3.5}$$

by applying an infinitesimal group on (E.7), ξ and η in (3.1) the transformation must satisfy the equation below[121]:

$$\begin{aligned} &\eta_{xx} + (2\eta_{xy} - \xi_{xx})y' + (\eta_{yy} - 2\xi_{xy})y'^2 - \xi_{yy}y'^3 + \\ &(\eta_y - 2\xi_x - 3\xi_y y')\omega = \xi\omega_x + \eta\omega_y + \\ &(\eta_x + (\eta_y - \xi_x)y' - \xi_y y'^2)\omega_{y'} \end{aligned} \tag{3.6}$$

By decomposing (3.4) into a system of PDEs, ξ and η can be calculated. Also from (3.2) the transformation φ and ψ can be calculated. If one considers the infinitesimal transformation in the form of below which is tarnslation and scaling:

$$\begin{aligned} \xi &= C_1 + C_2 x + C_3 y \\ \eta &= C_4 + C_5 x + C_6 y \end{aligned} \tag{3.7}$$

where:

$C_1, C_2, C_3, C_4, C_5, C_6$ are constant numbers.

Most of Lie symmetries including rotation, translation and scaling could be found with the above transformations.For equation (3.5) , ω is given by:

$$\frac{d^2y}{dx^2} = \omega(x, y, y') = \frac{M(x)}{E(x)I(x)}(1 + (\frac{dy}{dx})^2)^{\frac{3}{2}} \tag{3.8}$$

Substitution of (3.7) and (3.8) in (3.6) gives:

$$\begin{aligned}
&-\frac{M(x)}{E(x)I(x)}C_6 + \frac{2M(x)}{E(x)I(x)}(\frac{dy}{dx})^2 C_6 + \frac{2M(x)}{E(x)I(x)}C_2 \\
&-\frac{M(x)}{E(x)I(x)}(\frac{dy}{dx})^2 C_2 + 3\frac{M(x)}{E(x)I(x)}\frac{dy}{dx}C_3 + \\
&\frac{d}{dx}(\frac{M(x)}{E(x)I(x)})C_1 + \frac{d}{dx}(\frac{M(x)}{E(x)I(x)})C_1(\frac{dy}{dx})^2 + \frac{d}{dx}(\frac{M(x)}{E(x)I(x)})C_2 x + \\
&\frac{d}{dx}(\frac{M(x)}{E(x)I(x)})C_2 x(\frac{dy}{dx})^2 + \frac{d}{dx}(\frac{M(x)}{E(x)I(x)})C_3 y + \\
&\frac{d}{dx}(\frac{M(x)}{E(x)I(x)})C_3 y(\frac{dy}{dx})^2 + 3(\frac{M(x)}{E(x)I(x)})C_5\frac{dy}{dx} = 0
\end{aligned} \tag{3.9}$$

This can be further written as:

$$
\begin{aligned}
&(-\frac{M(x)}{E(x)I(x)}C_6 + 2\frac{M(x)}{E(x)I(x)}C_2 + \frac{d}{dx}(\frac{M(x)}{E(x)I(x)})C_1 \\
&+ \frac{d}{dx}(\frac{M(x)}{E(x)I(x)})C_2 x) + (2\frac{M(x)}{E(x)I(x)}C_6 - \frac{M(x)}{E(x)I(x)}C_2 \\
&+ \frac{d}{dx}(\frac{M(x)}{E(x)I(x)})C_1 + \frac{d}{dx}(\frac{M(x)}{E(x)I(x)})C_2 x + \frac{d}{dx}(\frac{M(x)}{E(x)I(x)})C_3 y) \\
&(\frac{dy}{dx})^2 + (3\frac{M(x)}{E(x)I(x)}C_3 + 3\frac{M(x)}{E(x)I(x)}C_5)\frac{dy}{dx} = 0
\end{aligned}
\tag{3.10}
$$

As all three parentheses must be zero, in first parenthesis coefficients of x and

$\frac{d}{dx}(\frac{M(x)}{E(x)I(x)})$ are zero:

$$C_1 = C_2 = 0 \tag{3.11}$$

and also:

$$C_6 = 0 \tag{3.12}$$

In the second parenthesis coefficient of y must be zero so:

$$C_3 = 0 \tag{3.13}$$

In the last parenthesis, in order to yield a zero coefficient $C_5 = 0$ must be also zero.

Therefore only $C_4 \neq 0$, and one can write:

$$\eta = C_4 = 1 \tag{3.14}$$

Therefore (3.3) becomes:

$$Xf = \frac{\partial f}{\partial y} \tag{3.15}$$

Canonical coordinates (E.12) and (E.13) can be calculated as[122]:

$$s(r,x) = \left(\int \frac{dx}{\xi(x, y(r,x))}\right)\Big|_{r=r(x,y)} \tag{3.16}$$

where:

$r(x,y)$ is the solution of:

$$Xf = \frac{\eta(x,y)}{\xi(x,y)} \tag{3.17}$$

One can show that:

$$r(x,y) = x$$

$$s(x,y) = y \tag{3.18}$$

Any canonical coordinates must satisfy the following conditions[114]:

$$\xi(x,y)r_x + \eta(x,y)r_y = 0$$

$$\xi(x,y)s_x + \eta(x,y)s_y = 1$$

$$\begin{bmatrix} r_x & r_y \\ s_x & s_y \end{bmatrix} \neq 0 \tag{3.19}$$

It is easy to show that (3.16) satisfies (3.17). According to (E.17) and (E.18) the reduced form of (E.19) becomes:

$$v = x$$

$$u(v) = \frac{dy(x)}{dx} \tag{3.20}$$

This transformation is a well-known and it is brought here just to show the method of deriving the canonical coordinates. Substituting (3.18) in (E.19) gives:

$$\frac{du(v)}{dv} = \frac{M(v)}{EI}(1+u^2(v))^{\frac{3}{2}} \tag{3.21}$$

This is a first order ODE and it is possible to further solve it by Lie symmetry method.

It can be shown that [114] for a first order differential equation like:

$$\frac{dy}{dx} = \omega(x,y) \tag{3.22}$$

where:

$$\frac{du(v)}{dv} = \omega(u,v) = \frac{M(v)}{EI}(1+u^2(v))^{\frac{3}{2}} \tag{3.23}$$

if one is applying an infinitesimal group on (E.7), ξ and η in (3.21) which must satisfy the equation below:

$$\eta_x + (\eta_y - \xi_x)\omega - \xi_y\omega^2 = \xi\omega_x + \eta\omega_y \tag{3.24}$$

And further substituting (3.23) in (3.24) yields:

$$\begin{aligned} &\eta_v + (\eta_u - \xi_v)\frac{M(v)}{EI}(1+u(v)^2)^{\frac{3}{2}} - \\ &\xi_u \frac{M^2(v)}{(EI)^2}(1+u(v)^2)^{\frac{3}{2}} = \\ &\xi \frac{dM(v)}{dvEI}(1+u(v)^2)^{\frac{3}{2}} + \\ &\eta \frac{3M(v)}{EI}u(v)(1+u(v)^2)^{\frac{1}{2}} \end{aligned} \tag{3.25}$$

There is no term of $u(v)(1+u(v)^2)^{\frac{1}{2}}$ the left hand side of the equation, so the equation yields:

$$\eta = 0 \tag{3.26}$$

Therefore (3.25) can be written as:

$$-\frac{M(v)}{E(v)I(v)}(\xi_v(1+u(v)^2)^{\frac{3}{2}}+\xi_u\frac{M(v)}{E(v)I(v)}(1+u(v)^2)^3)=$$
$$\xi\frac{d}{dv}(\frac{M(v)}{E(v)I(v)})(1+u(v)^2)^{\frac{3}{2}} \tag{3.27}$$

Comparing the moment in both sides of equation one can show that $\xi_u = 0$, so:

$$\xi = \xi(v) \tag{3.28}$$

By considering (3.28), equation (3.27) will simplify to:

$$-\frac{E(v)I(v)}{M(v)}\frac{d}{dv}(\frac{M(v)}{E(v)I(v)})=\frac{d\xi(v)}{\xi(v)dv} \tag{3.29}$$

which has as solution:

$$\xi(v)=\frac{E(v)I(v)}{M(v)}C \tag{3.30}$$

where C is a constant that can be considered to start with as the unit. Hence:

$$\xi(v)=\frac{E(v)I(v)}{M(v)} \tag{3.31}$$

Therefore:

$$Xf = \frac{E(v)I(v)}{M(v)}\frac{\partial f}{\partial x} \tag{3.32}$$

Canonical coordinates can be calculated as:

$$r(u,v) = u(v)$$

$$s(u,v) = \int \frac{M(v)}{E(v)I(v)}dv \tag{3.33}$$

These canonical coordinates satisfy the conditions (3.19). Equation (E19) can be written as:

$$\frac{ds}{dr} = \frac{1}{(1+r^2)^{\frac{3}{2}}} \tag{3.34}$$

for which the solution is:

$$s(r) = \frac{r}{(1+r^2)^{\frac{1}{2}}} + C_1 \tag{3.35}$$

or:

$$r = \frac{s(r)+C_1}{\sqrt{1-(s(r)+C_1)^2}} \tag{3.36}$$

Substituting (3.33) in (3.36) yields:

$$r = \frac{\int \frac{M(v)}{E(v)I(v)} dv + C_1}{\sqrt{1 - (\int \frac{M(v)}{E(v)I(v)} dv + C_1)^2}} \tag{3.37}$$

Further, substituting (3.20) in (3.37) results in:

$$\frac{dy}{dx} = \frac{\int \frac{M(x)}{E(x)I(x)} dx + C_1}{\sqrt{1 - (\int \frac{M(x)}{E(x)I(x)} dx + C_1)^2}} \tag{3.38}$$

Therefore, *y* becomes:

$$y = \int \frac{\int \frac{M(x)}{E(x)I(x)} dx + C_1}{\sqrt{1 - (\int \frac{M(x)}{E(x)I(x)} dx + C_1)^2}} dx + C_2 \tag{3.39}$$

This solution is expressed in terms of two constants C_1 and C_2 that could be evaluated from the boundary conditions. A 3D graph for C_1 and C_2 both equal to zero is illustrated below. The graph shows the deflection of each point on the beam with respect to the curvature $\frac{M(x)}{E(x)I(x)}$ and its integral. The integral in closed curves has a property which comes from Gauss-Bonnet Theorem in 3D space. This property states that the integral of the Gaussian curvature over a closed smooth surface is equal to 2π times the Euler

characteristic of the surface. The Euler characteristic is a topological invariant, a number that describes a topological space's shape or structure regardless of the way it bents.

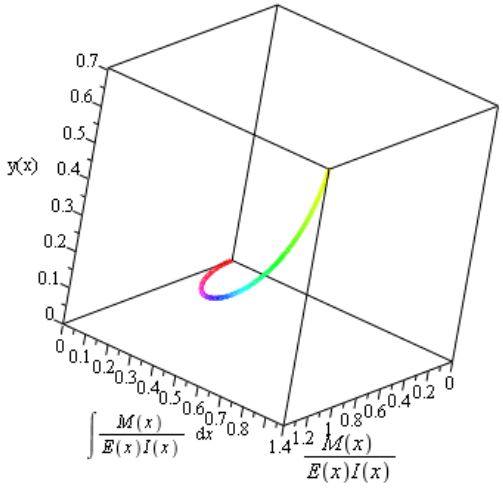

Figure 3.3.1. A general solution of equation (3.39)

As illustrated in figure 3.3.1 and from from equation (3.39) the large deflection of the beam has integral form. The deflection is function of the bending moment, Young modulus and the geometric moment of inertia in each seaction. Neglecting the denominator will provide small deflection equation for a beam (linear solution).

3.4. Example

Below the two closed forms solution of the deflection in the open literature will be compared with the solution obtained by the proposed method.

Case study 1- Large deflection of a cantilever beam subjected to a tip force

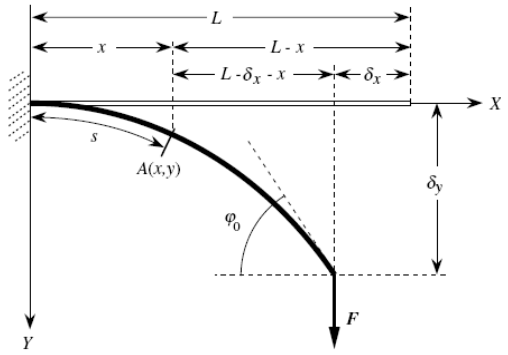

Figure 3.4.1. Cantilever beam loaded with an external vertical concentrated load at the free end and definitions of the parameters for large deflections[1].

If a point force is applied at the tip of a cantilever beam the bending moment can be expressed as (3.2). Moment of can be written as:

$$M(x) = P(L - \delta_x - x) \tag{3.40}$$

Hence,

$$\int \frac{M(x)}{E(x)I(x)}dx = \frac{P}{EI}(Lx - \delta_x - \frac{x^2}{2}) \tag{3.41}$$

By considering the boundary conditions in the equation (3.38), $C_1 = 0$.

From (3.39) one can calculate y(x) as:

$$\int \frac{M(x)}{E(x)I(x)}dx = \int \frac{\frac{P}{EI}(Lx - \delta_x - \frac{x^2}{2})}{\sqrt{1-(\frac{P}{EI}(Lx - \delta_x - \frac{x^2}{2}))^2}}dx + C_2 \tag{3.42}$$

By assuming:

$$\gamma = L - \delta_x$$

$$u = \frac{p\gamma + \sqrt{p^2\gamma^2 + 2EIp}}{p}$$

$$v = \frac{p\gamma + \sqrt{p^2\gamma^2 - 2EIp}}{p}$$

$$w = \frac{p\gamma - \sqrt{p^2\gamma^2 - 2EIp}}{p} \tag{3.43}$$

$$z = \frac{p\gamma - \sqrt{p^2\gamma^2 + 2EIp}}{p}$$

$$q = \sqrt{\frac{(w-u)(v-z)}{(v-u)(w-z)}}$$

Equation (3.42) can be simplified to:

$$
\begin{aligned}
y(x) = {} & \frac{1}{\sqrt{(x-v)(x-w)(x-u)(x-z)}}\left((x-v)(x-u)(x-z)+(v-z)\sqrt{\frac{(z-w)(x-v)}{(z-v)(x-w)}}(x-w)^2\right. \\
& \left.\sqrt{\frac{(w-v)(x-u)}{(u-v)(x-w)}}\sqrt{\frac{(w-v)(x-z)}{(z-v)(x-w)}}\left(\frac{v(w-z)+w(z+w)}{(z-w)(w-v)}\right)\right) \\
& EllipticF\quad\left(\sqrt{\frac{(z-w)(x-v)}{(z-v)(x-w)}},\sqrt{\frac{(w-u)(v-z)}{(v-u)(z-w)}}\right)+ \\
& \frac{(v-u)}{(w-v)}EllipticE\quad\left(\sqrt{\frac{(w-z)(x-v)}{(z-v)(x-w)}},\sqrt{\frac{(w-u)(v-z)}{(v-u)(z+w)}}\right)- \\
& \frac{4\gamma}{z-w}EllipticPi\quad\left(\sqrt{\frac{(z-w)(x-v)}{(z-v)(x-w)}},\frac{v-z}{z-w},\sqrt{\frac{(w-u)(v-z)}{(v-u)(w-z)}}\right) \\
& +\frac{1}{(w-z)(z-u)\sqrt{(x-v)(x-w)(x-u)(x-z)}} \\
& (4\gamma(u-w)\sqrt{\frac{(z-w)(x-u)}{(w-u)(x-z)}}(x-z)^2\sqrt{\frac{(z-u)(x-v)}{(v-u)(x-z)}}\sqrt{\frac{(z-u)(x-w)}{(w-u)(x-z)}} \\
& (z\,EllipticF\quad\left(\sqrt{\frac{(z-w)(x-u)}{(w-u)(x-z)}},\sqrt{\frac{(z-v)(u-w)}{(u-v)(w-z)}}\right) \\
& (u-z)EllipticPi\quad\left(\sqrt{\frac{(z-w)(x-u)}{(w-u)(x-z)}}\frac{(w-u)}{(w-z)},\sqrt{\frac{(z-v)(u-w)}{(u-v)(w-z)}}\right)
\end{aligned}
\tag{3.44}
$$

This equation explicitly relates length and force to deflection. To calculate deflection, equation (3.44) must be solved simultaneously with:

$$
L = \int_0^{L-\delta_h}\sqrt{(1+(\frac{dy}{dx})^2}\,dx \tag{3.43}
$$

Numerical solution of these equations are given in the table 3.4.1 which is complete agreement with .

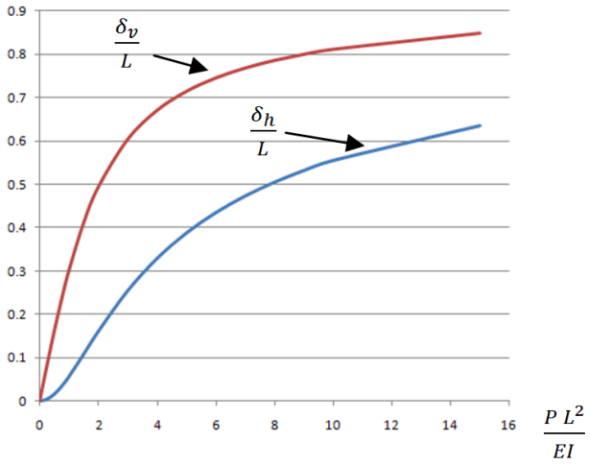

Figure 3.3.2. Large deflection of cantilever under point force at the tip in vertical and horizontal directions

Table 3.3.1. Numerical non-dimensional solution of cantilever under point force at the tip

$\frac{PL^2}{EI}$	$\frac{\delta_h}{L}$	$\frac{\delta_v}{L}$
0	0	0
0.2	0.0026466134	0.0663645377
0.4	0.0103539307	0.1309752510
0.6	0.0224876954	0.1923502946
0.8	0.0381656225	0.2494515460
1	0.0564330035	0.3017207122
1.5	0.1079415014	0.4109782132
2	0.1606417216	0.4934574795
3	0.2544201850	0.6032534411
4	0.3289412419	0.6699641822
5	0.3876283604	0.7137915239
6	0.4345888287	0.7445711491
7	0.4729274194	0.7673691097
8	0.5048277350	0.7849823718
9	0.5318205639	0.7990555255
10	0.5549956005	0.8106090210
15	0.6352857811	0.8477156727
∞	1	1

Case study 2-Larege deflection of a cantilever beam subjected to a tip moment

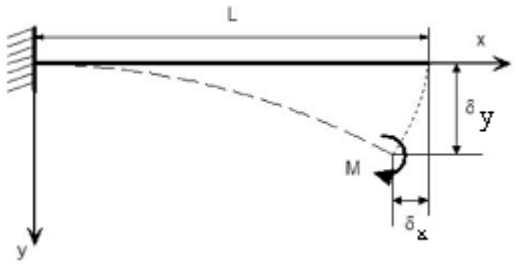

Figure 3.3.3. Cantilever beam subjected to an end moment .

If a point moment is applied at the tip of cantilever beam as figure 3.4.3, equation (3.1) becomes:

$$\frac{\frac{d^2y}{dx^2}}{(1+(\frac{dy}{dx})^2)^{\frac{3}{2}}}=\frac{M}{EI} \tag{3.44}$$

According to [34] deflection is:

$$y(x)=\frac{EI}{M}(1-\sqrt{1-(\frac{Mx}{EI})^2}) \tag{3.45}$$

By considering the boundary condition as the deflection at the fixed point:

$$y(0)=\left.\frac{dy}{dx}\right|_{x=0}=0 \tag{3.46}$$

which satisfies equation (3.45). The equation (3.38) in which the boundary conditions are considered becomes:

$$\left.\frac{dy}{dx}\right|_{x=0} = \left.\frac{Mx + C_1}{\sqrt{-(Mx)^2 - 2C_1Mx - C_1^2 + (EI)^2}}\right|_{x=0} = 0 \tag{3.47}$$

hence:

$$C_1 = 0 \tag{3.48}$$

Equation (3.39) becomes:

$$y(x) = \int \frac{Mx}{\sqrt{-(Mx)^2 + (EI)^2}}\,dx + C_2 = -\frac{(EI - Mx)(EI + Mx)}{M\sqrt{-M^2x^2 + (EI)^2}} + C_2 \tag{3.49}$$

By considering the boubdary conditions, C_2 in equation (3.49) becomes:

$$C_2 = \frac{EI}{M} \tag{3.50}$$

Finally equation (3.49) becomes:

$$y(x) = -\frac{(EI - Mx)(EI + Mx)}{M\sqrt{(EI)^2 - (Mx)^2}} + \frac{EI}{M} = \frac{EI}{M}(1 - \sqrt{1 - (\frac{Mx}{EI})^2}) \tag{3.51}$$

and as one can see, it is identical to (3.45). Deflection of cantilever various to the respect of length and $\frac{M}{EI}$ is given in the below 3D graph. This graph shows the variation of deflection of cantilever versus it's curvature in defferent points. It shows that nonlinearity incearse by curvature faster than length of cantilever.

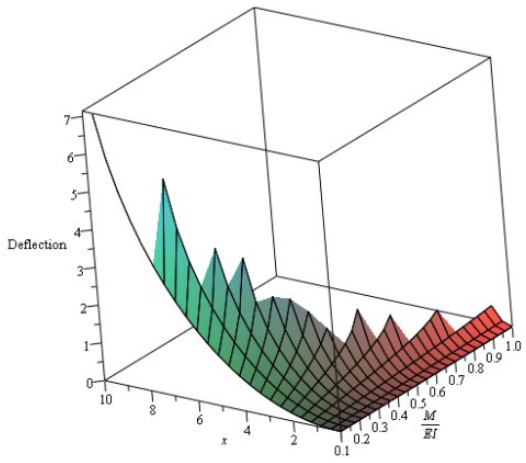

Figure 3.3.4. Large deflection of cantilever beam under moment at the tip.

Case study 3- Large deflection of a cantilever beam made of non-linear materials of Ludwick type subjected to a tip moment.

Generally the relation between stress and strain under small stress conditions is linear as stated by Hook Law. By increasing stress nonlinear behavior of material is expressed. For most of materials the non-linear behaviour can be defined asa stress-strain relation like:

$$\sigma = B\varepsilon^{\frac{1}{n}} \tag{3.51}$$

This kind of materials are called Ludwick materials. Here, B and n represent constants related to material properties. For a rectangular cross section of beam subjected to a moment at the free end, $\frac{M(x)}{E(x)I(x)}$ can be written as[130]:

$$\frac{\frac{d^2y}{dx^2}}{(1+(\frac{dy}{dx})^2)^{\frac{3}{2}}} = \frac{M^n}{K_n} \tag{3.52}$$

Where $K_n = \frac{n^n b^n h^{2n+1} B^n}{2^{n+1}(1+2n)^n}$, b is width and h is thickness. By substituting (3.52) in (3.39):

$$y(x) = \int \frac{\int \frac{M^n}{K_n} dx + C_1}{\sqrt{1-(\int \frac{M^n}{K_n} dx + C_1)^2}} dx + C_2 \tag{3.53}$$

As case 1, one can show that $C_1 = 0$ and $C_2 = \frac{K_n}{M^n}$. Equation (3.53) simplified to:

$$y(x) = (\frac{K_n}{M^n})(1 - \sqrt{1-(\frac{K_n}{M^n})^2 x^2} \tag{3.54}$$

This equation was provided in [130]. When there is no moment *y(x)* limit is zero for any case of *n*. This result was evaluated by a freeware software developed in MIT called wxMaxima0.8.2. This a free mathematical software which is developed by Maxima which is a spin-off from the MIT.

The deflection of cantilever to the respect to moment and length for a cantilever beam with $b = 0.25\ [in], h = 1.0\ [in],\ n = \frac{1}{0.209}$ and $B = 66100\,[\text{Psi}]$ is presented in graph below.

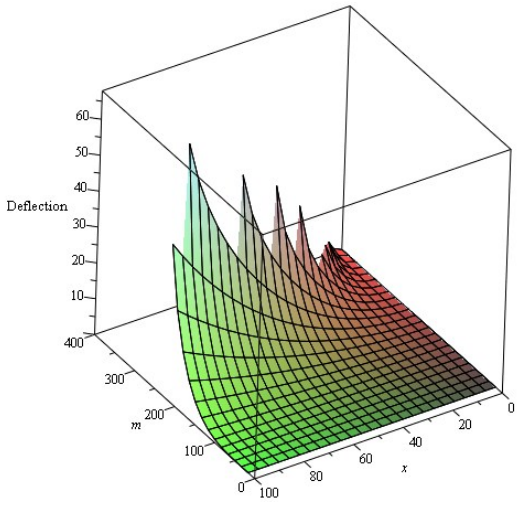

Figure 3.3.5. Large deflection of cantilever beam from nonlinear material, under moment at the tip.

Case study 4-Larege deflection of a cantilever beam of non-linear materials of Ludwick type subjected to a tip force

Like case 3 ODE is (3.52) whereas:

$$K_n = \frac{n^n b^n h^{2n+1} B^n}{2^{n+1}(1+2n)^n P^n} \tag{3.55}$$

and

$$M = P(L - x - \delta_x) \tag{3.56}$$

where:

P is point force and δ_x is end deflection.

Based on above equations, one can write:

$$\int \frac{M(x)}{E(x)I(x)}dx = \int \frac{M^n}{K_n}dx = -\frac{(L-x-\delta_x)^{n+1}}{(n+1)K_n} \tag{3.57}$$

For a cantilever beam B.C. is:

$$\left.\frac{dy}{dx}\right|_{x=0} = 0 \tag{3.58}$$

From (3.38) C_1 will be:

$$C_1 = \frac{1}{K_n}\frac{(L-\delta_x)^{n+1}}{(n+1)K_n} \tag{3.59}$$

By considering (3.57) and (3.59), one can write (3.39) as:

$$y(x) = \int \frac{(L-\delta_x)^{n+1} - (L-x-\delta_x)^{n+1}dx}{\sqrt{K_n^2(n+1)^2 - [(L-\delta_x)^{n+1} - (L-x-\delta_x)^{n+1}]^2}} \tag{3.60}$$

This equations was introduced in [131]. To calculate δ_h and $y(x)$, one has to use equations (3.60) and (3.43). Numerical solution of this system of two equation and two unknowns

is sought with Maple 11.0, for a cantilever like case 3 and P=10 [lb] which results yield the below graphs:

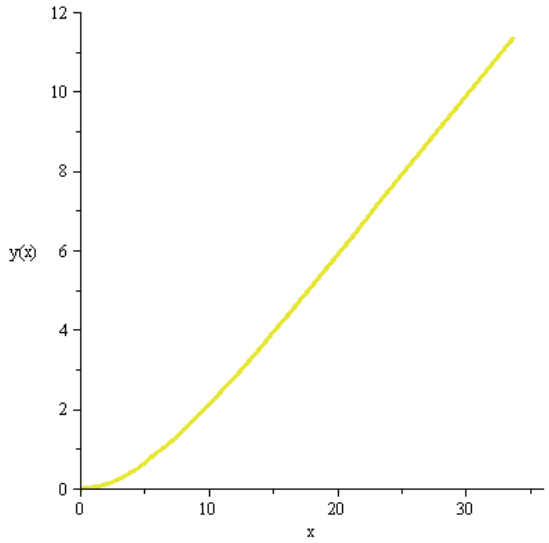

Figure 3.3.6. Large deflection of cantilever beam with non- linear material, under point force at the tip.

The shown figure t is for a cantilever beam with non-linear material which follows Ludwick law, Cantileveris subjected to point force at the free end-tip deflection for this case is:

$$\delta_y = 11.4570\ [in],$$
$$\delta_x = 2.02644\ [\text{in}]$$

In general case solution of this system of equations geven below diagram. This graph shows vertical and horizantal deflection versus applied moment. It shows that horzintal deflection increase with moment slitly compare to vertical deflection, where as in linear material with pint force, figure 3.4.2, horizantal deflection increase rapidly .

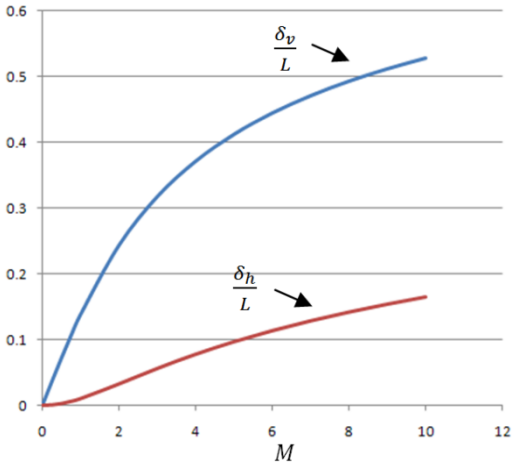

Figure 3.3.7. Large deflection of a cantilever beams of non-linear materials of Ludwick type subjected to a tip force

The deflection in horizontal direction maintains within a trend that could be accepted as linear while in vertical direction, it does not.

3.5. Small deflection

In general application of engineering, the assumption of small deflection beams is used. To relate small deflection and large deflection, one can consider (3.39) while assumes that curvature $\frac{M(x)dx+C_1}{E(x)I(x)}$ is very small, so in the denominator $(\int M(x)dx+C_1)^2 << (E(x)I(x))^2$, the equation will simplified to:

$$y(x)=\int\frac{\int M(x)dx+C_1}{E(x)I(x)}dx+C_2=\frac{1}{EI}\int(\int M(x)dx+C_1)dx+C_2 \tag{3.51}$$

where E and I are considered constant.

This is the well-known small deflection of the beam. One can assume above assumption because in small deflection $\int M(x)dx + C_1$ is slope of curvature which is very small compare to EI.

3.6. Calculation of bending moment and stress based on known deflection

If the large deflection of a beam can be described by a polynomial like:

$$y(x) = \sum_{n=0}^{k} a_n x^n \tag{3.52}$$

where k can be infinite and $y(x)$ satisfies boundary conditions. By substituting (3.52) in (3.39) and calculating $\int \frac{M(x)}{E(x)I(x)}$, it yields:

$$\int \frac{M(x)}{E(x)I(x)} = \frac{\sum_{n=0}^{k} n a_n x^n}{\sqrt{(\sum_{n=0}^{k} n a_n x^n)^2 + x^2}} \tag{3.53}$$

$$M(x) = E(x)I(x)\left(\frac{\sum_{n=0}^{k} n^2 a_n x^{n-1}}{\sqrt{(\sum_{n=0}^{k} n a_n x^n)^2 + x^2}} - \frac{1}{2}\frac{(\sum_{n=0}^{k} n a_n x^n)(2\sum_{n=0}^{k} n a_n x^n)(\sum_{n=0}^{k} n^2 a_n x^{n-1}) + 2x)}{(\sqrt{(\sum_{n=0}^{k} n a_n x^n)^2 + x^2})^{\frac{3}{2}}}\right) \tag{3.54}$$

Based on elasticity theory, stress in a point at a cross section can be calculated as:

$$\sigma = \frac{M(x)y}{I(x)} \tag{3.55}$$

Substitutions of (54) in (55) give:

$$\sigma = yE(x)\ \left(\frac{\sum_{n=0}^{k} n^2 a_n x^{n-1}}{\sqrt{(\sum_{n=0}^{k} n a_n x^n)^2 + x^2}} - \frac{1}{2}\frac{(\sum_{n=0}^{k} n a_n x^n)(2\sum_{n=0}^{k} n a_n x^n)(\sum_{n=0}^{k} n^2 a_n x^{n-1}) + 2x)}{(\sqrt{(\sum_{n=0}^{k} n a_n x^n)^2 + x^2})^{\frac{3}{2}}}\right) \tag{3.56}$$

3.7. Formulation of the large deflection of not-straight beam problem

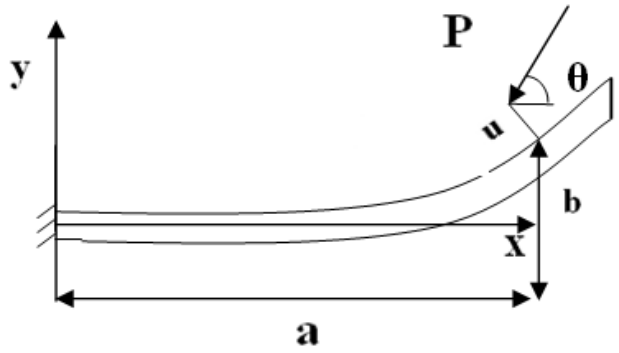

Figure 3.7.1. A non-straight cantilever under tip forces and moment

A non-straight cantilever beam as shown in figure 3.7.1 is subjected two orthogonal point forces and one moment. Internal reaction moment in any cross section on the left hand side of cantilever can be written as:

$$M(x,y) = V \times (x_0 - x) + H \times (y_0 - y) + M_0 \tag{3.57}$$

where:

$$V = P\sin(\theta_0)$$

$$H = P\cos(\theta_0)$$

$$M_0 = P.u$$

where u is distance from end of tip to neutral axis of the cantilever beam. Euler–Bernoulli moment–curvature relationship gives[11]:

$$EI\frac{d\theta}{d\rho} = M(x,y) \tag{3.58}$$

where:

$$\frac{dx}{d\rho} = \cos(\theta) \tag{3.59}$$

$$\frac{dy}{d\rho} = \sin(\theta) \tag{3.60}$$

Derivative of (3.58) yields:

$$EI\frac{d^2\theta}{d\rho^2} = -V\cos(\theta) - H\sin(\theta) \tag{3.61}$$

The boundary conditions for this ODE are:

$$\theta\big|_{\rho=0} = 0 \tag{3.62}$$

$$\left.\frac{d\theta}{d\rho}\right|_{\rho=L} = \frac{M_0}{EI} \tag{3.63}$$

L is length of cantilever.

3.8. One-parameter Lie group of transformation (pure approach)

The Lie group transformation has been intensively investigated. Bluman and Anio [121] have presented in detail algorithms that enable finding the symmetry of a specified problem. Below such as algorithm is used as presented [121]. For convenience, the definitions and the algorithm are reproduced from the above reference from chapter 3 to 7

Definition 3.1: Let $x = (x_1, x_2, ..., x_n)$ lie in region $D \subset R^n$. The set of transformations

$$x^* = X(x;\varepsilon) \tag{3.64}$$

defined for each x in D and parameter ε in set $S \subset R$, with $\phi(\varepsilon,\delta)$ defining a law of composition of parameters ε and δ in S, forms a one-parameter group of transformations on D if the following hold:

(i) For each ε in S the transformations are one-to-one onto D.

(ii) S with the law of composition ϕ forms a group G.

(iii)For each x in D, $x^* = x$ when $\varepsilon = \varepsilon_0$ corresponds to the identity e, i.e.,

$$X(x;\varepsilon) = x \tag{3.65}$$

(iv)If $x^* = X(x;\varepsilon)$, $x^{**} = X(x^*;\varepsilon)$, then

(v) $x^{**} = X(x;\phi(\varepsilon,\delta))$ (3.66)

Definition 3.2: A one-parameter group of transformations defines a one-parameter Lie group of transformations if, in addition to satisfying axioms (i)-(iv) of definition 1, the following hold:

(vi)ε is a continuous parameter, i.e., S is an interval in R. without loss of generality, ε=0 corresponds to the identity element e.

(vii) X is infinitely differentiable with respect to x in D and an analytical function of ε in S.

(viii) $\phi(\varepsilon,\delta)$ is an analytical function of ε and δ, $\varepsilon \in S, \delta \in S$.

Theorem 3.1: **T**here exists a parameterization $\tau(\varepsilon)$ such that the Lie group of transformations $X^* = X(x;\varepsilon)$ is equivalent to the solution of an initial value problem for a system of first-order ODEs given by (proof on page 112 [121]) :

$$\frac{dx^*}{d\tau} = \xi(x^*) \tag{3.67}$$

With

$$x^* = x \text{ where } \tau = 0 \tag{3.68}$$

In particular,

$$\tau(\varepsilon) = \int_0^{\varepsilon} \Gamma(\varepsilon')d\varepsilon' \tag{3.69}$$

where :

$$\Gamma(\varepsilon) = \left.\frac{\partial \phi(a,b)}{\partial b}\right|_{(a,b)=(\varepsilon^{-1},\varepsilon)} \tag{3.70}$$

and

$$\Gamma(0) = 1 \tag{3.71}$$

3.9. Infinitesimal generators

Definition 3.3: The infinitesimal generator of the one-parameter Lie group of transformations $X^* = X(x;\varepsilon)$ is the operator

$$X = X(x) = \xi(x).\nabla = \sum_{i=1}^{n} \xi_i(x) \frac{\partial}{\partial x_i} \tag{3.72}$$

Theorem 3.2: The one-parameter Lie-group of transformations, $X^* = X(x;\varepsilon)$ is equivalent to

$$x^* = e^{\varepsilon X} = \sum_{k=0}^{\infty} \frac{\varepsilon^k}{k!} X^k x \tag{3.73}$$

where the operator $X = X(x)$ is defined by (3.72) and the operator $X^k = X^k(x)$ is given by $X^k = XX^{k-1}$, $k = 1,2,...$. In particular, $X^k F(x)$ is the function obtained by applying the operator X to the function $X^{k-1}F(x)$, $k = 1,2,..., X^0 F(x) \equiv F(x)$, with $X^0 F(x) \equiv F(x)$.

3.10. Invariant functions

Definition 3.4: An infinitely differentiable function $F(x)$ is an invariant function of the Lie group of transformation $X^* = X(x;\varepsilon)$ if only if, for any group transformation $X^* = X(x;\varepsilon)$,

$$F(x^*) = F(x) \tag{3.74}$$

If $F(x)$ is an invariant function of $X^* = X(x;\varepsilon)$, then $F(x)$ is called an invariant of $X^* = X(x;\varepsilon)$ and $F(x)$ is said to be invariant under $X^* = X(x;\varepsilon)$.

Theorem 3.3: $F(x)$ is invariant under a Lie group of transformation $X^* = X(x;\varepsilon)$ if and only if

$$XF(x) \equiv 0 \tag{3.75}$$

3.11. Canonical coordinates

Definition 3.5: A change of coordinates $y = Y(x) = (y_1(x), y_2(x), ..., y_n(x))$, defines a set of canonical coordinates for the one-parameter Lie group of transformations $X^* = X(x;\varepsilon)$ if, in terms of such coordinates, the group $X^* = X(x;\varepsilon)$ becomes

$$y_i^* = y_i \quad i = 1,2,...,n \tag{3.76}$$

$$y_n^* = y_n + \varepsilon \tag{3.77}$$

Theorem 3.4: For any Lie group of transformations $X^* = X(x;\varepsilon)$, there exists a set of canonical coordinates $y = (y_1(x), y_2(x),..., y_n(x))$, such that $X^* = X(x;\varepsilon)$ is equivalent to (3.76) and (3.77).

Theorem 3.5: In terms of any set of canonical coordinates $y = (y_1(x), y_2(x),..., y_n(x)),$, the infinitesimal generator of the one- parameter Lie group of transformations $X^* = X(x;\varepsilon)$ becomes

$$Y = \frac{\partial}{\partial y_n} \tag{3.78}$$

3.12. Point transformations and prolongations

Definition 3.6: A one-parameter *(ε)* Lie group of point transformations is a group of transformation of the form

$$x^* = X(x,u,\varepsilon) \tag{3.79}$$

$$u^* = U(x,u,\varepsilon) \tag{3.80}$$

Acting on the space of $n+m$ variables

$$x = (x_1, x_2, ..., x_n) \tag{3.81}$$

$$u = (u^1, u^2, ..., u^m) \tag{3.82}$$

Theorem 3.6: The one-parameter Lie group of point transformations

$$x^* = X(x, y, \varepsilon) \tag{3.83}$$

$$y^* = Y(x, y, \varepsilon) \tag{3.84}$$

Acting on (x, y) - space extends to the following one-parameter Lie group of transformations acting on (x, y, y_1)-space:

$$y_1^* = Y(x, y, y_1, \varepsilon) \tag{3.85}$$

Theorem 3.7: The second extension of the one-parameter Lie group of point transformations (3.83) and (3.84) is following one-parameter Lie group of transformations acting on (x, y, y_1, y_2)-space:

$$x^* = X(x, y, \varepsilon) \tag{3.86}$$

$$y^* = Y(x, y, \varepsilon) \tag{3.87}$$

$$y_1^* = Y_1(x, y, y_1, \varepsilon)$$

$$y_2^* = Y_2(x, y, y_1, y_2, \varepsilon) = \frac{\dfrac{\partial Y_1}{\partial x} + y_1 \dfrac{\partial Y_1}{\partial y} + y_2 \dfrac{\partial Y_1}{\partial y_1}}{\dfrac{\partial X(x, y, \varepsilon)}{\partial x} + y_1 \dfrac{\partial X(x, y, \varepsilon)}{\partial y}} \tag{3.88}$$

where $Y_1 = Y_1(x, y, y_1, \varepsilon)$ is defined by (3.85).

3.13. Extended infinitesimal transformations

Definition 3.7: the one-parameter Lie group of point transformations

$$x^* = X(x, y, \varepsilon) = x + \varepsilon \xi(x, y) + O(\varepsilon^2) \tag{3.89}$$

$$y^* = Y(x, y, \varepsilon) = y + \varepsilon \eta(x, y) + O(\varepsilon^2) \tag{3.90}$$

Acting on (x, y)-space, has infinitesimals

$$\xi(x, y), \eta(x, y) \tag{3.91}$$

With the corresponding infinitesimal generator

$$X = \xi(x, y) \frac{\partial}{\partial x} + \eta(x, y) \frac{\partial}{\partial y} \tag{3.92}$$

Theorem 3.8: The extended infinitesimals $\eta^{(k)}$ satisfy the recursion relation

$$\eta^{(k)} = D^{(k)}\eta - \sum \frac{k!}{(k-j)!\,j!} y_{k-j+1} D^j \xi \qquad k \geq 1 \tag{3.93}$$

3.14. Solution of ODEs by Lie symmetry

The solution algorithm for first order differential equation is presented in detail in [121].

3.14.1. Solution of First-order ODEs

Assume that a first order ODE

$$y' = \frac{dy}{dx} = f(x, y) \tag{3.94}$$

has a one-parameter Lie group of point transformations, called a point symmetry, with the infinitesimal generator

$$X = \xi(x, y)\frac{\partial}{\partial x} + \eta(x, y)\frac{\partial}{\partial y} \tag{3.95}$$

canonical coordinates $r(x, y), s(x, y)$ for (3.94) which are found by solving

$$Xr = 0 \tag{3.96}$$

$$Xs = 1 \tag{3.97}$$

ODE (3.94) in terms of canonical coordinates become

$$\frac{ds}{dr} = \frac{s_x + s_y f(x,y)}{r_x + r_y f(x,y)} = F(r) \tag{3.98}$$

So

$$s(x,y) = \int^{r(x,y)} F(\rho)d\rho + c \qquad C = Const \tag{3.99}$$

3.14.2. Reduction of the order of ODE

Theorem 3.9: assume a nontrivial one-parameter Lie group of transformations (3.89) and (3.90), with infinitesimal generator (3.92), is admitted by an nth-order ODE

$$y^{(n)} = f(x, y, y', ..., y^{(n-1)} \qquad n \geq 2 \tag{3.100}$$

Let $r(x,y), s(x,y)$ be corresponding canonical coordinates satisfying (3.96) and (3.97). Then the nth-order ODE (3.100) reduces to an *(n-1)th*-order ODE

$$\frac{d^{n-1}z}{dr^{n-1}} = G(r, z, \frac{dz}{dr}, ..., \frac{d^{n-2}z}{dr^{n-2}}) \tag{3.101}$$

Where:

$$\frac{ds}{dr} = z \tag{3.102}$$

The above set of definitions and theorems could be effectively used to solve a complex problem of cantilever beam, which stands as an initial conditions problem. The curvature of the beam might be due to previous plastic deflection (deformation) or due to inter laminar stress in polymorphous layered beams. The last case can be solved using the presented method assuming that the effective geometry of the beam is due to a concentrated moment load which applied the free-end of the beam.

3.15. The algorithm formulation for Lie symmetry point

The equation (3.61) can be written as

$$\frac{d^2\theta}{d\rho^2} = -\frac{V\cos(\theta) + H\sin(\theta)}{EI} \tag{3.103}$$

From (3.93) one can show that for a second order ODE $\eta^{(2)}$ is calculated as in [115] and [120] ,

$$\eta^{(2)} = D^{(2)}\eta - \sum_{j=1}^{2} \frac{2!}{(2-j)!\,j!}\theta_{2-j+1} D^{j}\xi =$$
$$\eta_{\rho\rho} + (2\eta_{\rho\theta} - \xi_{\rho\rho})\dot{\theta} + (\eta_{\theta\theta} - 2\xi_{\rho\theta})\dot{\theta}^2 - \xi_{\theta\theta}\dot{\theta}^3 + (\eta_{\theta} - 2\xi_{\rho} - 3\xi_{\theta}\dot{\theta})\ddot{\theta} = \tag{3.104}$$
$$\xi\omega_{\rho} + \eta\omega_{\theta} + (\eta_{\rho} + (\eta_{\theta} - \xi_{\rho})\dot{\theta} - \xi_{\theta}\dot{\theta}^2)\omega_{\theta}$$

Where:

$$\omega = -\frac{V\cos(\theta) + H\sin(\theta)}{EI}$$

By decomposing (3.104) into a system of PDEs, ξ and η can be calculated. Most of Lie symmetries including rotation translation and scaling could be found with the help of the below transformations:

$$\begin{aligned} \xi &= C_1 + C_2\rho + C_3\theta \\ \eta &= C_4 + C_5\rho + C_6\theta \end{aligned} \tag{3.105}$$

where:

$C_1, C_2, C_3, C_4, C_5, C_6$ are constant numbers.

Substitution (3.104) in (3.105) yields:

$$(C_6 - 2C_2 - 3C_3\dot{\theta})(-\frac{V\cos(\theta) + H\sin(\theta)}{EI}) = (\frac{V\cos(\theta) - H\sin(\theta)}{EI})(C_4 + C_5\rho + C_6\theta) \tag{3.106}$$

By comparing terms, one can show that

$$C_2 = C_3 = C_4 = C_5 = C_6 = 0 \tag{3.107}$$

Therefore:

$$\begin{aligned} \xi &= C_1 \\ \eta &= 0 \end{aligned} \tag{3.108}$$

Equations (3.108) give the general transformation for (3.103). It is possible to consider ξ and η as:

$$\xi(\rho, \theta) = 1 \tag{3.109}$$

$$\eta(\rho, \theta) = 0 \tag{3.110}$$

Hence, (3.95) can be simplified as an operator:

$$X = \frac{\partial}{\partial \rho} \tag{3.111}$$

To calculate canonical coordinates, one can use (3.96) and (3.97); however, the solution of below ODE is $r(\rho, \theta)$ [135], [116]:

$$\frac{d\theta}{d\rho} = \frac{\eta(\rho, \theta)}{\xi(\rho, \theta)} \tag{3.112}$$

and $s(\rho, \theta)$ will be:

$$s(\rho,\theta) = \left(\int \frac{d\rho}{\xi(\rho,\theta(r,\rho))}\right)\Big|_{r=r(\rho,\theta)} \tag{3.113}$$

where (3.96) and (3.97) can be considered as boundary conditions. Substituting (3.109) and (3.110) in (3.112) and (56) (3.113) yields:

$$r(\rho,\theta) = \theta \tag{3.114}$$

$$s(\rho,\theta) = \rho \tag{3.115}$$

which satisfies (3.96) and (3.97) respectively.

By defining *u(r)* as:

$$u(r) = \frac{1}{\frac{d\theta}{d\rho}} \tag{3.116}$$

One can show that:

$$\frac{du(r)}{dr} = -\frac{\frac{d^2\theta}{d\rho^2}}{\left(\frac{d\theta}{d\rho}\right)^2} \tag{3.117}$$

So according to (3.83), (3.84), and (3.85):

$$\frac{d^2\theta}{d\rho^2} = -u(r)^{-3}\frac{du(r)}{dr} \tag{3.118}$$

Substitution of (3.116) and (3.117) in (3.118) gives:

$$\frac{du(r)}{dr} = (\frac{V\cos(\theta) + H\sin(\theta)}{EI})u(r)^3 \tag{3.119}$$

Substitution of (3.114) and (3.115) in (3.119) will yield:

$$\frac{du(\theta)}{d\theta} = (\frac{V\cos(\theta) + H\sin(\theta)}{EI})u(\theta)^3 \tag{3.120}$$

For a first order ODE like (3.120) equation (3.93) can be written as [114], [122]:

$$\eta_\theta + (\eta_u - \xi_\theta)\omega - \xi_u\omega^2 = \xi\omega_\theta + \eta\omega_u \tag{3.121}$$

Where:

$$\omega = (\frac{V\cos(\theta) + H\sin(\theta)}{EI})u(\theta)^3$$

Substituting ω and its derivatives in (3.121) yields

$$
\begin{aligned}
&\eta_\theta + \frac{1}{EI}(\eta_u - \xi_\theta) \\
&(V\cos(\theta) + H\sin(\theta))u^3 \\
&-\frac{1}{(EI)^2}\xi_u(V\cos(\theta) + H\sin(\theta))^2 u^6 \\
&= \frac{1}{EI}\xi(-V\cos(\theta) + H\sin(\theta))u^3 \\
&+\frac{3}{EI}\eta(V\cos(\theta) + H\sin(\theta))u^2
\end{aligned}
\tag{3.122}
$$

From (3.122), equating u^6 and free term, it is found that

$$\xi_u = \eta_\theta = 0 \tag{3.123}$$

By comparing the coefficients of u^3, one can write

$$(\eta_u - \xi_\theta)(V\cos(\theta) + H\sin(\theta)) = \xi(-V\sin(\theta) + H\cos(\theta)) \tag{3.124}$$

To satisfy (3.124), ξ must be assumed as zero

$$\xi = 0 \tag{3.125}$$

hence (3.122) becomes

$$\eta_u u = 3\eta \tag{3.126}$$

The integral of this ODE is:

$$\eta = u^3 \tag{3.127}$$

So (3.95) becomes:

$$X = u^3 \frac{\partial}{\partial u} \tag{3.128}$$

Based on (3.128), canonical coordinates can be calculated from (3.112) and (3.113) as:

$$r(\theta,u) = \theta \tag{3.129}$$

$$s(\theta,u) = -\frac{1}{2u^2} \tag{3.130}$$

Substituting (3.129) and (3.130) in (3.98) yields:

$$\frac{ds}{dr} = \frac{1}{EI}(V\cos(r) + H\sin(r)) \tag{3.131}$$

So:

$$s = \frac{1}{EI}(V\cos(r) + H\sin(r)) + C_1 \tag{3.132}$$

Further, by substituting (3.116), (3.129) and (3.130) in (3.132) one gets:

$$(\frac{d\theta}{d\rho})^2 = \frac{2}{EI}(H\cos(r) - V\sin(r)) + C_1 \tag{3.133}$$

By considering boundary condition (3.62), C_1 becomes:

$$C_1 = (\frac{M_0}{EI})^2 - \frac{2}{EI}(H\cos(\theta_f) - V\sin(\theta_f)) \tag{3.134}$$

where θ_f is final angle in the tip.

Solution of (3.133) yields:

$$\rho = \int \frac{d\theta}{\sqrt{\frac{2}{EI}(H\cos(\theta) - V\sin(\theta)) + C_1}} + C_2 \tag{3.135}$$

From equations (3.59) and (3.60) one can write equation (3.133) as:

$$\int_0^a dx = \int_0^{\theta_f} \frac{d\theta\cos(\theta)}{\sqrt{\frac{2}{EI}(H\cos(\theta) - V\sin(\theta)) + C_1}} \tag{3.136}$$

$$\int_0^b dy = \int_0^{\theta_f} \frac{d\theta\sin(\theta)}{\sqrt{\frac{2}{EI}(H\cos(\theta) - V\sin(\theta)) + C_1}} \tag{3.137}$$

which relationship, after the integration will yield the deflection at the tip of the not-straight cantilever beam.

3.16. Validation

The below examples are special cases of the presented general problem. All these presented cases refer to deflection in the non-linear domain and they have been formulated at different times and solved using different methods such as provided in [1], [34], [136]. Each solution has employed same formulation but different methods were used to prove the solution, which are identical with the solutions obtained from the proposed general formulation for the same problem. The three cases are recognized in the literature as the large deflection cases for straight cantilever beams subjected to point loads: cantilever beam subjected to vertical point force, cantilever beam subjected to moment at the tip and cantilever beam subjected to horizontal and vertical force at the tip.

3.16.1. Cantilever beam under vertical point force at tip

For a straight cantilever beam under a tip force, C_1 and ρ from (3.134) and (3.135) will simplify to:

$$C_1 = \frac{2V}{EI}\sin(\theta_0) \tag{3.138}$$

$$\rho = \int \frac{d\theta}{\sqrt{\frac{2}{EI}(-V\sin(\theta)) + C_1}} \tag{3.139}$$

Substituting (3.138) in (3.139) gives:

$$\rho = \int \frac{d\theta}{\sqrt{\frac{2V}{EI}(\sin(\theta_0) - \sin(\theta))}} + C_2 \tag{3.140}$$

Further, by applying the $\left.\frac{d\theta}{d\rho}\right|_{\rho=L} = 0$ as a boundary condition, one can show that $C_2 = 0$, and therefore:

$$\rho = \sqrt{\frac{EI}{2V}} \int \frac{d\theta}{\sqrt{(\sin(\theta_0) - \sin(\theta))}} \tag{3.141}$$

An identical solution was formulated using a different approach and proved in the reference [1] .

3.16.2. Cantilever beam under moment at tip

For a straight cantilever beam under a moment C_1 and y from (3.134) and (3.137), for tip deflection will simplify to:

$$C_1 = (\frac{M_0}{EI})^2 \tag{3.142}$$

$$y = -\frac{EI}{M_0}\cos(\theta) + C_1 \tag{3.143}$$

Further, assuming $y|_{\theta=0} = 0$ as a boundary condition C_2 will become:

$$C_2 = \frac{EI}{M_0} \tag{3.144}$$

therefore:

$$y = \frac{EI}{M_0}(1 - \cos(\theta)) \tag{3.145}$$

which was proved using another approach in [34] .

3.16.3. Nonlinear cantilever beam subjected to inclined point force at the tip

If in figure 3.7.1 horizontal force is considered as a fraction of the vertical force $H = nV$.

Equation (3.134) can be written as:

$$C_1 = \frac{2P\lambda}{EI} \tag{3.146}$$

where:

$$\lambda = \kappa_0 + \sin(\theta_0) - n\cos(\theta_0) \tag{3.147}$$

$$\kappa_0 = \frac{M_0^2}{2VEI} \tag{3.148}$$

Further, (78) can be written as:

$$\rho = \sqrt{\frac{EI}{2V}} \int \frac{d\theta}{\sqrt{(n\cos(\theta) - \sin(\theta) + \lambda)}} + C_2 \tag{3.149}$$

This solution was proved by a different method in [136] .

3.17. Sensitivity analysis of the non-straight beam

The sensitivity analysis for large deflection of micro-cantilever beams and AFM is carried out in this section. The main question here is, if one uses curved micro-cantilever beams how significantly its sensitivity is different from straight micro-cantilever beam? Manufacturing micro-cantilever beam like the one in figure 3.7.1 is relatively unchallenging. However, can such micro-beams be used as AFM probes? If micro-cantilever beam of AFM reaches a large deflection region, does it have the same sensitivity? To answer these questions, the AFM micro-cantilever beam of [135] was considered as figure 3.7.2. The dimensions and the mechanical properties of micro-cantilever beam are presented in table 3.7.1.

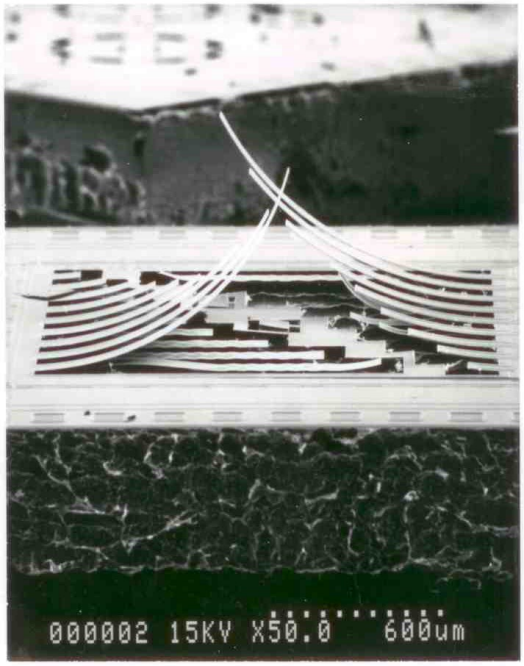

Figure 3.7.1. Permanently curved micro-cantilever beams (CONCAVE Laboratory)

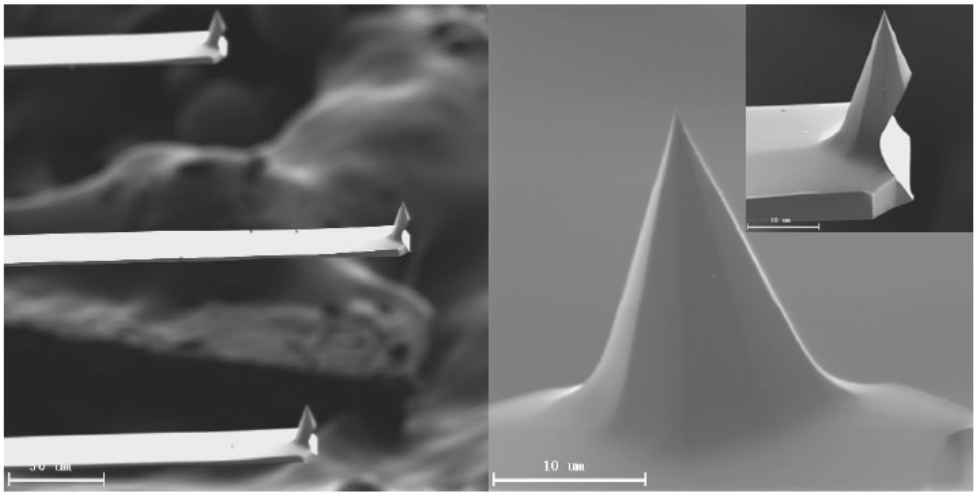

Figure 3.7.2. AFM Micro-cantilever beam and its tip close up [135]

Table 3.7.1. Dimensions and mechanical properties of AFM [135]

Length [μm]	Width [μm]	Thickness [μm]	Young Modulus [GPa]	Tip's length [μm]	Density [Kgm^{-3}]
299	35	0.96	169.5	15	2330

First, a very important result from equation (3.135) can be derived. This equation shows that the deflection of straight beam is same as curved beam when they have same dimensions and are subjected to same loads. Therefore, the deflection of the curved beams is same as straight beam's behavior. In order to evaluate the effect of different parameters on deflection, at the first step geometry and then mechanical properties of beam were considered constants. In order to simplify the results all analysis were carried out for the above mentioned AFM beam. All variations were considered around this AFM beam. Referring to the equations (3.135) to (3.137), the variables that can effect curvature, vertical and horizontal deflections are $P, I, L, \theta_f, \theta_0, u$,where P is applied force on the tip of cantilever beam, I is moment inertia of cross section, L is length of cantilever, θ_f is the final angle of free end of cantilever beam after deflection, θ_0 is the angle of applied force to the tip of AFM beam with horizontal surface and u is length of tip. As one can see, there are six different variables. P is assumed to vary from 0 to 2 [μN] . For the problem, the maximum value of P is selected. There are two criteria's that one has to consider. One criterion is the buckling problem. If one assumes that as worst case, the tip of beam touches the surface in the way that all applied forces are horizontal, so maximum stress for a straight cantilever beam under eccentric force under buckling can be calculated from the secant formula [123]:

$$\sigma_{\max} = \frac{P}{A}(1 + \frac{ec}{r^2}\sec(\frac{L}{2r}\sqrt{\frac{P}{EA}})) \quad (3.150)$$

where:

$\sigma_{\max} = 113 \times 10^{6}[Pa]$ is the ultimate stress

P is the applied force

$A = 3.360 \times 10^{-11}[m^2]$ is the cross section of micro-cantilever beam

$e = 15 \times 10^{-6}[m]$ is the eccentric distance which is tip's length

$c = 0.48 \times 10^{-6}[m]$ is half of thickness

$r = 0.277 \times 10^{-6}[m]$ is the radius of gyration

$L = 299 \times 10^{-6}[m]$ is the length of micro-cantilever beam

$E = 169.5 \times 10^{9}[Pa]$ is Young modulus of micro-cantilever beam

$I = 2.58048 \times 10^{-24}[m^4]$ is the moment of inertia

Substituting above values in equation (3.150) will yield to:

$$2.9762 \times 10^{10} P(1 + 93.75 \times \sec(226.051\sqrt{P})) = 1.13 \times 10^{8} \quad (3.151)$$

The solution of this equation for P is:

$$P = 20.7 \times 10^{-6}[N]$$

The second criterion for P is maximum stress due to the bending moment. From bending stress one can write:

$$\sigma_{\max} = \frac{Mc}{I} = \frac{PLc}{I} = \frac{P \times 299 \times 10^{-6} \times 0.48 \times 10^{-6}}{2.58048 \times 10^{-24}} = 113 \times 10^{6} \quad [Pa] \tag{3.152}$$

The terms in this equation are introduced above. The maximum force derived is found as $\mathrm{P} = 2.07 \times 10^{-6}[N]$. Following the aforementioned equations and considering the force as $\mathrm{P} = 2.07 \times 10^{-6}[N]$ in nonlinear area, the applied force will create large deflection on micro-cantilever. Also, if one assumes small deflection for this force, the deflection will be:

$$\delta = \frac{\mathrm{PL}^3}{3EI} = \frac{2 \times (299 \times 10^{-6})^3}{3 \times 169.5 \times 10^{9} \times 2.58045 \times 10^{-24}} = 40.7 \times 10^{-6}[m] \tag{3.153}$$

which represents 14% of length of micro-cantilever beam and 42 times larger than its thickness. So for analysis of micro-cantilever beam maximum force $2.0\ [\mu N]$ was considered. In all cases four forces were considered, $\mathrm{P} = 0.01 \times 10^{-6}, 0.1 \times 10^{-6}, 1.0 \times 10^{-6}$ and $2.0 \times 10^{-6}[N]$. Interval of θ_0 is assumed as $0 \le \theta_0 \le \frac{\pi}{2}$, because contact angle between surface and tip of AFM micro-cantilever beam can start from horizontal to reach vertical direction. Also, for θ_f was considered same interval as θ_0. If micro-cantilever does not

deflect, under zero force $\theta_f = 0$. Maximum θ_f cannot reach at $\frac{\pi}{2}$, because, if one assumes $\theta_f = \frac{\pi}{2}$, so:

$$R = \frac{L}{\theta_f} = \frac{2 \times 299 \times 10^{-6}}{\pi} = 190 \times 10^{-6} \ [m] \tag{3.154}$$

In this case, R represents the deflection. This deflection is 63% of length of the micro-cantilever beam. Figure 3.4.2, shows that in $\frac{\delta_h}{L} = 0.63$ cantilever beams lose their sensitivity with respect to the applied force. So $\theta_f = \frac{\pi}{2}$ is an acceptable boundary for θ_f.

In all cases for θ_f and θ_0 angles were considered within the assume range: $\frac{\pi}{8}, \frac{\pi}{4}, \frac{5\pi}{12}, \frac{\pi}{2}$.

Three values were considered for length of the tip. The actual available value for u based on data in table 3.7.1 shows $u = 15 \times 10^{-6}[m]$. Two other theoretical values were one third and three times of effective value. First, analysis showed that u has little effect on sensitivity, so large variations of u were studied to produce a large range of results. In all cases for u the following three values were considered: 5×10^{-6}, 15×10^{-6}, $45 \times 10^{-6}[m]$.

Stiffness of the micro-cantilever beam is function of moment of inertia; clearly stiffness is an important factor in deflection of micro-cantilever beam. To evaluate the sensitivity of micro-cantilever beam with respect to the moment of inertia, three different moments of inertia were considered: $I = 1 \times 10^{-24}, 2 \times 10^{-24}, 3 \times 10^{-24}[m^4]$.

Four sets of analysis were performed for this specific AFM micro-cantilever beam. In the first set, sensitivity of micro-cantilever beam versus θ_f, θ_0 and P were studied. The sensitivity study of these variables were carried out in six different analysis:

1- Curvature (ρ) versus curvature angle θ.

2- Deflection in x direction versus curvature angle θ.

3- Deflection in y direction versus curvature angle θ.

4- Deflection in y direction versus deflection in x direction

5- Curvature (ρ) versus deflection in x direction.

6- Curvature (ρ) versus deflection in y direction.

First three analyses are direct solution of (3.135) to (3.137) for specific values of θ_f, θ_0 and P. The fourth analyses are implicit solution of (3.136) and (3.137), fifth one is implicit solution of (3.135) and (3.136) and final one is implicit solution of (3.135) and (3.137). In each analysis; for a specific value of θ_f, above mentioned values, the six analyses were performed by evaluating the variations of the variables with respect to variation of θ_0 and P. For example for the first set of analysis with $\theta_f = \frac{5\pi}{8}$ the six analyses are presented in figures 3.17.3 to 3.17.8.

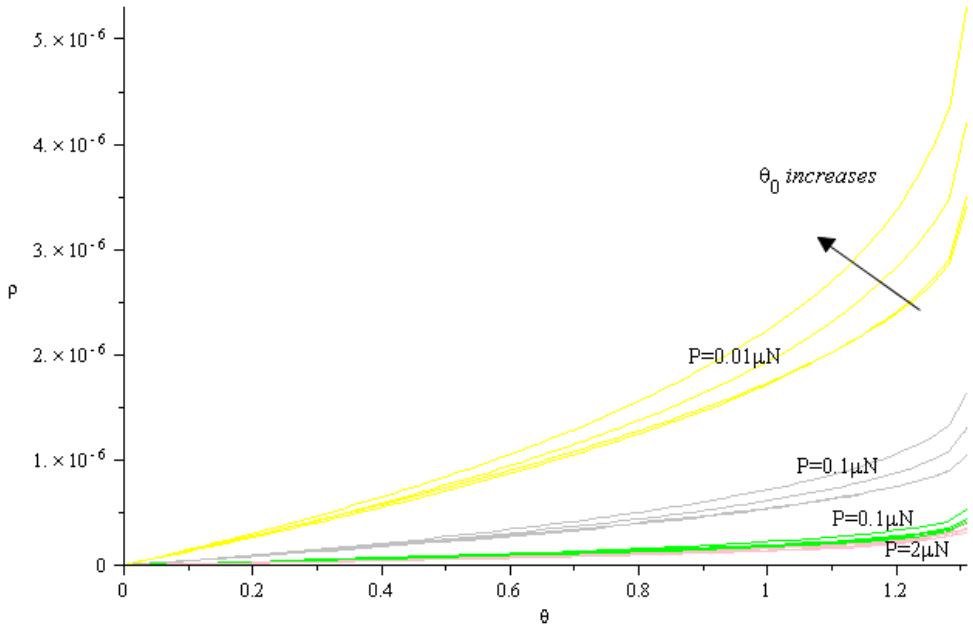

Figure 3.7.3. Numerical solution for the curvature versus the current angle as per (3.135), $\theta_f = \frac{5\pi}{8}$

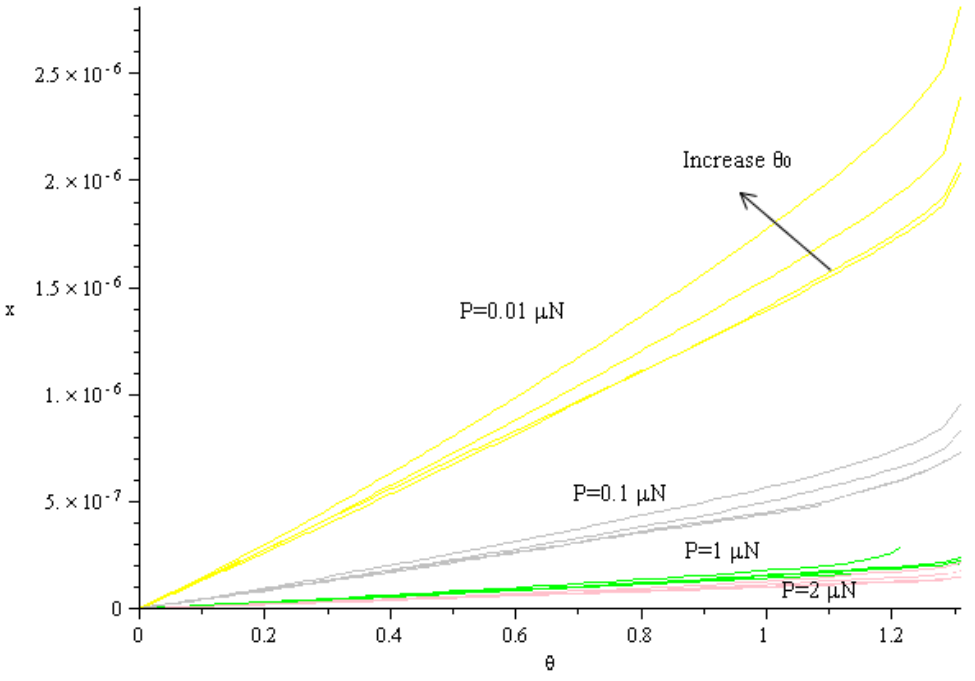

Figure 3.7.4. Numerical solution for the vertical deflection versus the current angle as per (3.136), $\theta_f = \frac{5\pi}{8}$

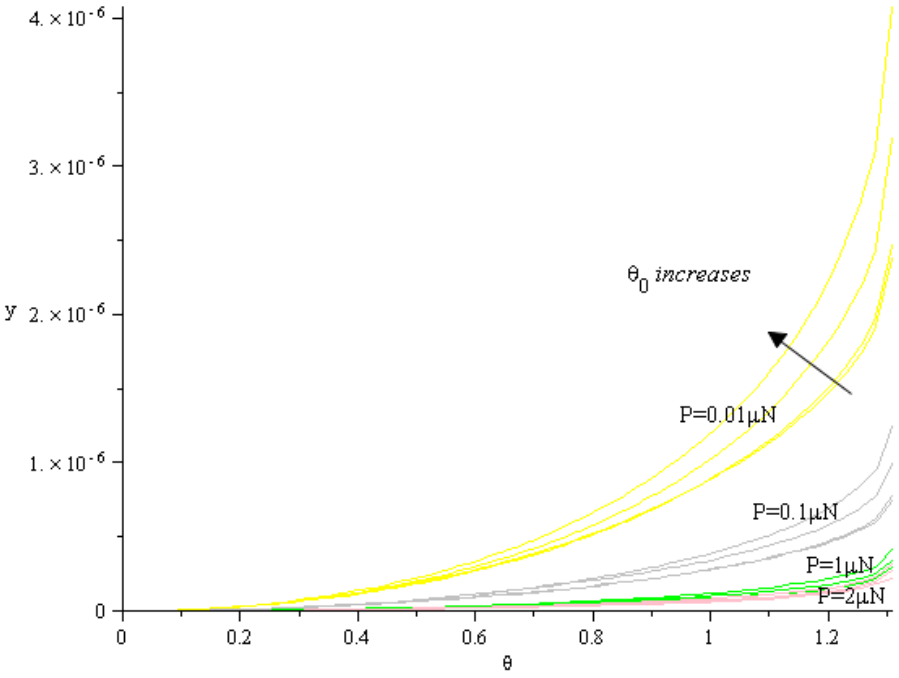

Figure 3.7.5. Numerical solution for the horizontal deflection versus the current angle as per (3.137), $\theta_f = \frac{5\pi}{8}$

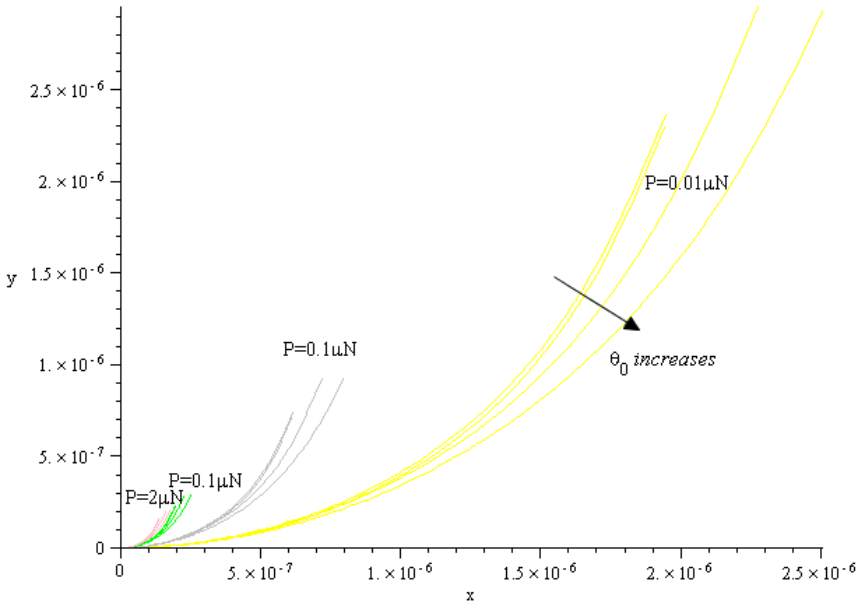

Figure 3.7.6. Numerical solution for the vertical deflection versus the horizontal deflection as per, (3.136) and (3.137),

$$\theta_f = \frac{5\pi}{8}$$

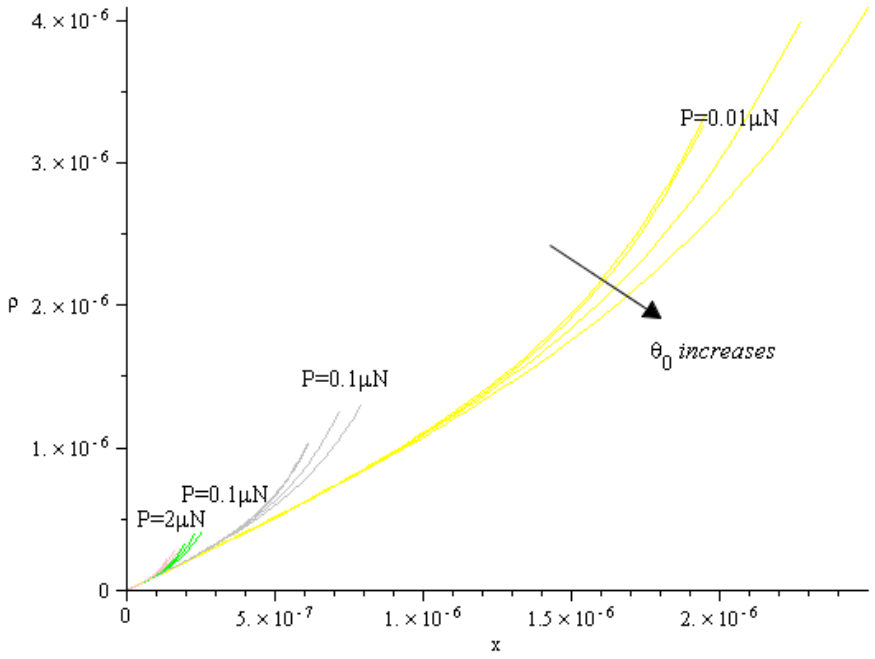

Figure 3.7.7. Numerical solution for the curvature versus the horizontal deflection as per, (3.135) and (3.136),

$$\theta_f = \frac{5\pi}{8}$$

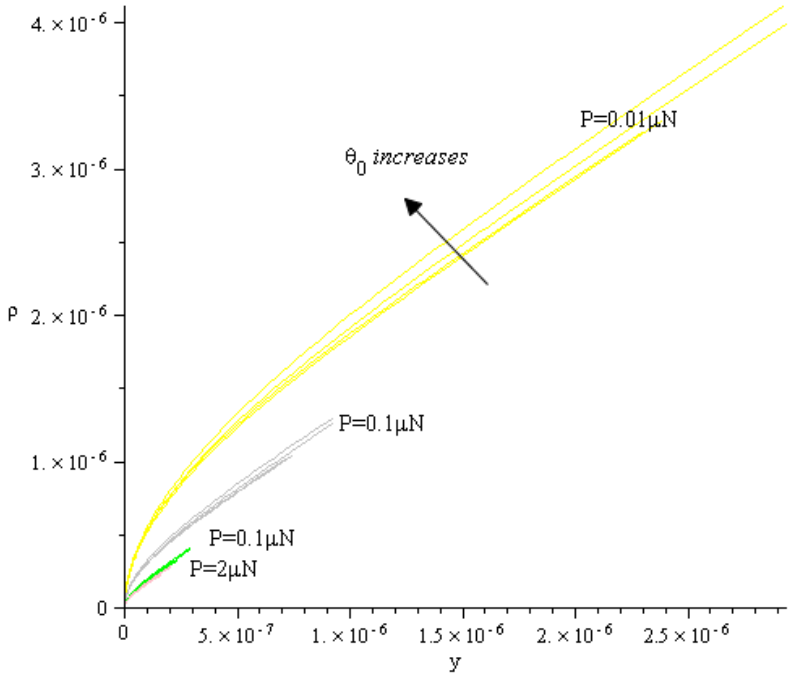

Figure 3.7.8. Numerical solution for the curvature versus the horizontal deflection as per, (3.135) and (3.137),

$$\theta_f = \frac{5\pi}{8}$$

One can see that θ_0 (the contact angle of tip with surface) has significant effect on nonlinear domain for large force. This effect increases by increasing the force. So if the micro-cantilever beam is used in large forces, it is more sensitive to θ_0.

The numerical analysis shows that solution of equation (3-136) for $\theta_f = \frac{\pi}{8}$ in $P = 0.01\ [\mu N]$ varies by 28% and by varying θ_0 from 0 to $\theta_0 = \frac{\pi}{2}$ and for $P = 2.0\ [\mu N]$ variation of the solution is of 32%. If θ_f increases to $\frac{\pi}{2}$ for any force the solution variation for (3.136) is almost 50%. This variation is almost similar to (3.135) and (3.137). For (3.135), solution for $\theta_f = \frac{\pi}{8}$ varies 10% for $P = 0.01\ [\mu N]$ and 12% for $P = 2.0\ [\mu N]$. For $\theta_f = \frac{5\pi}{8}$ the variation of solution for any force is almost 25%. For $\theta_f = \frac{\pi}{8}$ and $P = 0.01\ [\mu N]$ variation of θ_0 from $\frac{\pi}{8}$ to $\theta_0 = \frac{\pi}{2}$, in equation (3.137), creates 9% variation in solution, and in $\theta_f = \frac{5\pi}{8}$ and $P = 2.0\ [\mu N]$ the solution varies by 50%.

Implicit solutions give similar results to variation of θ_0. For any force at $\theta_f = \frac{\pi}{8}$ variation of θ_0 from 0 to $\theta_0 = \frac{\pi}{2}$ changes approximately 16% the implicit solution of (3.136) and (3.137), while for $\theta_f = \frac{5\pi}{8}$ this value increases to 39%.

In implicit solution of (3.135) and (3.136) yields an antithetical behavior with respect to other solutions. For any force at $\theta_f = \frac{\pi}{8}$ variation of θ_0 from 0 to $\theta_0 = \frac{\pi}{2}$ approximately 16% variation is solution is encountered, but by increasing θ_f from 0 to $\frac{5\pi}{8}$ the variation of the solution reduces to 12%.

Behavior of the implicit solution of (3.135) and (3.137) shows that variation of solution for 0, while any force is around 15% and by increasing θ_f to $\frac{5\pi}{8}$ for any force variation the solution is higher by 50%.

As mentioned above θ_0 is angle between horizontal axis and applied force and it is shown in the above results that variation of θ_0 has significant effect on solution of explicit and implicit solutions (3.135) to (3.137). Although this effect is reduced by increasing the force, it is still significant. The reason of this reduction can be explained by the illustration in figure 3.4.2. As one can see in this figure, the deflection increases much less than force as the force reaches the nonlinear domain. Hence for the forces that makes large deflection significant change occur in the solution. Changing θ_0 does not affect deflection too much. The behavior of the solution with respect to the variation of θ_0 comes from the nature of integrals in the equations.

Sensitivity of presented AMF micro-cantilever beam to force P is illustrated in above graphs. Variation of P in all implicit solutions has the same affect. In the all above graphs, for any X (angle θ_0, deflection in X or Y directions) axis and Y axis, by

increasing force P sensitivity of axis reduces for any angle of curvature. This means that for ρ, X and Y, variation of angle for large forces are higher than for small forces for the same deflection. Implicit solutions of (3.136) and (3.137) are identical to the solutions presented in [8] which represent only particular cases of the general solution in the present work. For a specified deflection in X direction large force produces large deflection in Y direction. These phenomena in simple case can be explained from figure 3.4.2. It is clear that in any case, deflection of beam in X direction is less than deflection in Y direction.

Implicit solutions of (3.135) and (3.135) yield the same pattern as implicit solutions of (3.136) and (3.137). For a specific deflection in X direction for large force, one will obtain larger curvatures.

Solution of (3.135) and (3.137) follows the same logical algorithm as above. On the other hand the solution shows that for large deflections in Y direction and for any force the relation between deflections in Y direction is linear with respect to curvature.

The performed investigation shows that the variation of θ_f does not change the pattern of the above graphs, although it affects the solution of the equations.

Numerical analysis shows that for $P = 0.01\,[\mu N]$ any θ_0 variation and any varieties of θ_f in the solution of (3.136) yields variation of 82% while for $P = 2\,[\mu N]$ this variation ranges between 72% and 65% when θ_0 varieties from 0 to $\frac{\pi}{2}$. In the equation (3.137) for $P = 0.01\,[\mu N]$ and $\theta_0 = \frac{\pi}{8}$ variation of θ_f from 0 to $\frac{\pi}{2}$ yields change in the solution of 79% whereas for same force with $\theta_0 = \frac{\pi}{2}$ this variation of the solution is 68%. These

values for $P = 2\,[\mu N]$ are 79% and 70%, respectively. Explicit solution of (3.135) which gives the curvature yields variation of θ_f. As above, the numerical analysis performed for sensitivity of curvature deflection to θ_f shows that for any force and $\theta_0 = \frac{\pi}{8}$, variation of θ_f affects by 74% the solution and this value changes to 63% when θ_0 is $\frac{\pi}{2}$.

Effect of variation of θ_f on all implicit solutions, (3.135) and (3.136), (3.135) and (3.137), (3.136) and (3.137) is same. For any force and $\theta_0 = \frac{\pi}{8}$ the implicit solutions vary by 74% and when θ_0 is $\frac{\pi}{2}$, the variation of solution reduces to 63%.

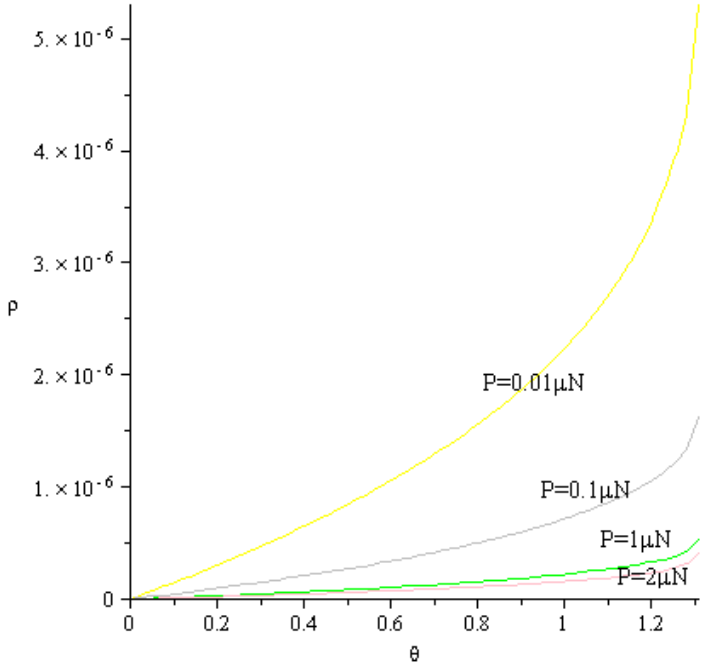

Figure 3.7.9. Numerical solution for curvature versus the current angle as per (3.135) for different tip length $\theta_f = \frac{5\pi}{8}$ and $\theta_0 = \frac{\pi}{2}$

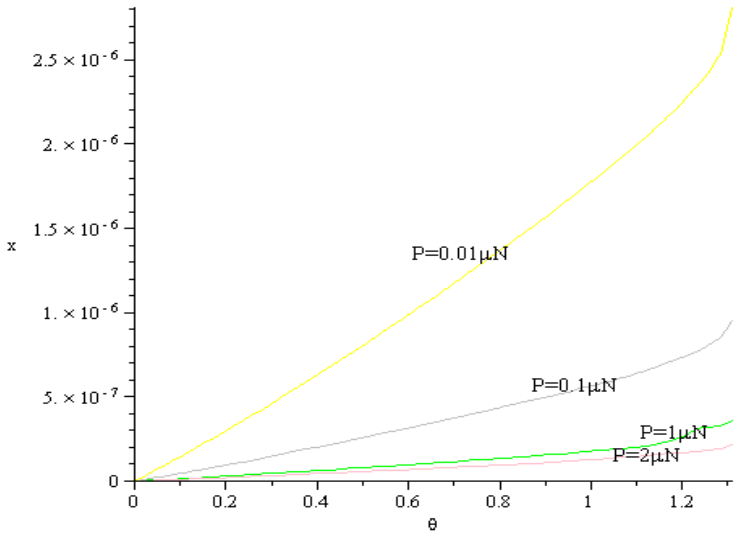

Figure 3.7.10. Numerical solution for horizontal deflection versus the current angle as per (3.136) for different tip length $\theta_f = \frac{5\pi}{8}$ and $\theta_0 = \frac{\pi}{2}$

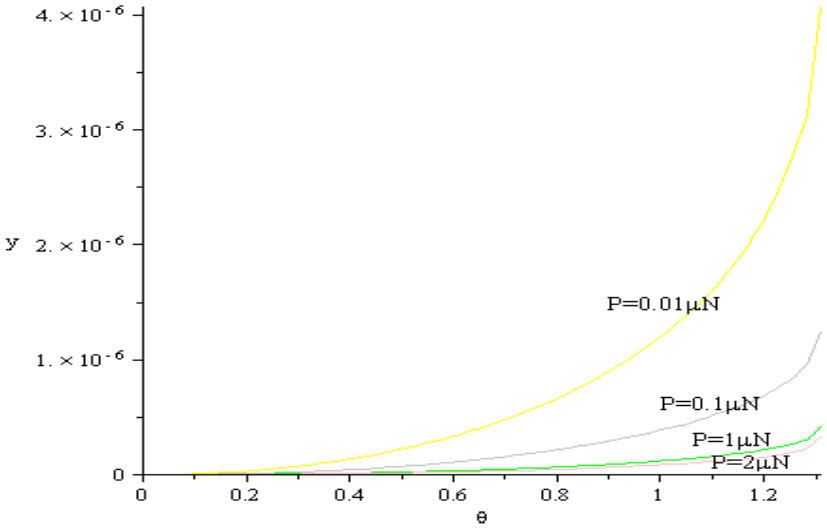

Figure 3.7.11. Numerical solution for vertical deflection versus the current angle as per (3.137) for different tip length $\theta_f = \frac{5\pi}{8}$ and $\theta_0 = \frac{\pi}{2}$

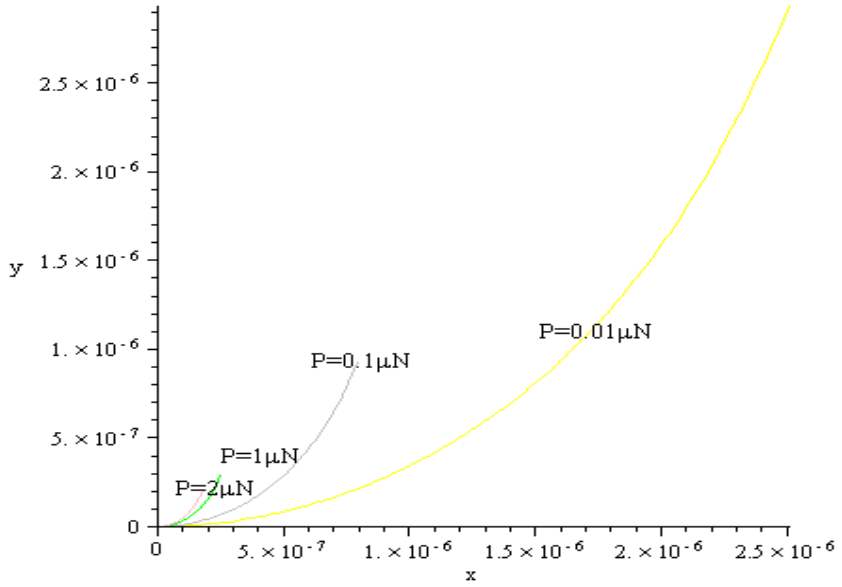

Figure 3.7.12. Numerical solution for vertical deflection versus the horizontal deflection as per (3.136) and (3.137) for different tip length $\theta_f = \frac{5\pi}{8}$ and $\theta_0 = \frac{\pi}{2}$

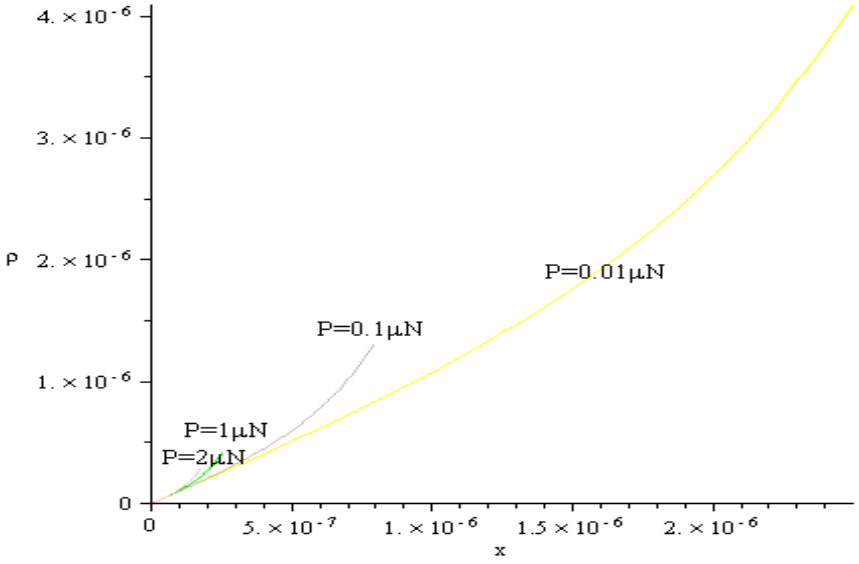

Figure 3.7.13. Numerical solution for curvature versus the horizontal deflection as per (3.135) and (3.136) for different tip length $\theta_f = \frac{5\pi}{8}$ and $\theta_0 = \frac{\pi}{2}$

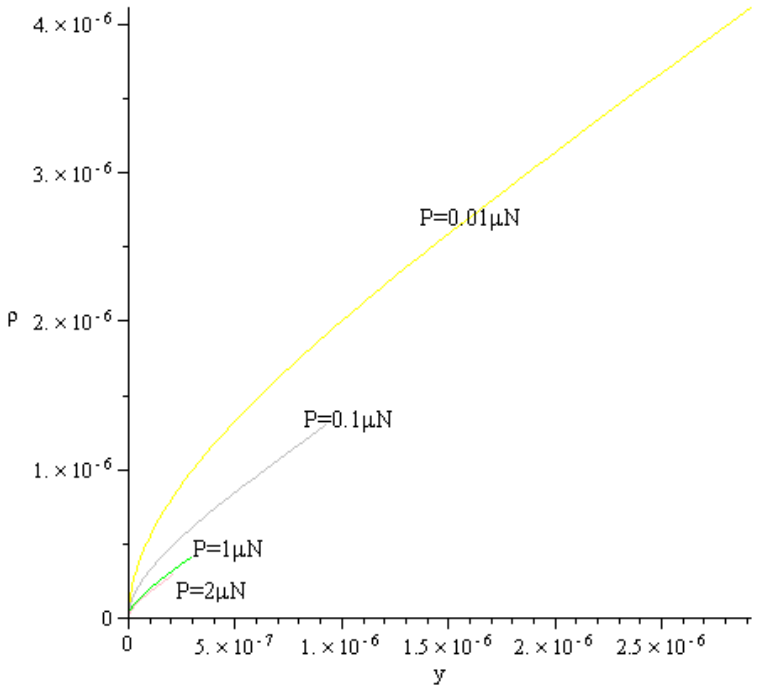

Figure 3.7.14. Numerical solution for curvature versus the vertical deflection as per (3.135) and (3.137) for different tip length $\theta_f = \frac{5\pi}{8}$ and $\theta_0 = \frac{\pi}{2}$

The second set of analyses of the sensitivity was focused towards the study of the effect of the tip length on the explicit and implicit solution of the equations (3.135) to (3.137). Figures 3.17.9 to 3.17.14 show a sample set of implicit and explicit the numerical solution for $\theta_0 = \frac{\pi}{2}$ and $\theta_f = \frac{5\pi}{8}$ with different tip length. Figures 3.17.9 to 3.17.11 are implicit integral of (3.135) to (3.137) for different tip lengths and forces. Also figures 3.17.12 to 3.17.14 are explicit solutions of (3.135) to (3.137) for different tip lengths and forces. Comparing this set of analysis with pervious set, sensitivity analysis for θ_0, θ_f and P ,shows that the pattern of all graphs are the same. Sensitivity analysis shows that for any force with any θ_0 and θ_f, the variation of u affects neither the explicit solution nor the implicit solution. Numerical analysis shows that the moment about

neutral axis was created by H force and is negligible as it yields between 50 times to 100 less in value when compared to the moment created by force V . Moment was created by H and V are $M_0 = H.u$ and $M_0 = V(1-x)$ respectively.

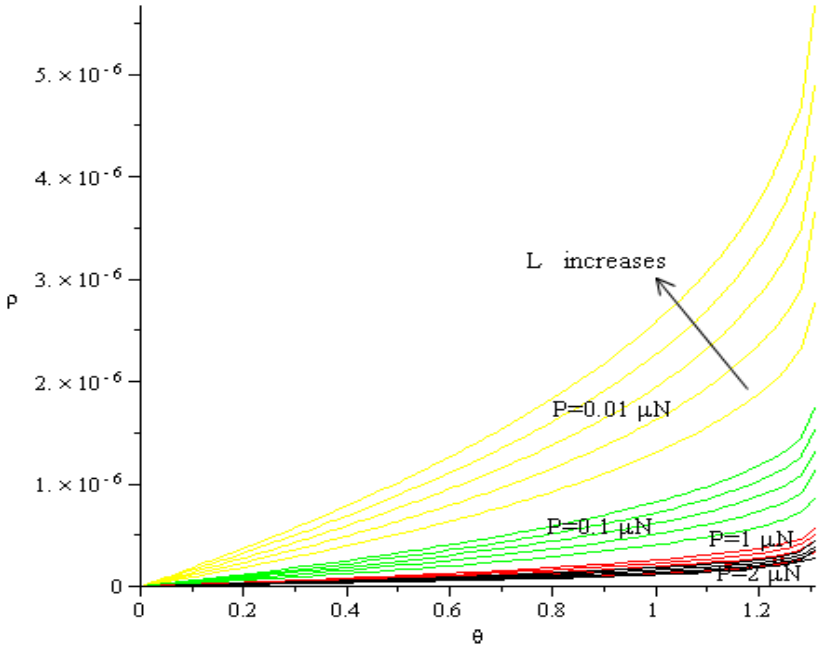

Figure 3.7.15. Numerical solution for curvature versus the current angle as per (3.135) for different length $\theta_f = \frac{5\pi}{8}$ and $\theta_0 = \frac{5\pi}{8}$

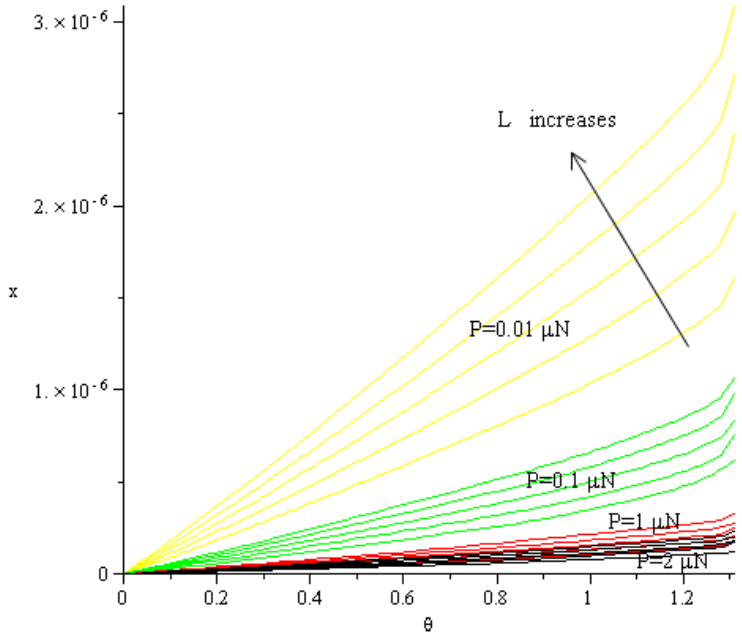

Figure 3.7.16. Numerical solution for horizontal deflection versus the current angle as per (3.136) for different length $\theta_f = \frac{5\pi}{8}$ and $\theta_0 = \frac{5\pi}{8}$

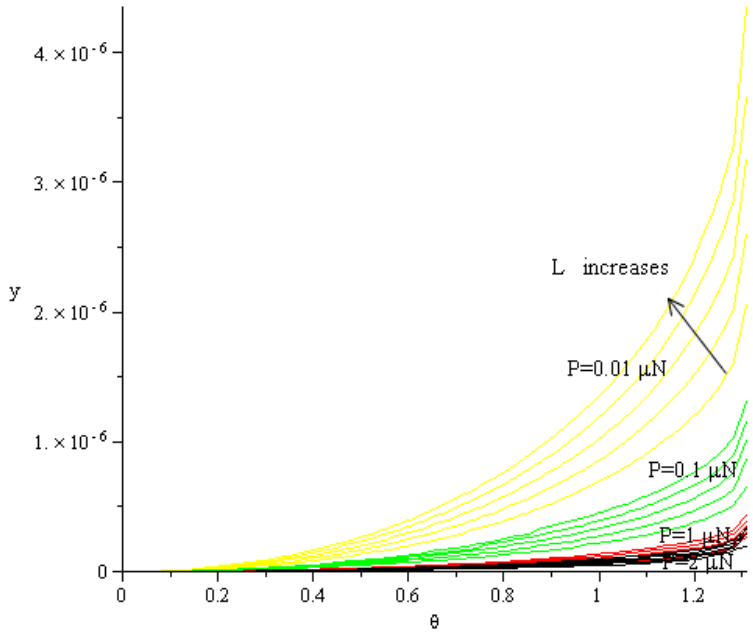

Figure 3.7.17. Numerical solution for vertical deflection versus the current angle as per (3.137) for different length $\theta_f = \frac{5\pi}{8}$ and $\theta_0 = \frac{5\pi}{8}$

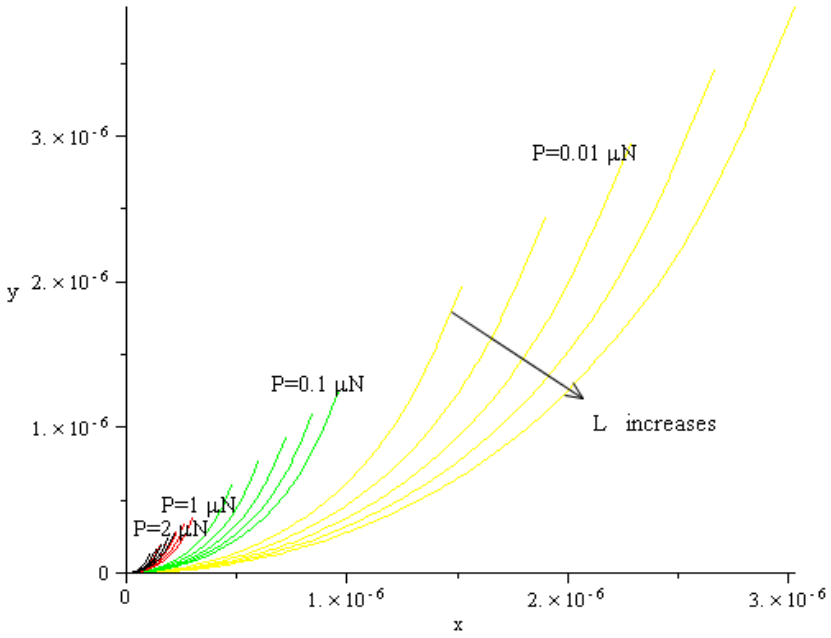

Figure 3.7.18. Numerical solution for vertical deflection versus the horizontal as per (3.136) and (3.137) for different length $\theta_f = \frac{5\pi}{8}$ and $\theta_0 = \frac{5\pi}{8}$

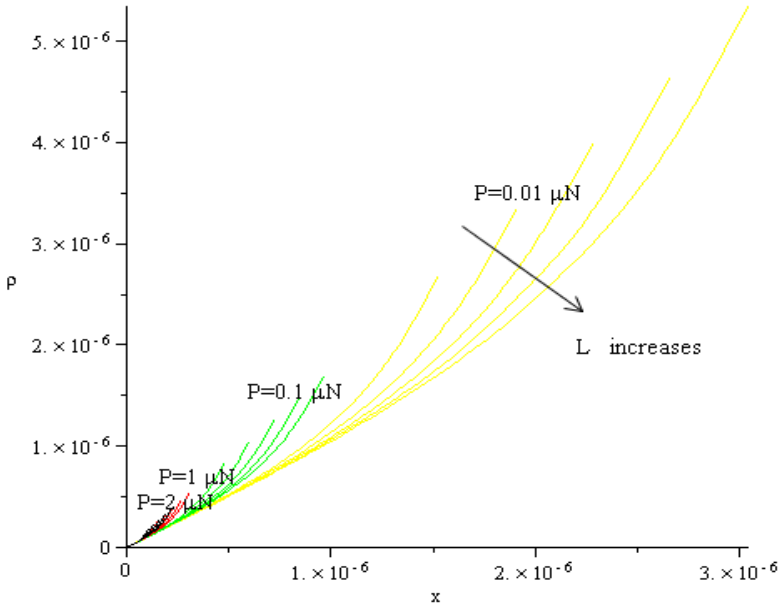

Figure 3.7.19. Numerical solution for horizontal deflection versus the current angle as per (3.135) and (3.136) for different length $\theta_f = \frac{5\pi}{8}$ and $\theta_0 = \frac{5\pi}{8}$

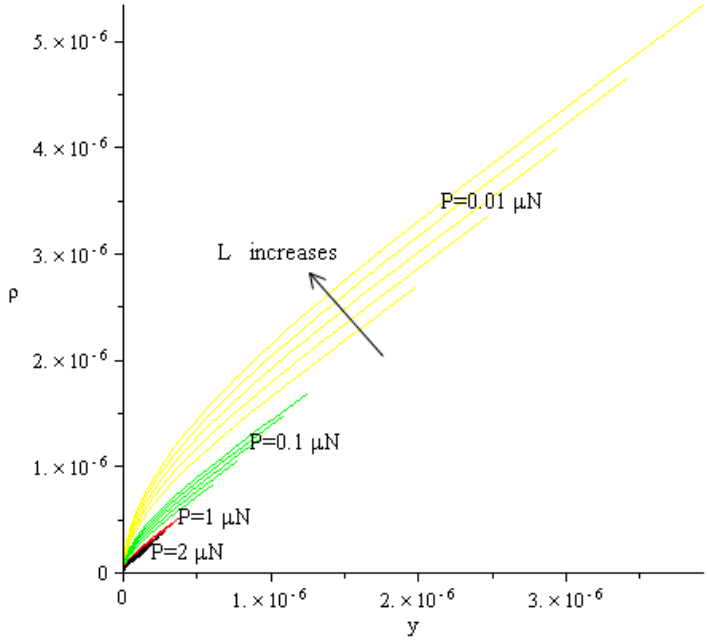

Figure 3.7.20. Numerical solution for curvature versus the vertical deflection as per (3.135) and (3.137) for different length $\theta_f = \frac{5\pi}{8}$ and $\theta_0 = \frac{5\pi}{8}$

Figures 3.17.15 to 3.17.20 illustrate the implicit and the explicit numerical solution of integrals (3.135) to (3.137) for $\theta_0 = \theta_f = \frac{5\pi}{8}$ and different lengths of the micro-cantilever beam: 200, 250, 300, 350 and 400 μm. It is clear that the curvatures and deflections increase at any force when the length of beam increases. However, sensitivity reduces when the applied force increases. Again, the cause of this phenomenon can be explained by figure 3.4.2. As one can see from this graph, the deflection increases just slightly by increasing the force within the nonlinear range. Numerical analysis shows that, sensitivity in y direction is almost similar to the one in x direction, however, less than the sensitivity of the curvature. For any force and any angles θ_0 and θ_f deflection in x direction which is the solution of (3.136) varies in average more than 100% by increasing length from 200 to 400 μm. However, for y direction, solution of (3.137) in small forces

domain yields variation is 80% while for larger forces it rises to 100%. Solution of (3.135) varies with respect to length change, for $P = 0.01$ [μN]and any angle θ_0 and θ_f , the average variation is 94% while for $P = 2.0$ [μN] the average of variation of solution reduces to 72%. Numerical analysis of implicit solutions for (3.135), (3.136) and (3.135), (3.137) as well as (3.136), (3.137) show that for any force and angles variation of length, changes in solutions vary the solution by up to 100%. One can see that increasing the length yields increase in the sensitivity for all forces, but sensitivity decreases by increasing the deflection.

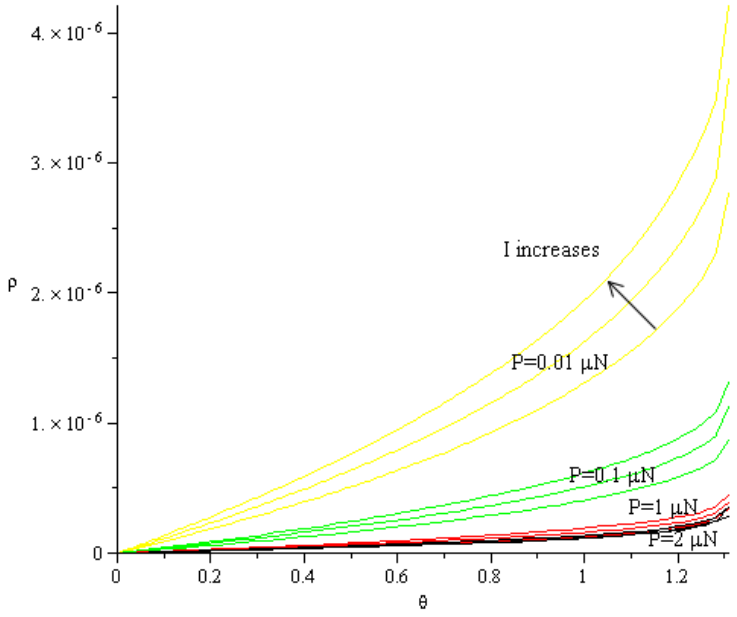

Figure 3.7.21. Numerical solution curvature versus the current angle as per (3.135) for different moment of inertia $\theta_f = \frac{5\pi}{8}$ and $\theta_0 = \frac{5\pi}{8}$

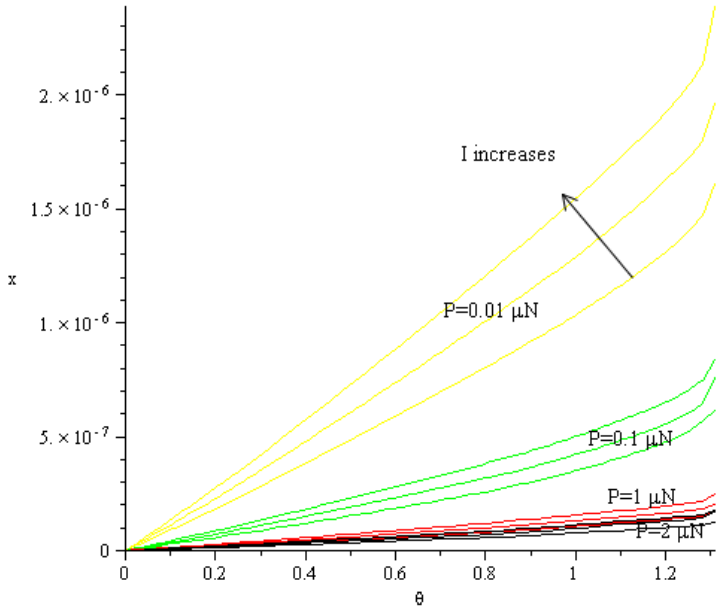

Figure 3.7.22. Numerical solution for horizontal deflection versus the current angle as per (3.136) for different moment of inertia $\theta_f = \frac{5\pi}{8}$ and $\theta_0 = \frac{5\pi}{8}$

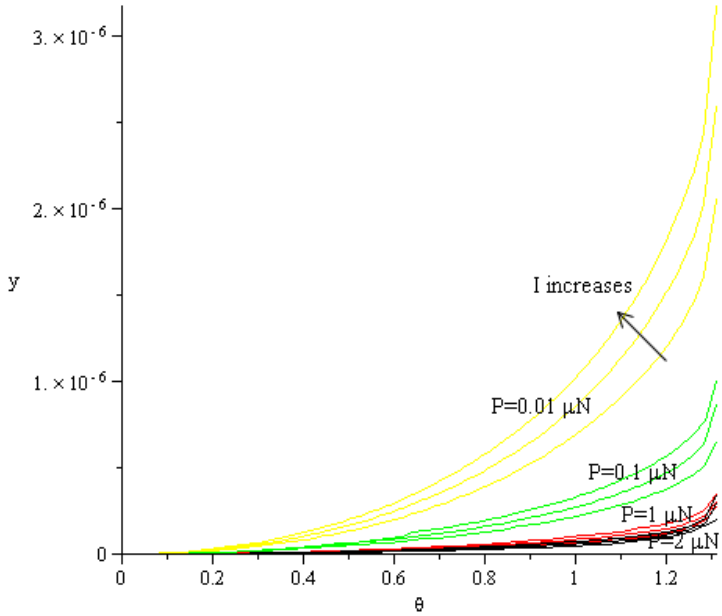

Figure 3.7.23. Numerical solution for vertical deflection versus the current angle as per (3.137) for different moment of inertia, $\theta_f = \frac{5\pi}{8}$ and $\theta_0 = \frac{5\pi}{8}$

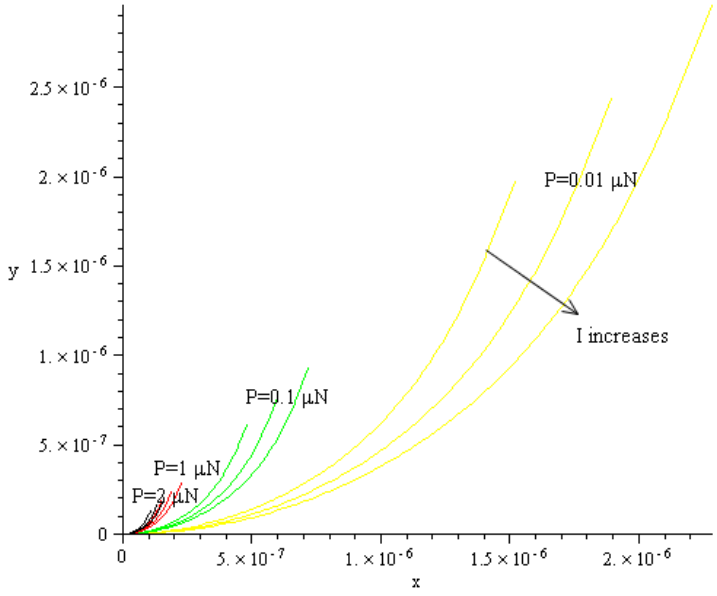

Figure 3.7.24. Numerical solution for vertical deflection versus the horizontal deflection as per (3.136) and (3.137) for different moment of inertia, $\theta_f = \frac{5\pi}{8}$ and $\theta_0 = \frac{5\pi}{8}$

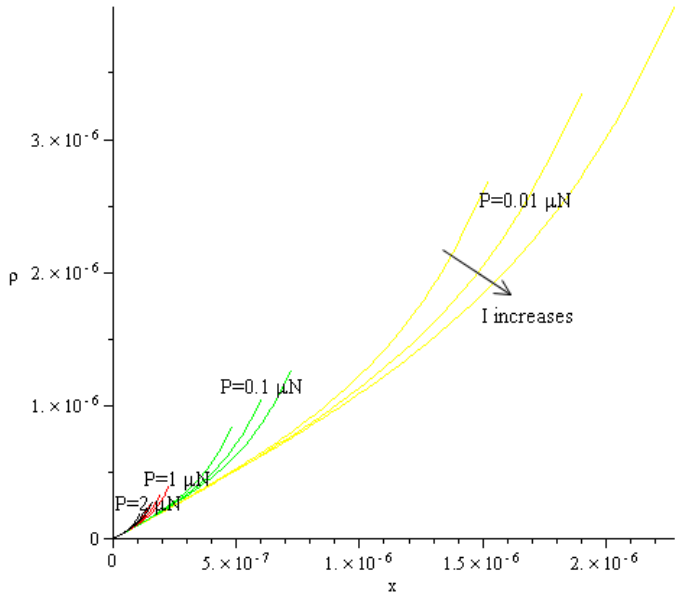

Figure 3.7.25. Numerical solution for curvature versus the horizontal deflection as per (3.135) and (3.136) for different moment of inertia, $\theta_f = \frac{5\pi}{8}$ and $\theta_0 = \frac{5\pi}{8}$

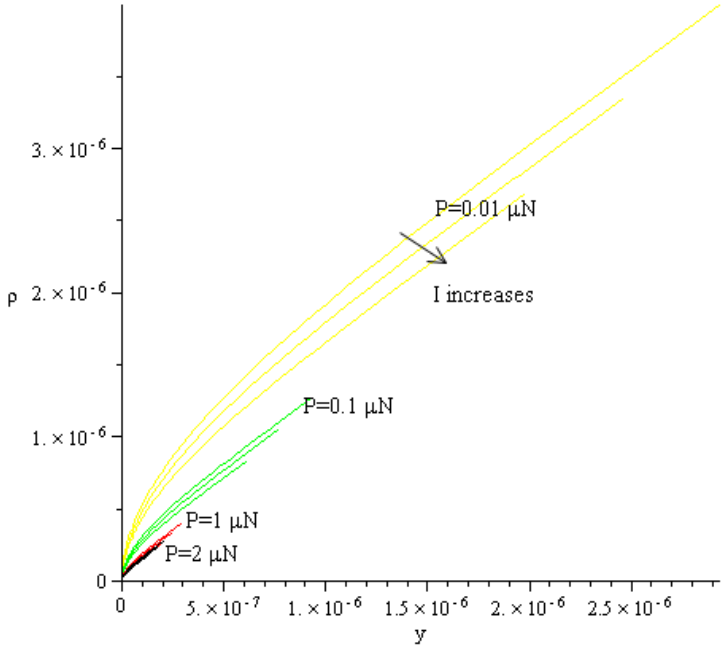

Figure 3.7.26. Numerical solution for curvature versus the vertical deflection as per (3.135) and (3.136) for different moment of inertia, $\theta_f = \frac{5\pi}{8}$ and $\theta_0 = \frac{5\pi}{8}$

Figures 3.17.21 to 3.17.26 illustrate the implicit and the explicit numerical solution of integrals (3.135) to (3.137) for constant angles $\theta_0 = \theta_f = \frac{5\pi}{8}$ for different moments of inertia for cross section of micro-cantilever beam, I = 2, 3, 4 μm^4. Figures 3.7-21 to 3.7-23 are implicit integrals of (3.135) to (3.137) for different moments of inertia. In all cases, an increment in the moment of inertia for a constant angle the sensitivity decreases. Meanwhile, increasing the applied force reduces the sensitivity. The solution of (3.135), (3.136) and (3.137) for any θ_0 and θ_f for $P = 0.01$ [μN] varies by 36%, 46% and 42% respectively. By increasing the force to $P = 2.0$ [μN]variations of the solution for (3.136) and (3.137) do not modify while for curvature as the solution of (3.135) reduces by 36%. Figure 3.7-24 shows the sensitivity of y with respect to x for different moments of inertia and forces. By increasing the moment of inertia, shown in the figure, sensitivity

decreases since cross section produces a stiffer structure. Also this fact can be seen in figures 3.7-25 and 3.7-26. Numerical analysis shows that for any implicit solution no matter what force or angle θ_0 and θ_f are, variation of the moment of inertia effects the solutions by 42%. It is important to note that although the moment of inertia changes twice, it does not affect more than 46% the deflection. This analysis shows that deflection of AFM micro-cantilever is not very sensitive to width and thickness of micro-cantilever beam.

3.18. Conclusion

The problem of large deflection of non-straight cantilever beams subjected to multiple loads consisting of point forces as well as point moment is formulated and a solution that yields the correct solution to the problem is presented. Lie group symmetry method is used to solve the general mathematical problem. Lie symmetry method is generally used to reduce the order of the differential equation that describes the large deflection equation of the cantilever beam subjected to multiple point loads, by one unit. The first order differential equation can usually be easily integrated and for all three particular cases presented for validation purpose, the solution found coincides with the particular solution presented in the references. The method brings a major advantage to the solution of the general problem, as it does not impose any restrictions on the curvature of the beam. The general proposed solution has applications in evaluation of the static large deflection of not-straight cantilever beam type structures. A general solution of the large deflection of

beams subjected to any type of loading has been obtained using Lie symmetry groups. The analytical formulation for the deflection could yield closed form solutions for some type of loadings. However, a numerical solution could be always obtained for any loading case. Although the solution might look laborious, this is the only solution to the general problem at this time. The validity of the solution is checked on two particular loading conditions, namely the ones available in the open literature: cantilever beam end-loaded with point moment force and. The solution produced by the Lie symmetry based method perfectly matches the corresponding solutions in the literature.

3.19. Summary

The chapter presents the results encountered by using a non-linear deflection model of a micro-cantilever beam subjected to point loads and moments. As an example an AFM beam is used in the discussion. Lie group symmetry method is used to solve the constitutive equation. From distinct cases are considered in the model:

1) Large deflection of a cantilever beam subjected to tip force.

2) Large deflection of a cantilever beam subjected to a tip moment

3) Large deflection of a cantilever beam made of non-linear material of Ludwick type subjected to a tip moment

4) Large deflection of a cantilever beam of non-linear material of Ludwick type subjected to a tip force.

The assumption of small deflection yields the results encountered by the linear model. Further, the performance of the non-straight beam is analyzed. Again, The Lie group formulation is used.

The conclusion of the study is that the deflection of because of same geometry and material subjected to same loading either straight or non-straight yield same deflection. The validation of the results in carried out for particular cases of analysis found in the open literature. A sensitivity analysis is carried out for the non-linear models.

Chapter4

Extraction Method for the Residual Stress in Multilayer Micro-plates under Large Deflections

Rationale

Chapter four presents a method of extraction of the built-in stress in film grown by thin film deposition in micro-plates. Although the fabrication processes are well controlled, the stress values are varying within + 40% and the assumption of variance yields more accurate solutions for the deflection than the ones obtained by assuming the exact inter-laminar stress yield by the deposition process. The extraction method was using on a gradient based optimization method. The estimation of the deflection in the model vs. the experimental method was based on static deflection matching. The estimation RMS of error based on model was reduced by 0.38 vs. the deflection resulting from the assumption of the nominal inter-laminar stress.

4.1 Introduction

Large deflection of micro-plates and analysis of inter layer residual stress in micro-plate based sensors are studied in this chapter. Large deflection of plates widely was studied [46, 137, 138] and as matter of fact, the governing equations were derived [139] in 1910 for a single layer plate. To solve the set of partial differential equations some new numerical methods like finite element method [140] was developed. Governing equations were recently developed [141] for small and large deflection by using tensor analysis for multilayer plates. The method is based on single layer plate deflection but the analytical analysis of multilayer plates has recorded more history. An analytical method for failure of laminated evaluate to calculate the stress-strain was derived on late 60's [142]. The nonlinear behavior of unidirectional laminated was developed for laminated composites and compared with experimental results [143] and the author showed that the solution of governed equations were fully in agreement with the experimental results. Dynamic analysis of multilayer composites was also studied by analytical methods and governed equation was derived [144]. Here the governing equation of multilayer composite material behavior in cylindrical coordinates form was derived. For a composite plates with different relaxed planar dimensions a new theory was presented and some particular cases were detailed [145]. For thicker plates under large deflection, higher accuracy was obtained in comparison to Von Karman theory. The governing equation was derived in [146] where the authors numerically solved the equations and compared the results with other theories. They showed that differences up to 33% among various theories were found. From the other side, manufacturing of micro-plates by MEMS technology [147,

148] started rising rapidly from 70's. Micromachining technology was used to fabricate perforated silicon nitride and porous silicon membranes [149]. Although the mechanical stability was a key issue for filtration, full characterize of the mechanical and the geometrical properties of the membrane was carried out. They used ANSYS for numerical simulation. However, the residual stress in layers was not considered although two layers were deposited on the substrate. To better understand the behavior of micro-plates, researchers use the classical plate theories were developed before the concept of miniaturization. One of the main issues in today MEMS structures is determination of the residual stress between the layers of a micro-plate. This residual stress is produced mainly by the thermal mismatching practically resulting from the deposition of different materials at different temperatures [150-152]. In [2], a membrane was manufactured of a weakly stressed quadruple stack. The plate contains of four different layers which are: SOI buried oxide, LPCVD nitride, densified PECVD and the devices passivation layer. The advantages of this method of manufacturing from authors point of view is the inherent co-integration process capability allowing fabricating sensors and their associated electronics on the same die. Previous studies considered residual stresses in layers and evaluated the internal stresses in each layer known output based on the fabrication. In the present study a method of evaluating the residual stress and the values of pre-determined stress have been adjusted. Authors of [153] optimized the performances of an existing piezoresistive silicon pressure sensor by changing the etchant. They used ANSYS to simulate the micro-plate behavior. Again, in any case they did not consider any internal stresses in their analysis. The work in [154] focused on manufacturing of two types of pressure sensors, the sensor cavity and the sensor

diaphragm by using SU-8.The advantage of this method from authors point of view is the possibility of measuring high pressure within wide range. They derived governing equations but they did not considered residual stress in their analysis. Resonant pressure sensor with piezoelectric was manufactured [155] on LTCC structure. The authors used this sensor to measure the resonant frequency while they were applying pressure on micro-plate. By applying pressure, the stress in the composing layers increased and this resulted in shifted resonant frequency. To calculate residual stress between layers, researchers use the classic formulation of Stoney equation [156]. In order to improve the accuracy of Stoney equation some analytical formulations were developed [157, 158]. In [159], authors used dynamic properties of micro-plates to calculate the internal stresses between layers. The drawback of these methods is the instability of the structure during measurement. Authors of [160] managed to prove that by moving the aluminum bond pads away from the structure they reduced the thermal stress in the micro-plate. A software algorithm was developed in [161] to calculate equivalent reference temperature, residual stresses and strains. They tested their software by comparing the results with those yield by ANSYS and experimental tests. As mentioned before the Stoney formula does not provide enough accuracy to evaluate the real residual stress. In [162] a method was presented to calculate the residual stress when the stress distribution is not uniform. A correction factor for Stoney formula was presented [163] to calculate stress in thicker coated layers. Another formula to correct Stoney equation was introduced in [164]. Authors proved that the original formula can yield up to 40% error.

4.2. Theory

Deflection of plates was studied widely in the case of single and composite layer [137, 138, 141]. In order to compare and have drawn a conclusion from experimental results, analytical results of small and large deflection of single and composite plates are presented here. Given the fact that the present investigations have focused on square plates and that the fabrication and the experiments are carried out on this shape, below we only discuss analytical formulations for square multi-layered plates subjected to uniform pressure.

4.3. Linear and nonlinear deflection of single layer plates

Based on definition for a thin plate [138], the ratio of its thickness to smaller length should be less than $\frac{1}{20}$. By this assumption, Kirchhoff hypotheses for isotropic, homogeneous, elastic plate are defined as follows[138]:

a) The deflection of the mid-surface is small compared to the thickness of plate.
b) The mid-plane remains unstrained subsequent to bending.
c) Plane sections initially normal to mid-surface remain plane and normal to the surface after the bending.
d) The stress normal to the mid-plane is small compared with the other stress components and is assumed as negligible.

Governing equation for small deflection of thin plate, based on Kirchhoff hypotheses, is derived as following:

$$\frac{\partial^4 w}{\partial x^4} + 2\frac{\partial^4 w}{\partial x^2 \partial y^2} + \frac{\partial^4 w}{\partial y^4} = \frac{p}{D} \tag{4.1}$$

w is deflection

P is uniformly distributed load per unite area

D is the flexural rigidity:

$$D = \frac{Eh^3}{12(1-\nu^2)} \tag{4.2}$$

one can show that maximum deflection of simple supported square plate subjected to uniform pressure under the assumption of linearity yields [138]:

$$w_{\max} = 0.0040 P_0 \frac{a^4}{D} \tag{4.3}$$

P_0 is the applied pressure

a is length of the square

E is Young's modulus

h is thickness of plate

ν is Poisson's ratio

Maximum deflection of the square plate with fixed supports subjected to uniform pressure under the assumption of linear deflection is [138]:

$$w_{\max} = 0.00126 P_0 \frac{a^4}{D} \tag{4.4}$$

Maximum deflection of simple supported square plate under uniform pressure in nonlinear deflection domain can be calculated from [137]:

$$(\frac{w_{\max}}{h})^3 + 5.8595(\frac{w_{\max}}{h}) = 0.26335\frac{P_0 a^4}{Eh^4} \tag{4.5}$$

The relation can calculate $w_{\max}$ as:

$$w_{\max} = \frac{1}{6}\frac{((108k_2 + 12\sqrt{12k_1^3 + 81k_2^2})^{\frac{2}{3}} - 12k_1)t}{(108k_2 + 12\sqrt{12k_1^3 + 81k_2^2})^{\frac{1}{3}}} \tag{4.6}$$

Where:

$$k_1 = 5.8595 \text{ and } k_2 = 0.26334\frac{P_0 a^4}{Eh^4}$$

Maximum deflection of fixed supports plate under uniform pressure in nonlinear analysis is calculated as shown below [46, 137]:

$$\lambda_m = \alpha_m a_0 \tag{4.7}$$

$$a = 2a_0 \tag{4.8}$$

$$\lambda_m = \pi(m - 0.25) \quad \text{m=1, 2, 3...} \tag{4.9}$$

$$\beta_m = \alpha_m = \frac{\lambda_m}{a_0} \tag{4.10}$$

$$X_m(x) = \frac{\cosh(\alpha_m x)}{\cosh(\alpha_m a_0)} - \frac{\cos(\alpha_m x)}{\cos(\alpha_m a_0)} \tag{4.11}$$

$$Y_n(y) = \frac{\cosh(\beta_n y)}{\cosh(\beta_n a_0)} - \frac{\cos(\beta_n y)}{\cos(\beta_n a_0)} \tag{4.12}$$

The force applied can be defined as a series:

$$q(x,y) = \sum_{m=1,3\ldots}^{\infty} \sum_{n=1,3\ldots}^{\infty} q_{mn} \cos(\frac{m\pi x}{a}) \cos(\frac{n\pi y}{a}) \tag{4.13}$$

Where:

$$q_{mn} = \frac{1}{a^2} \int_{-a_0}^{a_0} \int_{-a_0}^{a_0} q(x,y) X_m(x) Y_n(y) dx dy \tag{4.14}$$

If one defines $M_1^{rmp}, M_2^{rmp}\ M_3^{rmp}, M_2^{imr}$, K_1^{ip} and L_1^{jn} as functions like :

$$M_1^{rmp} = \int_{-a_0}^{-a_0} X_r \cos(\frac{m\pi x}{a}) \cos(\frac{p\pi x}{a}) dx \tag{4.15}$$

$$M_2^{rmp} = \int_{-a_0}^{a_0} X_r'' \cos(\frac{m\pi x}{a}) \cos(\frac{p\pi x}{a}) dx \tag{4.16}$$

$$M_3^{rmp} = \int_{-a_0}^{a_0} X_r' \cos(\frac{m\pi x}{a}) \sin(\frac{p\pi x}{a}) dx \tag{4.17}$$

$$M_2^{imr} = \int_{-a_0}^{a_0} X_i \sin(\frac{m\pi x}{a}) \cos(\frac{r\pi x}{a}) dx \tag{4.18}$$

$$K_1^{ip} = \frac{1}{a\alpha_m^2} \int_{-a_0}^{a_0} X_i X_m'' dx \tag{4.19}$$

$$L_1^{jn} = \frac{1}{a\beta_m^2} \int_{-b_0}^{b_0} Y_j Y_m'' dy \tag{4.20}$$

The large deflection equation for a plate is [137]:

$$D\nabla^4 w = q + h(w_{,xx}\Psi_{,yy} + w_{,yy}\Psi_{,xx} - 2w_{,xy}\Psi_{,xy}) \tag{4.21}$$

$$\nabla^4 \Psi = E(w_{,xy}^2 - w_{,xx}w_{,yy}) \tag{4.22}$$

Ψ is Airy stress function

w is deflection

Substitution of (4.6) into (4.21) and into (4.22) will give [137] :

$$w_{mn}(\frac{m^2}{a^2} + \frac{n^2}{a^2})^2 = \frac{q_{mn}}{\pi^4 D} -$$
$$\frac{4}{\pi^2 a^2 D} \sum_{p=2k+1}^{\infty} \sum_{q=2k+1}^{\infty} \sum_{r=1,..s=1,...}^{\infty} \sum_{}^{\infty} w_{pq} F_{rs} [\frac{p^2}{a^2} M_1^{rmp} N_2^{snq} + \frac{q^2}{a^2} M_2^{rmp} N_1^{snq} + 2\frac{pq}{a^2} M_3^{rpm} N_3^{sqn}] \tag{4.23}$$

$$F_{ij}(\lambda_i^4 + \lambda_j^4) + 2\sum_{p}^{\infty}\sum_{q}^{\infty} F_{pq}\lambda_p^2\lambda_q^2 K_1^{ip} L_1^{jq} =$$

$$\frac{\pi^4 E}{16a^2}\sum_{m=2k+1}^{\infty}\sum_{n=2k+1}^{\infty}\sum_{r=2k+1}^{\infty}\sum_{s=2k+1}^{\infty} w_{mn} w_{rs}(mnrsM_4^{imr}N_4^{jns} - m^2 s^2 M_1^{imr} N_1^{jns})$$

(4.24)

These series are simplification of the equations (4.21) and (4.22). To solve a large deflection of plate problem instead of using (4.21) and (4.22) which are two nonlinear differential equations, one can use (4.23) and (4.24) which are two nonlinear algebraic equations. Indexes N, n, q, s which are used in equations (4.23) and (4.24) can be calculated by below interchanging in the above equations:

$$M \leftrightarrow N, X \leftrightarrow Y, x \leftrightarrow y, m \leftrightarrow n, p \leftrightarrow q, r \leftrightarrow s \tag{4.25}$$

Two special cases of micro-plates, which are simple supported and fixed supported, were studied assuming the following geometry: thickness - $h = 10[\mu m]$, side - $a = 250[\mu m]$, Young modulus of Elasticity - $E = 70[GPa]$, and Poisson Ratio $\nu = 0.31$. The main purpose of this analysis was the selection of the suitable element type for ANSYS®. ANSYS® has several suitable elements, SHELL 181, SHELL 281, SOLID 185L, SOLID 185, SOLID 187, SOLID186, SOLID 186L that enable large deflection analysis and residual stress options. Table 1 shows the maximum deflection for different elements of the same plate with fixed supports subjected to a steady pressure of 2.75 MPa. This pressure was assumed given the selected size and material of the micro-plate such that non-linear deflection occurs. The element that yield identical results as the analysis was

SHELL 181. Figures 4.3.1, 4.3.2 show the maximum deflection of plate for simple support and fixed support plates in the linear and nonlinear analysis. As one can see the results of nonlinear analysis are identical for ANSYS® when SHELL 181 is selected as element type. The results of the analytical formulation have been compared with the numerical results yield by ANSYS®. For the FEM from the selected element type, one has yield identical results.

Table 4.3.1. Maximum Deflection of plate with different elements

Analytical	Shell181	Shell281	Solid185L	Solid185	Solid187	Solid186	Solid186L
2.14e-6	2.14e-6	2.57e-6	0.58e-7	0.280e-7	1.4e-6	1.45e-6	1.45e-6

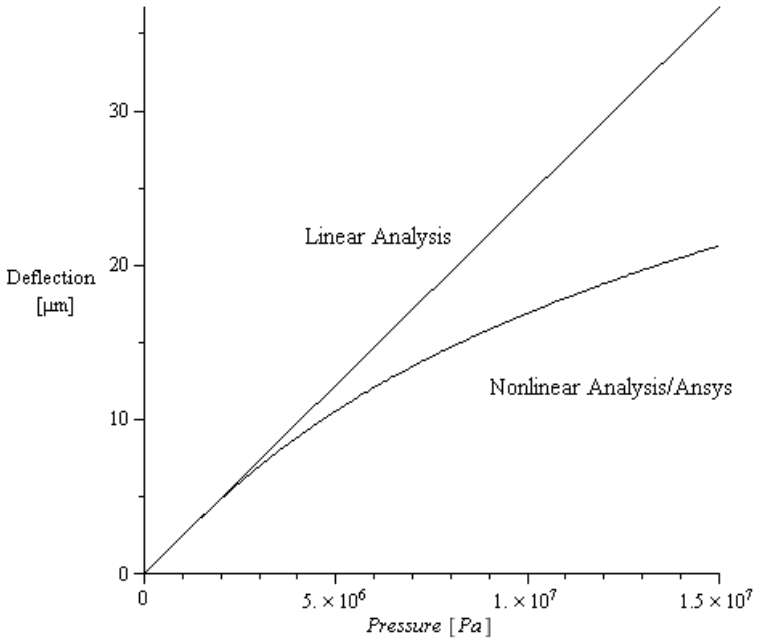

Figure 4.3.1. Linear vs. nonlinear analysis for simple support plate as defined above

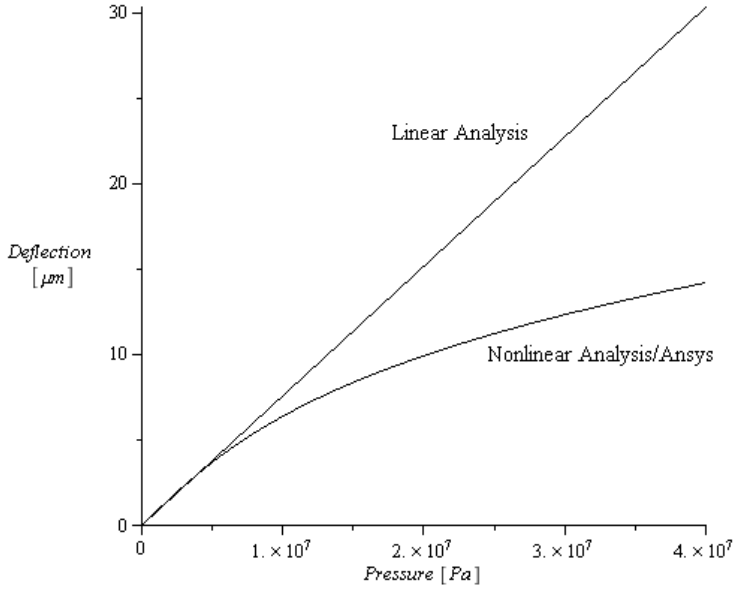

Figure 4.3.2. Linear vs. nonlinear analysis for fixed support plate as described above

4.4. Mismatch stress in composite materials with large deflection

The large deflection of laminated composite plates was widely studied [146, 165-167] . The equations of motion of the plate are [141]:

$$-\left(\frac{\partial N_{xx}}{\partial x}+\frac{\partial N_{xy}}{\partial y}\right)+I_0\frac{\partial^2 u_0}{\partial t^2}-I_1\frac{\partial^2}{\partial t^2}\left(\frac{\partial w_0}{\partial x}\right)=0 \tag{4.26}$$

$$-\left(\frac{\partial N_{xy}}{\partial x}+\frac{\partial N_{yy}}{\partial y}\right)+I_0\frac{\partial^2 v_0}{\partial t^2}-I_1\frac{\partial^2}{\partial t^2}\left(\frac{\partial w_0}{\partial y}\right)=0 \tag{4.27}$$

$$
\begin{aligned}
&-\left(\frac{\partial^2 M_{xx}}{\partial x^2}+2\frac{\partial M_{xy}}{\partial y\partial x}+\frac{\partial^2 M_{yy}}{\partial y^2}\right)-N(u_0,v_0,w_0)-q \\
&+I_0\frac{\partial^2 w_0}{\partial t^2}-I_2\frac{\partial^2}{\partial t^2}\left(\frac{\partial^2 w_0}{\partial x^2}+\frac{\partial^2 w_0}{\partial y^2}\right)+I_1\frac{\partial^2}{\partial t^2}\left(\frac{\partial u_0}{\partial x}+\frac{\partial v_0}{\partial y}\right)=0
\end{aligned}
\tag{4.28}
$$

Where:

$$
N(u_0,v_0,w_0)=\frac{\partial}{\partial x}\left(N_{xx}\frac{\partial w_0}{\partial x}+N_{xy}\frac{\partial w_0}{\partial y}\right)+\frac{\partial}{\partial y}\left(N_{xy}\frac{\partial w_0}{\partial x}+N_{yy}\frac{\partial w_0}{\partial y}\right) \tag{4.29}
$$

$$
\begin{bmatrix} I_0 \\ I_1 \\ I_2 \end{bmatrix}=\int_{-\frac{h}{2}}^{\frac{h}{2}}\begin{bmatrix} 1 \\ z \\ z^2 \end{bmatrix}\rho dz \tag{4.30}
$$

I is the mass momentum of inertia.

N_{xx}, N_{xy}, N_{yy}, M_{xx}, M_{xy}, M_{yy} are forces and moments in the cross section of plate as shown in the figure 4.4.1

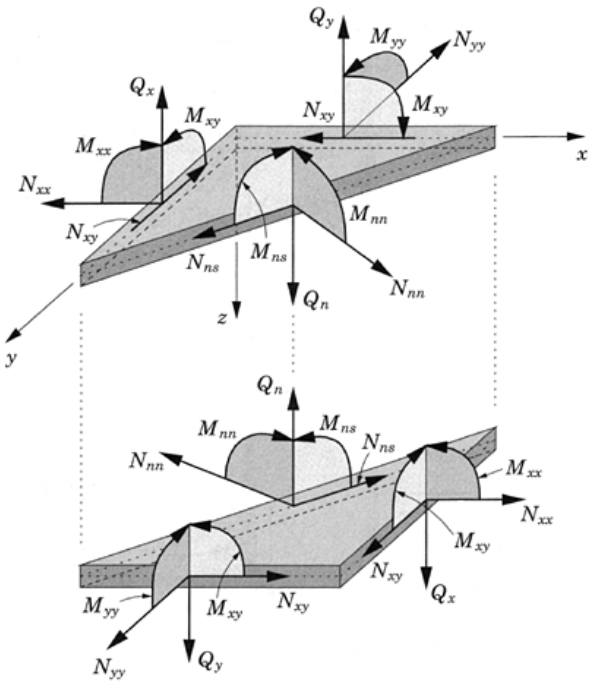

Figure 4.4. 1. Force and moment resultant on a plate element[141]

$$\begin{bmatrix} M_{xx} \\ M_{yy} \\ M_{xy} \end{bmatrix} = \begin{bmatrix} B_{11} & B_{12} & B_{16} \\ B_{12} & B_{22} & B_{26} \\ B_{16} & B_{26} & B_{66} \end{bmatrix} \begin{bmatrix} \dfrac{\partial u_0}{\partial x} + \dfrac{1}{2}\left(\dfrac{\partial w_0}{\partial x}\right)^2 \\ \dfrac{\partial v_0}{\partial y} + \dfrac{1}{2}\left(\dfrac{\partial w_0}{\partial y}\right)^2 \\ \dfrac{\partial u_0}{\partial y} + \dfrac{\partial v_0}{\partial x} + \dfrac{\partial w_0}{\partial x}\dfrac{\partial w_0}{\partial y} \end{bmatrix} + \begin{bmatrix} D_{11} & D_{12} & D_{16} \\ D_{12} & D_{22} & D_{26} \\ D_{16} & D_{26} & D_{66} \end{bmatrix} \begin{bmatrix} -\dfrac{\partial^2 w_0}{\partial x^2} \\ -\dfrac{\partial^2 w_0}{\partial y^2} \\ -2\dfrac{\partial^2 w_0}{\partial x \partial y} \end{bmatrix} \tag{4.31}$$

$$\begin{bmatrix} N_{xx} \\ N_{yy} \\ N_{xy} \end{bmatrix} = \begin{bmatrix} A_{11} & A_{12} & A_{16} \\ A_{12} & A_{22} & A_{26} \\ A_{16} & A_{26} & A_{66} \end{bmatrix} \begin{bmatrix} \frac{\partial u_0}{\partial x} + \frac{1}{2}(\frac{\partial w_0}{\partial x})^2 \\ \frac{\partial v_0}{\partial y} + \frac{1}{2}(\frac{\partial w_0}{\partial y})^2 \\ \frac{\partial u_0}{\partial y} + \frac{\partial v_0}{\partial x} + \frac{\partial w_0}{\partial x}\frac{\partial w_0}{\partial y} \end{bmatrix} + \begin{bmatrix} B_{11} & B_{12} & B_{16} \\ B_{12} & B_{22} & B_{26} \\ B_{16} & B_{26} & B_{66} \end{bmatrix} \begin{bmatrix} -\frac{\partial^2 w_0}{\partial x^2} \\ -\frac{\partial^2 w_0}{\partial y^2} \\ -2\frac{\partial^2 w_0}{\partial x \partial y} \end{bmatrix}$$

(4.32)

$[A],[B],[D]$ are the extensional stiffness, the bending-extensional coupling stiffness and the bending stiffness respectively which are defined as:

$$A_{ij} = \sum_{k=1}^{N} \overline{Q}_{ij}^{(k)} (z_{k+1} - z_k) \tag{4.33}$$

$$B_{ij} = \frac{1}{2} \sum_{k=1}^{N} \overline{Q}_{ij}^{(k)} (z_{k+1}^2 - z_k^2) \tag{4.34}$$

$$D_{ij} = \frac{1}{3} \sum_{k=1}^{N} \overline{Q}_{ij}^{(k)} (z_{k+1}^3 - z_k^3) \tag{4.35}$$

$\overline{Q}_{ij}^{(k)}$ is the lamina, stiffness. u_0, v_0, w_0 are the displacement components of midpoint of mid-plane along the (x, y, z) coordinate directions, respectively. ρ_0 is the density of the material where $q(x, y, z)$ is the distributed force.

4.5. Stoney equation

Deposition process in MEMS fabrication generally is usually performed at high temperature process. High temperature creates residual stress. The stress is determined

through a simple measurement of the curvature of the full wafer due to the thermal mismatching. Equally, the deflection at the center of the wafer with respect to the edges reveals the built-up stress in a deposited layer. Stoney equation gives the residual stress [156, 168]:

$$\sigma_f = \frac{\delta}{t}\frac{E}{1-\upsilon}\frac{T^2}{3R^2} \tag{4.36}$$

Where δ is the defection of the center of the wafer, t is the film thickness, R is the radius of the wafer, and T is the thickness of the wafer. In order to reach an acceptable result from Stoney equation, the substrate must be significantly thicker than thickness of the deposited film and Young modulus ratio of two materials must be close to one. Therefore there are serious limitations in the usage of Stoney equation. To evaluate these limitations in validity of Stoney equation, the following example is presented. A circular plate with radius of 141.047 $[\mu m]$ with Young modulus of 380 $[MPa]$ and equal thickness of wafer and deposited film, $t = T = 2.5$ $[\mu m]$, was considered. A circular plate was considered because Stoney equation was presented for circular plate. The area of plate is same as of square plate with length of 250 $[\mu m]$, which experiments were done by that. Also Young modulus of Si_3N_4 and residual stress of SiO_2, $\sigma_f = 225$ $[MPa]$ from [3] where considered for this example. One can calculate δ, the deflection at the center of the plate, from (4.36) which will result is 9.67 $[\mu m]$ whereas ANSYS® analysis, in figure 4.5, shows 0.704 $[\mu m]$. These results prove the substantial difference between the two estimates as based on Stoney assumptions, thickness of wafer should be much greater

than deposited film. Whereas, if $T = 100\ [\mu m]$ and $t = 2.5\ [\mu m]$ for above mentioned data deflection from Stoney can be calculated as $\delta = 9.6686 \times 10^{-8}[m]$. For this case, the numerical evaluation of the deflection performed with ANSYS® result is shown in Figure 4.6. So when thickness of wafer is much higher than thickness of deposited film like in this case, the error of Stony equation reduces %32. According to the cited references [164, 169], such error is acceptable. As introduced in reference [169] the error of Stoney equation can be calculated as shown below:

$$Error_{Stony} = \frac{\frac{t}{T} - (\frac{E_f}{E})(\frac{t}{T})^3}{1 + (\frac{E_f}{E})(\frac{t}{T})^3} \tag{4.37}$$

E_f is Young modulus of deposited layer. Figure 4.5.1 shows the equation (4.36). This figure is in a good correlation with the above example:

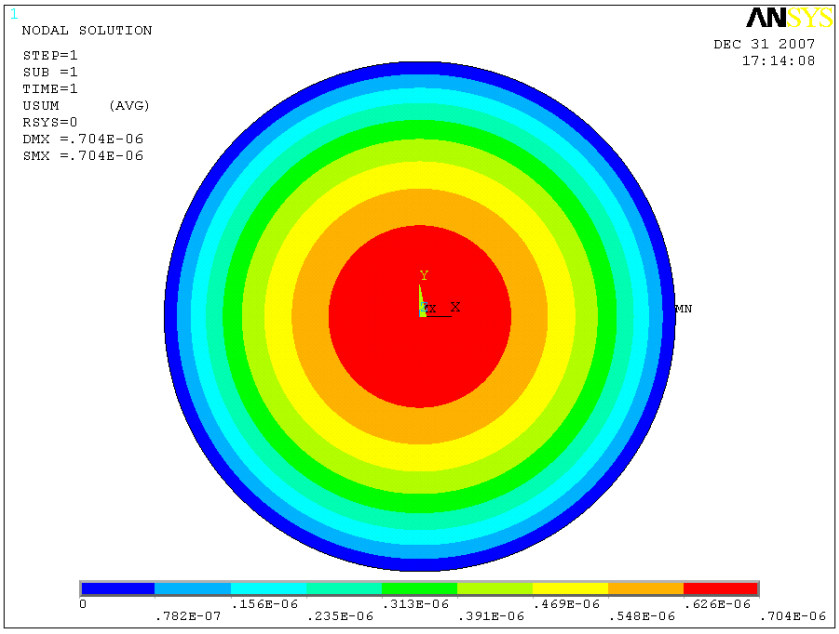

Figure 4.5.1. ANSYS result for deflection of plate, $t = T = 2.5\ [\mu m]$

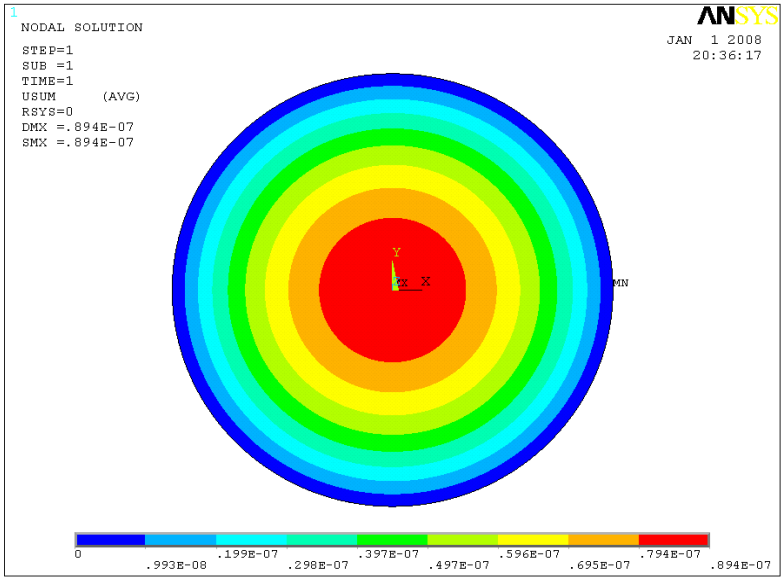

Figure 4.5.2 ANSYS result for deflection of plate, $T = 100[\mu m]$ and $t = 2.5[\mu m]$

These results show that Stoney equation cannot correctly predict residual stress when the ratio of wafer thickness to deposited layer is small [156]. One cannot make use

this equation for multilayer micro-plates that have almost equal thickness layers. Authors recommended a Stoney modified equations [145, 157, 163]. Another limitation for this equation was introduced in the above mentioned publications. The film and substrate must be attached together without any disturbance. For MEMS devices, in some cases, one cannot consider this assumption. The discontinuity of the layer with the substrate introduces stress concentration that is often uncertain. Moreover, when derive Stoney equation; one uses the linear relation between stress and strain. This assumption should be regarded with skepticism given the large stress value encountered in the inter-laminar stress sometimes much higher than the yield stress. This leads to a legitimate question: is the assumption of linearity between stress and strain standing in micro-systems?

Another issue in using Stoney equation is in measuring the curvature of the structure. This curvature is out of plane and it requires specific tools for measurement [162]. In very small features, the task is quite challenging.

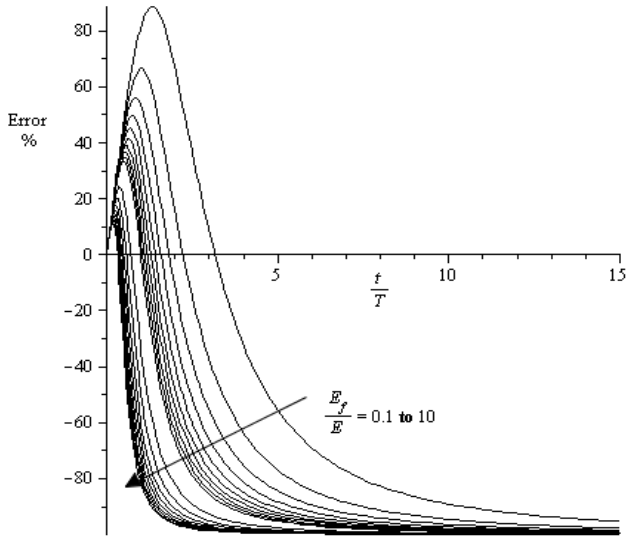

Figure 4.5.3. Error variation in Stoney equation versus film - substrate thickness and Young modulus of elasticity ratios

4.6. Difference between theory and experiments

In the part above, analytical methods in determining of small and large deflection of single layer and multilayer plates were presented. To validate the theory, a set of experiments was used. A fabricated square micro-plate with the side of 250 [μm] [3] made from four layers of different materials was used. Mechanical properties and the assumed stresses which were established based on the process parameters are shown in table 4.6.1. Although the deflection of this micro-plate is numerically evaluated by ANSYS®, the results were very much different from the ones resulting from experiments. The numerical and experimental results are illustrated in Figures 4.6.1 and 4.6.2. In this analysis, the element SHELL181 with residual stress is used.

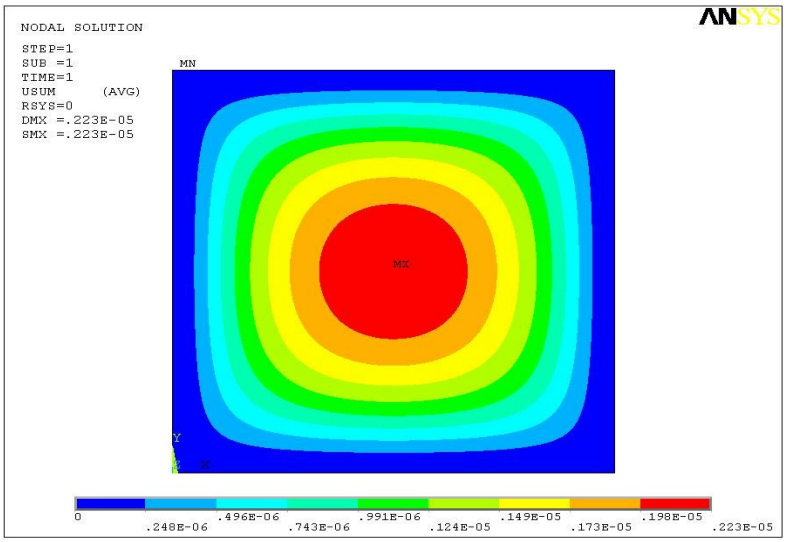

Figure 4.6.1. ANSYS analysis result for deflection of micro-plate P=2 bar

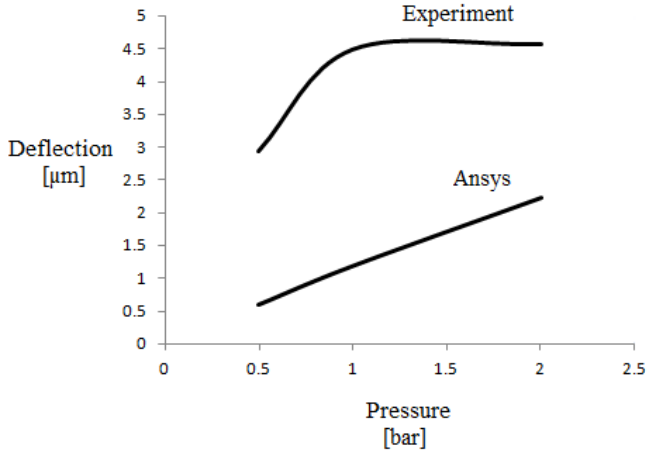

Figure 4.6.2. Pressure versus deflection of the square micro-plate 250µm side size

As seen from figure 4.6.2, there is a very significant difference between the numerical analysis and the experimental results. Meanwhile, the experimental results show a nonlinear behavior whereas the numerical results follow a linear trend.

Table 4.6.1. Mechanical properties and estimated stress in micro-plates[3]

Material	Thickness [nm]	Stress [MPa]	Young's Mod. [GPa]	Poisson ratio
Single crystal SI	100	0	165	0.25
Polysilicon	340	1000	180	0.22
Thermal Oxide (SIO2)	433	- 225	70	0.17
PECVD (SIO2)	283	-172	85	0.25
APCVD (SIO2)	560	383	69	0.17
LPCVD (SI3N4)	288	860	380	0.25
Aluminum	1000	-10	70	0.33

This significant difference provided the rational of this investigation. The source of this is difference also investigated. For this purpose, authors used the results of the following

experiment and numerical methods to validate the results of the experiments and then identify the cause of the difference. The method evaluates tore-iterate the stress values in the layers.

4.7. The experiments

It is important to mention here out the fact that the results of the measurements show also non-monotonous behavior in the deflection vs. pressure. The results have been used as collected from measurements and the variations are assumed due to instrumental error associated with the measurement method. The deflection in the experiments is measured by interferometer. The nozzle that creates pressure on the membrane, although transparent, may induce some error in measurement due to the interference of the incident and reflecting light wave through the transparent material of the nozzle (quartz). The results of the numerical simulations are compared to the measured deflection which values are assumed as reference.

4.7.1 Fabrication of the devices

To evaluate the internal stress in each layer several micro-plates were fabricated. Plates had various dimensions and number of layers. Details of manufacturing are defined in [2, 3]. Below, a brief description of manufacturing process which is a standard SOI CMOS process that includes some extra fabrication steps is presented. A <100> UNIBOND SOI wafer film and a layer of oxide is used. Two types of multi-layered are built as illustrated

in figure 4.7-1. By photolithography the active Si film is removed. A patterned LPCVD nitride film which acts as a mask for locally wet thinning the top silicon film and for the LOCOS oxidation is deposited. Another LPCVD nitride layer is deposited and patterned. A combination of SF_6 and CHF_3 based plasmas is used for etching. Wafers follow the process of gate oxidation, channel implantation, poly-silicon gate deposition and patterning. Figure 4.7.1 Shows, schematics of the measurement system for the deflection of the plate subjected to steady pressure. The laser interferometer, measures, with a sensitivity of 10 [nm], the deflection of the multiple layered plate at the centers. The pressure reading is correlated to the deflection.

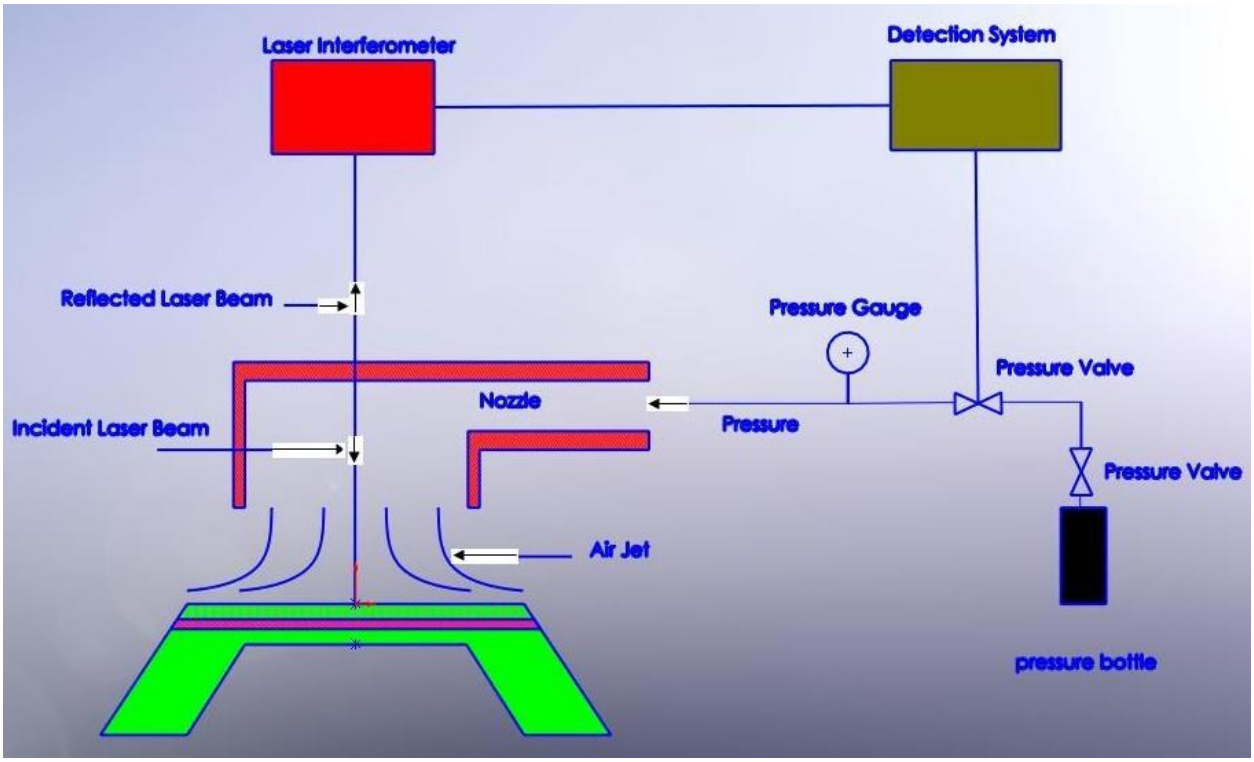

Figure 4.7.1. Schematics of the measurement system for deflection of the plate

4.7.2. Mechanical behavior of the membrane under uniform distributed load

Mechanical properties and the estimated internal stress in each layer are presented in table 4.7-1 The method of calculation of the residual stress is in detail provided in [2]. When a process is preformed a layer is grown and the stress is measured by the curvature of the wafer, by Stoney equation. All layers deposited with same process are assumed to have developing the same predetermined internal laminar stress. Two types of membranes have been studied: 3-layers and 4-layers, as are shown in Figure 4.7-2where the thickness of each layer is indicated. The experimental values of the deflections of plates are given in Figures 4.7-3 and 4.7-4, and the numerical values of deflection at specific pressures are provided in tables 4.7-2 and 4.7-3

Table 4.5. Mechanical property and internal stress of each layer[3]

Material	Stress (MPa)	Young's Mod. (GPa)	Poisson ratio
SiO_2 (Thermal)	-225	70	0.17
SiO_2 PECVD	-172	85	0.25
SiO_2 APCVD	383	69	0.17
Si_3N_4 LPCVD	860	380	0.25

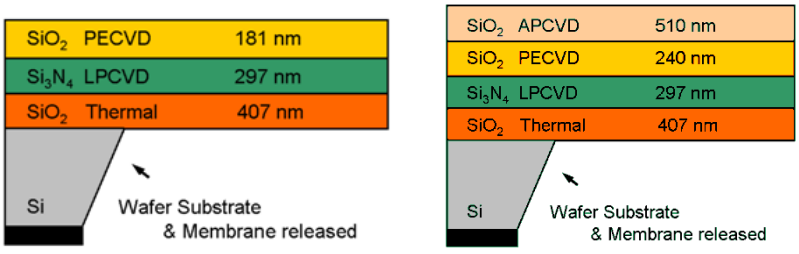

Figure.4.7.2 The two different types of plates [2]

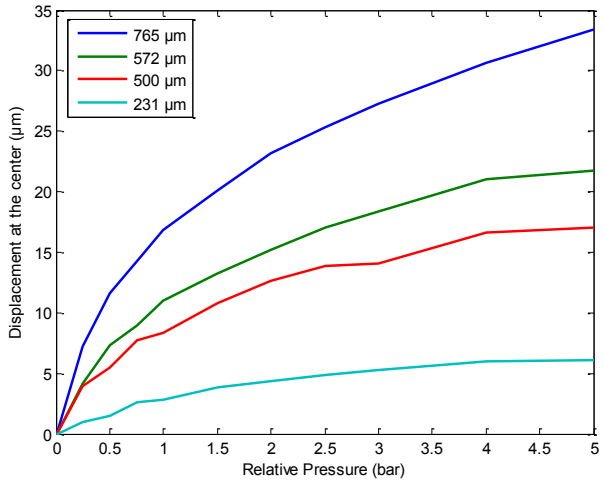

Figure 4.5.3. Experimental results for deflection of 3-layer plates under uniform pressure [2]

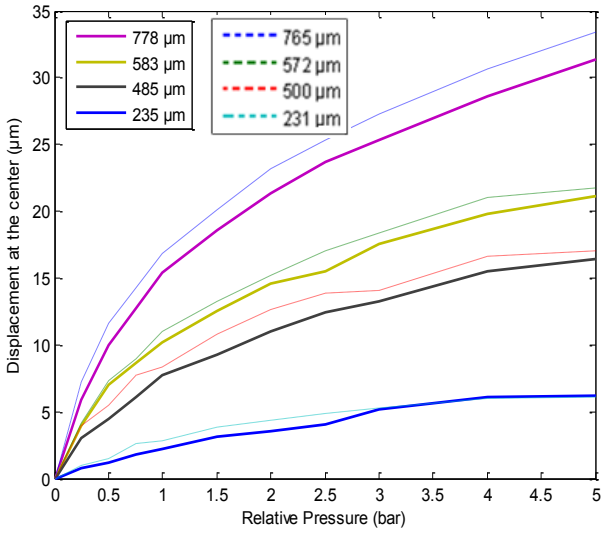

Figure 4.7.4. Experimental results for deflection of 4-layer plates under uniform pressure(dashed lines represent the deflection of the 3-layers membranes deflection) [2]

Table 4.52. Deflection of 3-layer plates at specific values of the pressure [2]

pressure (bar)	0.25	0.5	0.75	1	1.5	2	2.5	3	4	5
size (μm)	Deflection at the center of the membrane (micrometers) ↓									
778	5.88	10.01	12.77	15.39	18.6	21.32	23.67	25.35	28.63	31.33
583	3.96	6.98	8.69	10.22	12.51	14.59	15.52	17.52	19.79	21.11
485	3.05	4.47	6.1	7.69	9.23	10.97	12.43	13.29	15.51	16.4
235	0.8	1.17	1.8	2.16	3.14	3.56	4.09	5.15	6.04	6.17

Table 4.5. Deflection of 4-layer plates under pressure [2]

pressure(bar)	0.25	0.5	0.75	1	1.5	2	2.5	3	4	5
size (μm)	Deflection at the center of the membrane (micrometers) ↓									
765	7.26	11.63	14.25	16.83	20.09	23.18	25.28	27.28	30.62	33.43
572	4.14	7.32	8.94	10.99	13.21	15.24	17.03	18.34	20.98	21.75
500	3.89	5.48	7.69	8.37	10.76	12.66	13.84	14.04	16.64	17.07
231	0.95	1.5	2.64	2.81	3.82	4.34	4.88	5.22	5.97	6.06

4.8. The numerical analysis

A series of analysis algorithms are developed to run simulations by ANSYS. A code was developed to evaluate strain analysis on a plate made from several uniform thickness layers. The element SHELL 181 was used in this analysis. The below graphs, Figures 4.8-1 to 4.8-8, illustrate the differences between the experimental results and the numerical analysis performed by ANSYS. The highlight of the analysis is given below.

a) In all cases, numerical results yield deflection values below the experiments. This is due to the stiffness of the SHELL 181 elements which is overestimated.

b) In most cases the error decreases by increasing the pressure. The route of the error encountered for deflection measurements with pressure varying from 0 to 5 bar decreases with the increase in size of the plates.

c) In all cases the experimented and the analytical results exhibit nonlinear behavior. However, the numerical method yields monotonous results with regards to the pressure.

d) The gradual increase in pressure yields an increase in the deflection this means that pressure is related by deflection through a continuum function.

e) The error recorded between numerical and experimental values is non-monotonous.

f) By increasing the dimensions the average error reduces.

g) 3 layer configurations yield less error route than 4 layer configuration.

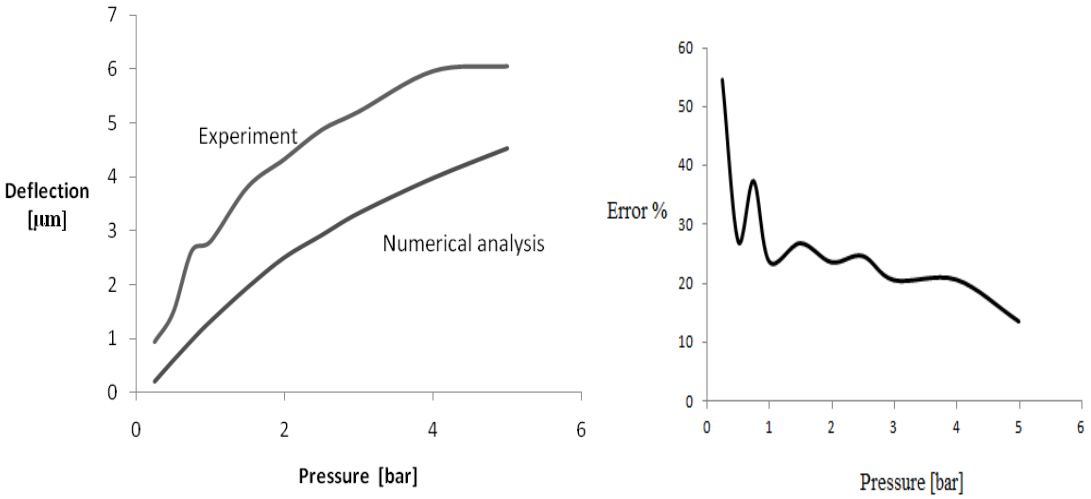

Figure 4.8.1. Experimental versus numerical deflection and error of numerical value with respect to experiments for 3 layers plate 231µm×231µm

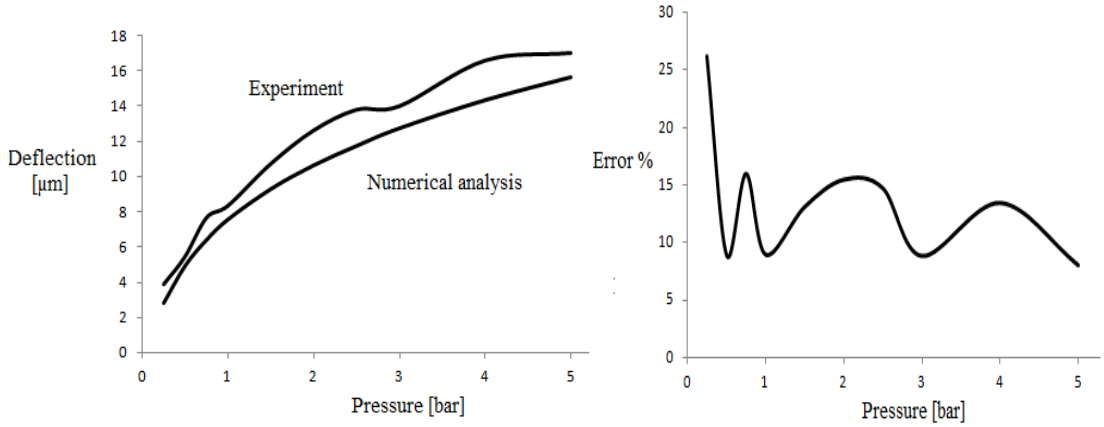

Figure 4.8.2. Experimental versus, numerical deflection and error of numerical respect to experiments for 3 layers 500µm ×500µm plate

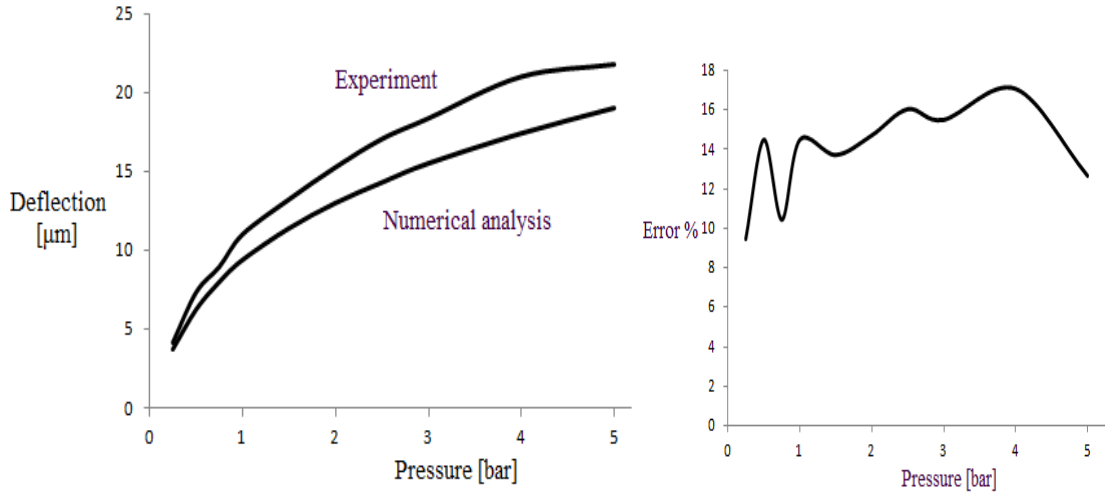

Figure 4.8.3. Experimental, numerical deflection and error of numerical respect to experiments for 3 layers 572μm ×572μm plate

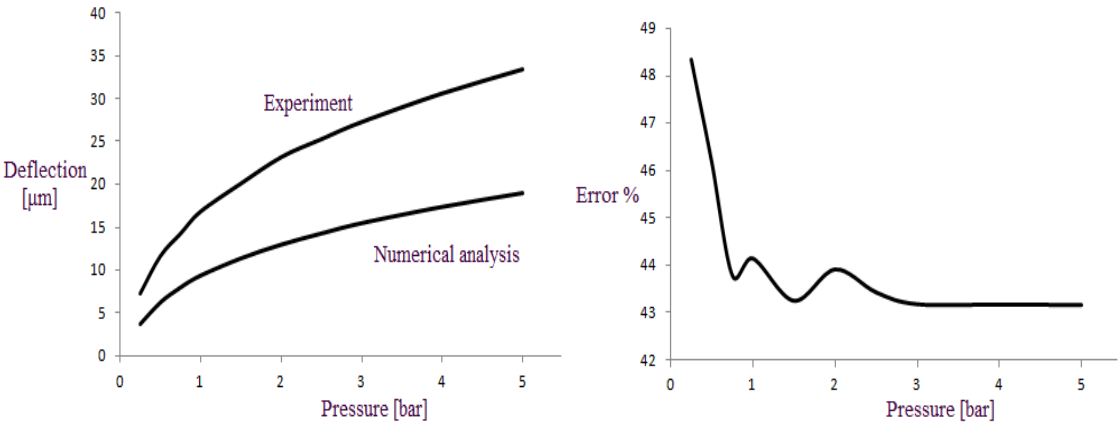

Figure 4.8.4. Experimental, numerical deflection and error of numerical respect to experiments for 3 layers 765μm×765μm plate

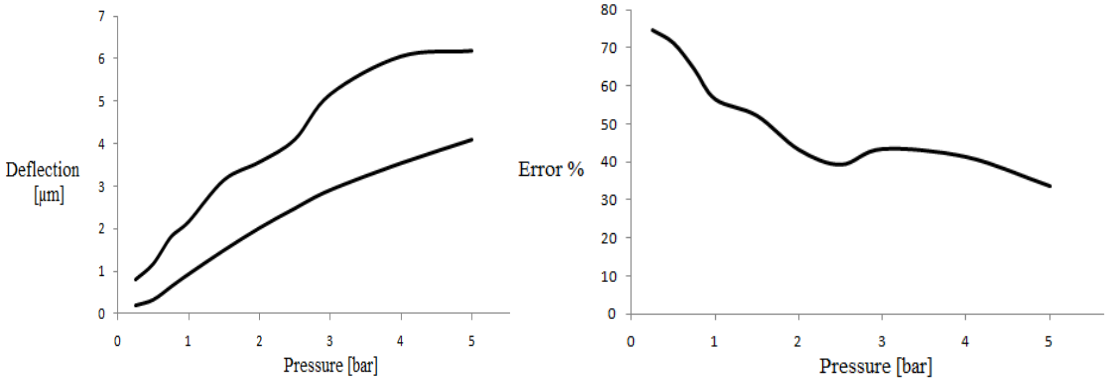

Figure 4.8.5. Experimental, numerical deflection and error of numerical respect to experiments for 4 layers 235µm×235µm plate

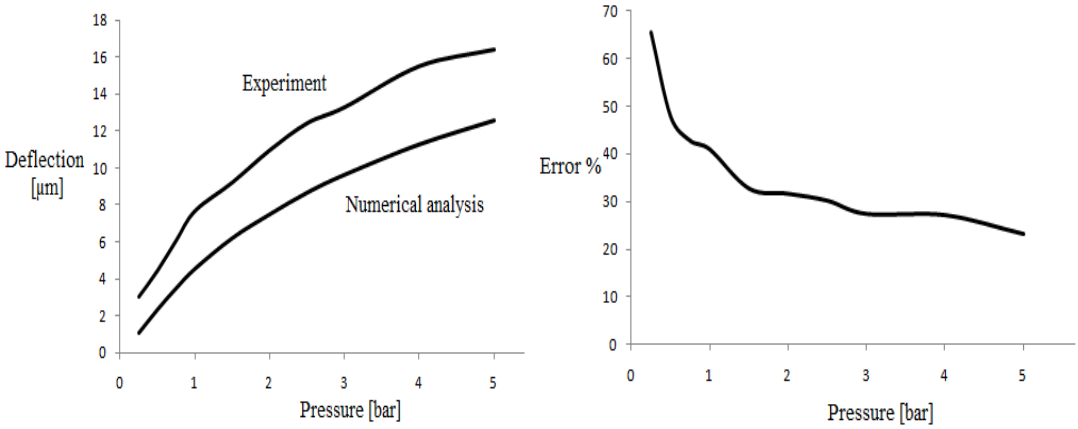

Figure 4.8.6. Experimental, numerical deflection and error of numerical respect to experiments for 4 layers 485µm×485µm plate

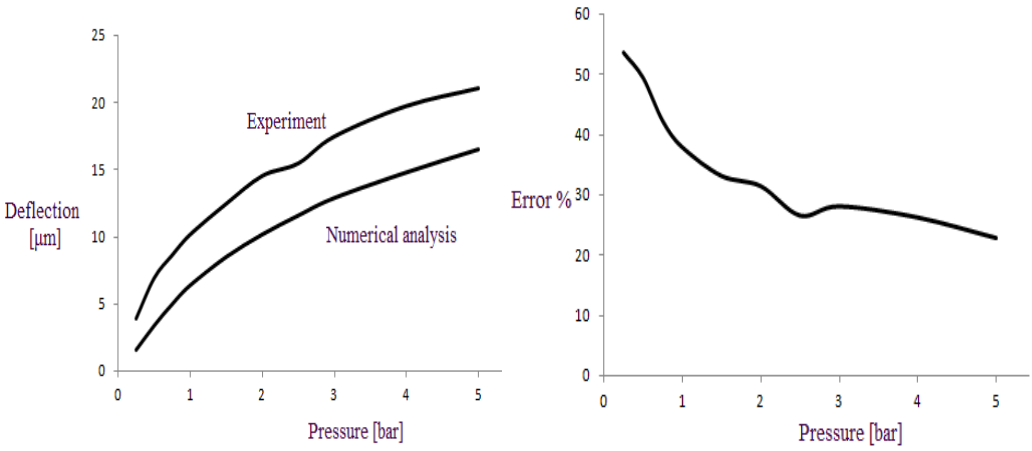

Figure 4.8.7. Experimental, numerical value of the deflection and the error of numerical solution with respect to the experiments for 4 layers 583µm×583µm plate

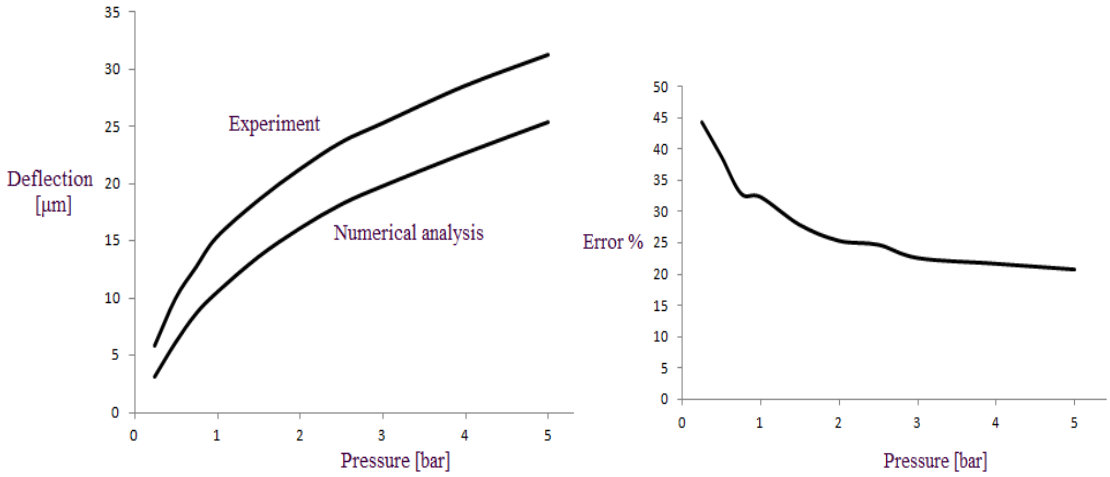

Figure 4.8.8. Experimental, numerical deflection and error of numerical respect to experiments for 4 layers 778µm × 778µm plate

The source of the error is assumed to be related to the unrealistic values of the stress in the structural layers. If assume that the error in estimating the stress is within the range of the error encountered when Stoney equation is used, the potential variation of the stress within these limits may yield an accurate estimate. The problem becomes now an optimization and the gradient-descent like algorithm for three or four variables. A formulation is implemented to numerically evaluate the stress that yields a good matching of the experiments with numerical simulation using ANSYS.

The optimization method requires proving that the continuous variation of the stress in the layers produces continuous variation in the deflection of the composite made membrane. For 3 layers micro-plates, it is shown that continuous relation is established between the inter-laminar stress and deflection. For this purpose, a numerical analysis was accomplished for all 3 layers plates by considering this fact that Stoney equation yields up to 40% error [163]. A set of different stress values in layers is applied in the plates and deflections were computed. The stresses are assumed to vary within 60%-to140% from the one estimated initially for every layer. The results are shown in figures 4.8-1 to 4.8-8. As one can see from these plots and governed equation for stress, equation

(4.26) to (4.28), there is no discontinuity in graphs and no pole in equations. In the other words, the deflection does not come discontinued despite the fact that the stress is varied in figure below from 60% to 140%, the deflection covers a continuous domain which is represented by the thick gray line. If one checks 4 layers plates, similar results will be found. In order to avoid repeating the similar plots, in the below chapter the results for four layer composite plate are not illustrated. However, the results are quite similar as the ones for three layer configurations.

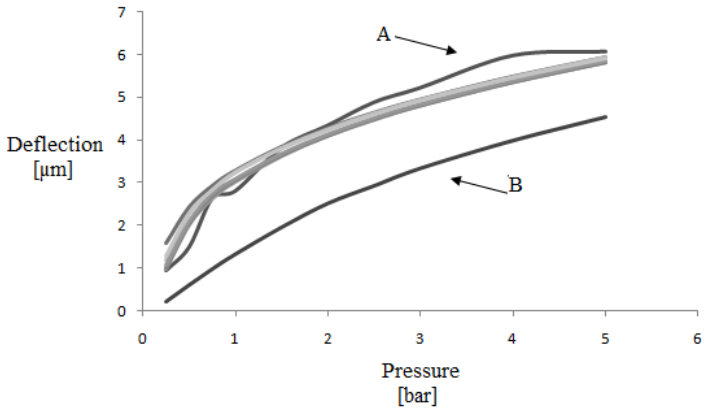

Figure 4.8.9. Plate with 3 layers, 231µm×231µm, 10 different stresses distribution in layers (A: experiment as in table 4.4-1B: 60%-140%-60% stresses of Stoney equation in each layer respectively)

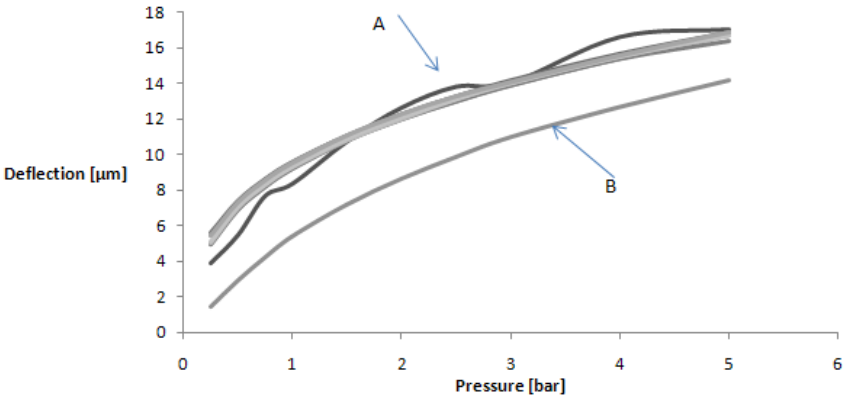

Figure 4.8.10. Plate with 3 layers, 500µm ×500µm, 10 different stresses distribution in layers(A: experiment as in table4.4-1, B: 60%-140%-60% stresses of Stoney equation in each layer respectively)

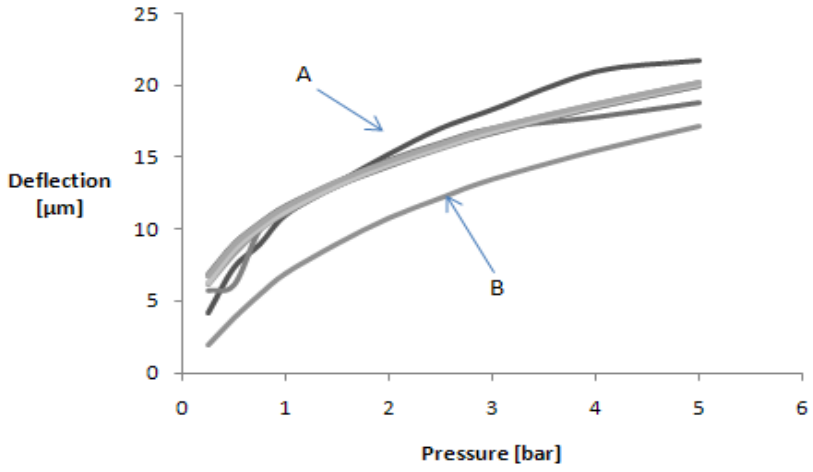

Figure 4.8.11. Plate with 3 layers, 572µm ×572µm, 10 different stresses distribution in layers(A: experiment, B: 60%-140%-60% stresses of Stoney equation in each layer respectively)

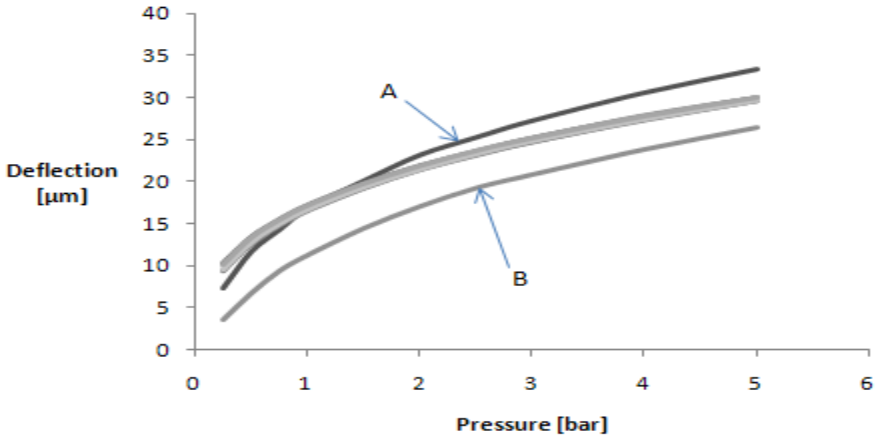

Figure 4.8.12. Plate with 3 layers, 765µm ×765µm, 10 different stresses distribution in layers (A: experiment, B: 60%-140%-60% stresses of Stoney equation in each layer respectively)

4.9. The optimization technique

The governing equations for the multilayer micro-plate with residual stress were presented in section 4.4 followed by the equations (4.26)-(4.28) give the large deflection of plates of multilayer configurations with residual stress. As showed in the previous

section, the deflection of the micro-plates follows a continuous function with regards to the inter-laminar stress. Because the micro-plate experiences large deflection which is a nonlinear phenomenon, the governed equations, (4.26) to (4.28), are selected as nonlinear. The exact value of stress in each layer is sought through a nonlinear optimization technique that has an objective minimization of the error between the experimental and analytical computed deflection of the multi-layered micro-plate for various pressure values varying from 0 to 5 [bar]. Nonlinear optimization gets faster convergence compare to linear optimization. By considering that in each step of this optimization for each point several times must run ANSYS®, so one can see that fast convergence is essential. In general, the problem formulation is as in [170]:

Let $(X, \|.\|)$ be a real normed space; let S be a nonempty subset of X; and let $f: S \to \Re$ be a given functional. Under this assumption, we investigate the optimization problem $\min_{x \in S} f(x)$. One can prove the below theorem [170]:

Let S be a nonempty convex subset of a real normed space. Every local minimal point of a convex functional $f: S \to \Re$ is also a minimal point of f on S.

By considering analyses which were carried out in the previous sections and the above theorem, one can conclude that the problem to find an optimum stress distribution in layers is possible. As mentioned before the stress is continuous function in the normed space, and also a real numbers $\Re$. Also for this case the objective function f is expressed as the square error, $MSE(\hat{\Theta})$ between the calculated and the measured values of the deflection at the center of the micro-plate. This function is minimized. Stress in each layer was considered in the range 140% to 60% of Stoney equation and these were

constrain equations for optimization problem. It means that the interval of residual stress variation for each layer was considered as below:

$$-225\times 0.6=-153\ [MPa]\le \sigma_{1^{et}\ layer}\le -225\times 1.4=-315\ [MPa]$$

$$-172\times 0.6=-103.2\ [MPa]\le \sigma_{2^{ed}\ layer}\le -172\times 1.4=-240.8\ [MPa]$$

$$860\times 0.6=516\ [MPa]\le \sigma_{3^{ed}\ layer}\le 860\times 1.4=1204\ [MPa]$$

The applied pressure represents a constraint equation. The analysis was run using ANSYS. For each case the error function is computed. The minimum one was selected from the error functions which is further used to decide what iteration if further performed by the FEA program. Pressure values are: 0.25, 0.5, 0.75, 1.0, 1.5, 2.0, 2.5, 3.0, 4.0 and 5.0 [bar] respectively. In the code, for a specific dimension, first assumed that pressure is 0.25 [bar] then for first layer $\sigma_{1^{et}\ layer}=-153\ [bar]$ assumed as residual stress also for second layer and third layer residual stress was considered $\sigma_{2^{ed}\ layer}=-103.2\ [MPa]$, $\sigma_{3^{ed}\ layer}=516\ [MPa]$ respectively. Then ANSYS® calculated deflection for this case. The error from the experimental for $P=0.25\ [bar]$, $\sigma_{1^{et}\ layer}=-225\ [bar]$, $\sigma_{2^{ed}\ layer}=-72\ [MPa]$, $\sigma_{3^{ed}\ layer}=860\ [MPa]$ was calculated. Then $P=0.5\ [bar]$ was considered without changing the residual stresses and the deflection and the error were derived. Further, the deflection corresponding to the max pressure was calculated and the corresponding error was found. After that $MSE(\hat{\Theta})$ was calculated for all pressures. In the second step for $P=0.25\ [bar]$ was assumed and the residual stresses in first and second layers was left unchanged while the residual stress in third layer was increased 1% this is $\sigma_{3^{ed}\ layer}=521.1\ [MPa]$, and all procedure repeated again and another

$MSE(\hat{\Theta})$ calculated. When the error reduces, the change follows the same trend. This algorithm repeated till the smallest value of the $MSE(\hat{\Theta})$ is found for a combination of residual stress in layers for all pressures. To complete comprehensive analysis for a plate one may need for more than five million times of running ANSYS® which means significant amount of time. Even if the solution may lead a local optimum, it is thought that the error which has reached 0.385% is considered more acceptable than running such a huge number of simulations to cover the entire range of possibilities. At the end, minimum value of $MSE(\hat{\Theta})$ was selected as an optimum value that reduces the error between experiments and numerical analysis. For example for plate 231μm×231μm, minimum $MSE(\hat{\Theta})$ happens when the residual stress in first layer is 135% of Stoney equation, $\sigma_{1^{st}\,layer} = -255\ [MPa]$ and second and third layers stresses are %72 and 63%, $\sigma_{2^{nd}\,layer} = -124\ [MPa]$, $\sigma_{3^{rd}\,layer} = 542\ [MPa]$ of Stoney equation respectively, as shown in figure 4-9.1.

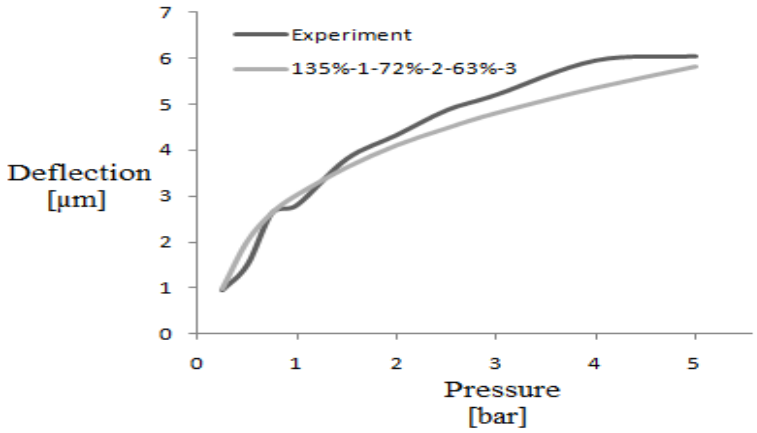

Figure 4.9.1. Optimized stress distribution in 3-layer micro-plate, 231μm×231μm, in the first layer 135% in the second layer 72% and in the third layer 63% of Stoney equation estimated are in the layers.

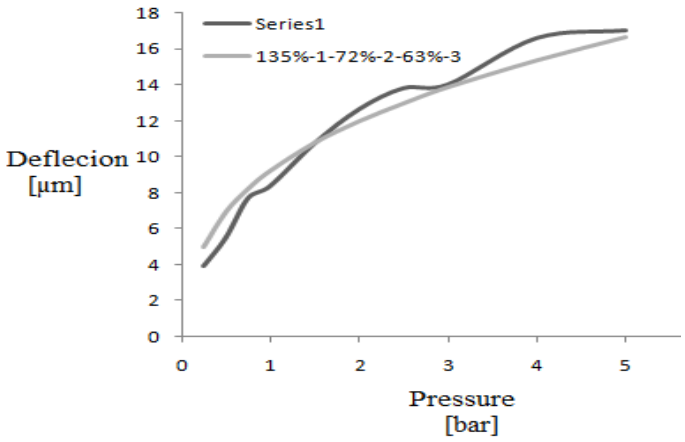

Figure 4.8. Optimized stress distribution in 3-layer micro-plate, 500µm×500µm, in the first layer 135% in the second layer 72% and in the third layer 63% of Stoney equation estimated are in the layers.

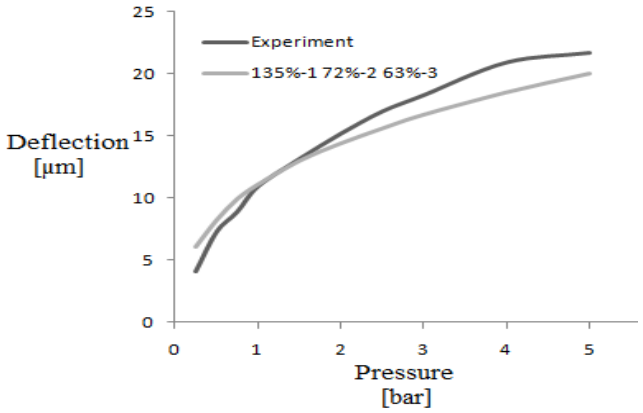

Figure 4.8. Optimized stress distribution in 3-layer micro-plate, 572µm×572µm, in the first layer 135% in the second layer 72% and in the third layer 63% of Stoney equation estimated are in the layers.

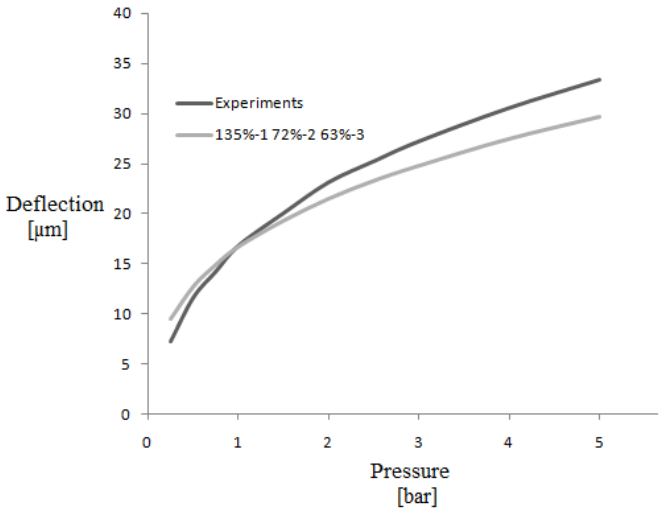

Figure 4.9.5. Optimized stress distribution in 3-layer micro-plate, 765µm×765µm, in the first layer, 135% in the second layer 72% and in the third layer 63% of Stoney equation estimated are in the layers.

As one can observe from figures 4.9-1 to 4.9-4, the residual stress distributions in layers are for from Stoney equation predicted values. In two layers stress is less than predicted values and in one layer is more than it is. Based on the experiments done in [2, 3], stresses in layers are as table 4.7-1, whereas optimization method shows that the stresses are as table 4.9-1:

Table 4.8. Stress distribution in 3 layer micro-plate

Material	Stress (MPa) (Stoney Eq.)	Stress (MPa) (optimized)
SiO2 (Thermal)	-225	-304
SiO2 PECVD	-172	-108
Si3N4 LPCVD	860	620

4.10. Summary

In practical application involving fabrication of micro-structures of multi-laminar films is essential to prior know the value of the stress developed in each layer. These values are in general terms well known. However, the effective values may vary as much as ± 40%

with respect to the generic values. The design of the geometry of a micro-structure is strongly dependent on the built-in stress in the constitutive layers. The more accurate this information is more accurate prediction of the mechanical or elastic properties could be performed. The classical linear theory of the in-layer stress by Stoney proves to be substantially off the experimental values. As the experimental measurement are assumed as the gold standard, the present investigation proposes an extraction algorithm for the values of the inter-laminar stress based on the reduction of the error between the experimental static deflection vs. the calculated value. The base-line of the analysis is the stress generic values yield by the features of the process. Based on the analytical formulation of the problem, a solution that involved Kirchhoff assumptions is proposed. A finite element analysis for a generic size of micro-plate using multiple element types shows that SHELL 181 yields the closest values of deflection if compared to the analytical solution found by series expansion. Thus, this type of element is further used in the extraction algorithm. The deflection is established for the base line and again, for extreme variations of the stress in the structural films: 60% and 140%. The gradient method is further used to evaluate the direction of increasing the stress by 5% in the layers that yield the highest sensitivity. When the gradient on the RMS error increases, the revising calculations are performed with increments of 1%. The process is followed as long as convergence is attained. In this paper, the results for square micro plates made of 3 and 4 layers of four different geometric sizes are analyzed. The method enables fine-tuning of the resonant properties of microstructures as well.

Chapter 5

Conclusion and Future Work

5.1. Conclusion

This thesis focuses on analytical analysis of nonlinear behavior of MEMS devices. MEMS structures show nonlinear behavior, due to the physics at small scale, manufacturing process and the properties of materials in thin films. These phenomena do not usually come into picture at large scale.

The theory of beams and plates has been well defined in the past and the assumptions used in these theories have been used in the analysis of microstructures just because other available theories were not handy. As the fundamental theories make use of simplifying assumptions accepted in the classical theory given the specific application of the respective structure, in MEMS such assumption are not reasonable anymore.

The deflection of a macro-cantilever beam in construction structures or in vehicle applications is not affected by any electrostatic field, whereas this phenomenon is common in MEMS. If the potential difference between substrate and micro-cantilever beam increases, the beam will collapse. The event occurs when the potential difference reaches pull-in voltage inducing static instability. Linear analysis of pull-in voltage shows that the beam will collapse if deflection reaches 1/3 of the initial distance between beam

and substrate. These results do agree with nonlinear analysis which was carried out in this investigation. It has been shown that the critical distance is 4/9 of the original distance. The behavior of micro-cantilever beam was studied under the voltage very close to pull-in voltage. Experimental result with direct measurements is not feasible for this phenomenon. Indirect measurements were performed at potentials large enough but not close to the pull-in. The deflection of the beams modeled through the non-linear assumptions better suits the experimental results that the linear assumptions.

Analytical solution of differential equation by Lie symmetry groups preserved the nonlinear terms for pull-in voltage formulation. This term relates the pull-in voltage, the gap between micro-cantilever beam and substrate to pull-in distance independently of beam geometry.

Micro-cantilever beam as a probe in AFM has a crucial role. Using a curved manufactured beam may significantly affect the sensitivity of the probe. If micro-cantilever beam experiences a large deflection during an experiment, the sensitivity of AFM will change. To answer these questions, the governing differential equation of non-straight beam under the point force tip which creates large deflection was derived and solved by Lie symmetry groups. The analytical solution was compared with the straight beam in the large deflection subjected to the same force. The results showed that there was no difference between the two solutions. Also sensitivity analysis was carried out for all the possible parameters and the effect of each such parameter was investigated for several cases.

Pressure sensors are largely used in industrial applications. One type of pressure sensors is micro-plate sensors. To manufacture this type of sensors, different materials are deposited on the substrate. Deposition of each layer builds up residual stress between

layers. Stoney derived a simple equation for evaluation of the residual stress in 1907. Only recently the equation has been used. In this thesis, it was shown that this equation will not predict correctly the values for stress in layers. A numerical optimization method was presented to calculate correct values of residual stress in three and four layers laminate micro-plates. The experimental results have been used to optimize the values of the laminar stress such that deflection matches the experimental data.

5.2. Lie Symmetry Group Method

Sophus Lie found in nineteenth century that most of the methods for solving differential equations are using group theory. Lie symmetry methods are central to the modern approach for solving nonlinear differential equations.

The main idea came from symmetry in geometry. In smooth manifold a differential equation relates its elements to another smooth manifold similar as in mapping process. An infinitesimal transformation which is invariant of the differential equation does not change the form of differential equation. The infinitesimal transformation makes a symmetric group that is also Lie group. This group transfers the differential equation from main domain to a new manifold which is tangent bundle. The manifold is called canonical coordinates. By this transformation the order of original differential equation reduces one degree and if it is first order differential equation it will be separable. The reduction order process can continue until it reaches a first order differential equation. All this process is possible if the invariant transformation is available. In this investigation, although three different approaches of Lie symmetry were presented, just one type of invariant that includes scaling and rotating was studied.

5.3. Nonlinear vibration of micro-cantilever beams under electrostatic field

Nonlinear vibration of micro-cantilever beam under electrostatics field was studied. The governing ordinary differential equation (ODE) was derived by using the energy method. The equation was taken into account as second order nonlinear ODE. It was shown that the equation is invariant under the scaling transforming. The transformation of the second order differential equation produced a first order ODE. The new ODE is nonlinear and so far, there is no invariant for this ODE to yield a close form solution. The first order ODE has a term which is dependent on the pull-in voltage. This term also makes the ODE nonlinear. Neglecting this term makes the ODE solvable, but the solution excludes the damping parameter.

Numerical solution of second order ODE, is another issue that was studied in the present investigation. It was shown that all the solutions that used Maple included algorithms, except one, are not suitable to solve this ODE. The only method that can be used is *lsod* algorithm. This method is used for stiff ODE's.

As most the of numerical methods fail in solving the nonlinear ODE, the objective of finding an analytical solution to this problem is a natural intention.

Pull-in voltage is an important subjected that was widely studied. This is the reason for which the subject was also investigated in this research. Although this phenomenon was studied in many articles, most of them solved the linearized ODE. In the present investigation it has been shown that using linearized solution yields to different output than the one obtained from nonlinear solution. Several models of pull-in voltage which were introduced in the open literature were addressed in this research. Nonlinear solution of the models was compared with the linear models solutions and also with the experimental results. It was proved that linear models yield solutions that are far from the

experimental results. Moreover nonlinear models would not match with experimental results within the recommended range of the papers. For seven types of models the pull-in voltage the behavior of system close to pull-in voltage was analyzed including the stability of system, large deflection of cantilever and resonance frequency. The results of the analysis were studied and compared with experiments which the results were fit experiments. Similar behavior is expected to be resulting from exposure of micro-systems to other field forces.

5.4. Large deflection of micro-cantilever beams

Analytical analysis of large defection of beam has more than sixty years of history. Many kinds of forces, supports, analytical methods and numerical methods have been investigated. Advent of MEMS and also the successful manufacturing of the micro-cantilever beam leads to the importance of beam large deflection analysis. Most of the microstructures including cantilever beams experience large deflections. The governing equation of large deflection for a beam under any kind of loading is represented by a second orders nonlinear ODE.

In the third chapter of this thesis, a general solution for large deflection of beams is analyzed. The applications of the method are for beams under any kind of load and any type of material. A general solution was derived for beams of arbitrary cross section using Lie symmetry groups. By this solution, an explicit formulation was derived for the first time for a cantilever beam under a point force at the tip. The result was compared with those obtained from the implicit solution. Three cases were selected from the open literature and they were examined through the presented solution as well as by numerical

methods. Method of deriving small deflection from large deflection was validated from the general solution. All derived relations were valid at the micro level.

One of the problems that researchers are facing when analyzing micro-cantilevers beams is to calculate the residual stress in such beams with large deflections. To overcome this problem, a semi-analytical formula based on Taylor expansion was presented and validated.

Another application for large deflection of micro-cantilevers is in AFM. In AFM normally, micro-cantilever beams are straight and they are subject to small deflections. However, the fabrication process effort of the AFM would be significantly reduced if non-straight beams would be used as probes. Moreover, the beams could be subjected to large deflections under specific tapping mode conditions. For an originally curved beam under large deflection, the governing ODE was derived and solved by Lie symmetry method. It was shown that curved beam had the same deflection as straight beam of the same geometry and material in large deflection. The sensitivity of beam was investigated with respect to the geometric parameters of the beam and the material for various loading conditions including tip force of variable angle. It was proved that the sensitivity with respect to the intensity of the load reduces in large deflection when compared with large deflection beams.

5.5. Large deflection of multi-layered micro-plates

As mentioned above, micro-plates have a wide range of applications in industry. In this thesis, the governing equations for single layer and multilayer plates with large deflection

were presented. A series of micro-plates with three and four constitutive layers were modeled in the present investigation. The micro-plates were manufactured and tested by a collaborator of Concave Research Centre. The experimental results for the deflection of the plates under the assumed values of the inter-laminar stress showed very large abatement from the numerical results obtained from the numerical simulation carried out with ANSYS. All these stresses were taken into account while a uniform pressure was assumed to act on the micro-plate. The experimental value of the maximum deflection was compared with the peak deflection resulting from the numerical computation. In calculating the residual stress in layers, Stoney equation was used whereas it was proved that the equation can yield up to 40% error. Based on this fact, the effective value of the stress in each layer was found using a numerical optimization method in conjunction with ANSYS. In each micro-plate the corresponding deflection for a uniform known pressure were measured and recorded. An optimization algorithm was presented to determine the stress values in each layer such that they range within ±40% of Stoney predicted stress, some constrains were applied to reduce number of iterations . The objective function was set as to minimize the error of the deflection vs. pressure with respect to experimental deflection within the given experimental range. The results showed that there are residual stresses in all micro-plates in the predicted range in the way that deflection by numerical analysis is very close to the experimental results. Also it was shown that for all different dimensions of micro-plates with the same number of layers the calculated residual stresses are same. It was shown that in three layer plate real residual stress in layers are 135% of initially assumed stress in the first layer, 72% in the second layer and 63% in the third layer. The values are specific for the fabrication process.

5.6. Future recommended work

Nonlinear analysis is important in MEMS accurate modeling. A basic fundamental theory is missing and the reason of this absence is obvious. The nonlinear theories are difficult to apprehend and they represent a step away from the reasoning of engineering which aims simplified theories. However, when linearizing differential equations in micro-systems modeling, that operation should be carried with caution. For this reason, it seems reasonable that for all MEMS applications one should perform analysis solving the nonlinear differential equations. To extend the objectives of this thesis, author has formulated few suggestions for the future work.

In classical theory of the mechanics of materials it is undisputed that a beam would deflect within a linear domain, this is a fraction of its thickness. In microstructures the deflection of a beam might exceed few hundred times the thickness of the beam and despite the deflection range, the beam resumes its original position when the exciting load is removed. It is clear from here that despite the large strain the stress has not exceed the yield value for the material of the micro-beam. A paradox in the physics of micro-systems is thus re-formulated as previously stated in the thesis; the relation between stress and strain at micro-level is non-linear. Based on this justification the future investigations should be directed towards:

1. Deriving complete solution for first order ODE in vibration of micro-cantilever beam by Lie symmetry. This requires finding some type of other symmetry of the equation rather than rotation or translation. An analytical solution will enable a direct design of microstructures which operate in electric fields.
2. Deriving an analytical formulation for stability of micro-cantilever beam. This will help to predict the stability of system without any need to numerical solution.

3. Deriving an analytical formulation for pull-in voltage with nonlinear analysis. Still there is no analytical value for pull-in voltage. This will give exact value for pull-in voltage and there will be no need to solve a stiff ODE or PDE to get approximate solution. Also it helps to design the micro-cantilever in way that to avoid pull-in. This can be done by finding an analytical solution by Lie symmetry method to first order ODE.
4. Solving the large deflection of micro-beam with PDE by Lie group. For this purpose , the algorithm of finding symmetries of PDE and method of solving the PDE by Lie symmetry should studied carefully.
5. Finding the physical meaning for nonlinear terms of reduced form of ODE. This may can be done by understanding the physical meaning of infinitesimal transformation and physical meaning of canonical coordinates and transferred equations. It need to deep understanding of Manifold and Lie groups and their physical properties.
6. Deriving an explicit solution for large deflection of curved beam. It may be possible to follow the presented method for large deflection of beam in current work.
7. Solving the PDE of large deflection of micro-plate by Lie symmetry method. It can be done as mentioned for PDE of large deflection of beam.
8. Deriving analytical formula for residual stress between layers. Still the behavior of plate under the variation of residual stress in different layers is unclear. To understand this behavior, Solution method for system of nonlinear PDE by Lie symmetry should be study and applied to this problem.

References:

1. Beléndez, T., C. Neipp, and A. Beléndez, *Large and small deflections of a cantilever beam.* European journal of physics, 2002. **23**: p. 371.
2. Olbrechts, B., et al., *Characterization of FD SOI devices and VCO's on thin dielectric membranes under pressure.* Solid State Electronics, 2007. **51**(9): p. 1229-1237.
3. Olbrechts, B., et al. *SOI Devices and Ring Oscillators on Thin Dielectric Membranes For Pressure Sensing Applications*. 2007.
4. Nayfeh, A.H. and B. Balachandran, *Applied nonlinear dynamics*. 1995: Wiley New York.
5. Reddy, J.N., *An introduction to nonlinear finite element analysis*. 2004: Oxford University Press, USA.
6. Holzapfel, G.A., *Nonlinear solid mechanics*. 2000: Wiley New York.
7. Ansys, I., *ANSYS Theoretical Manual.* Swanson Analysis Inc, 1986.
8. Bisshopp, K.E. and D. Drucker, *Large deflection of cantilever beams.* NOTES. **101**(3).
9. Ang Jr, M.H., W. Wei, and L. Teck-Seng. *On the estimation of the large deflection of a cantilever beam*. 1993.
10. Monasa, F. and G. Lewis, *Large deflections of point loaded cantilevers with nonlinear behaviour.* Zeitschrift für Angewandte Mathematik und Physik (ZAMP), 1983. **34**(1): p. 124-130.
11. Horr, A.M. and L.C. Schmidt, *Closed-form solution for the Timoshenko beam theory using a computer-based mathematical package.* Computers & Structures, 1995. **55**(3): p. 405-412.
12. Belendez, T., et al., *Numerical and experimental analysis of large deflections of cantilever beams under a combined load.* Physica scripta, 2005. **2005**: p. 61.
13. Al-Sadder, S. and R.A.O. Al-Rawi, *Finite difference scheme for large-deflection analysis of non-prismatic cantilever beams subjected to different types of continuous and discontinuous loadings.* Archive of Applied Mechanics, 2006. **75**(8): p. 459-473.
14. Knapp, J.A. and M.P. de Boer, *Mechanics of microcantilever beams subject to combined electrostatic and adhesive forces.* Journal of Microelectromechanical Systems, 2002. **11**(6): p. 754-764.
15. Kaajakari, V., et al. *Square-extensional mode single-crystal silicon micromechanical RF-resonator*. 2003.
16. Hirai, Y., M. Shindo, and Y. Tanaka. *Study of large bending and low voltage drive electrostatic actuator with novel shaped cantilever and electrode*. 1998: Institute of Electrical & Electronics Engineers (IEEE).
17. De Boer, M.P. and T.A. Michalske, *Accurate method for determining adhesion of cantilever beams.* Journal of Applied Physics, 1999. **86**: p. 817.
18. Mastrangelo, C.H. and C.H. Hsu. *A simple experimental technique for the measurement of the work of adhesion of microstructures*. 2002: IEEE.
19. Kaajakari, V., et al., *Nonlinear limits for single-crystal silicon microresonators.* Microelectromechanical Systems, Journal of, 2004. **13**(5): p. 715-724.
20. Liu, S., A. Davidson, and Q. Lin, *Simulation studies on nonlinear dynamics and chaos in a MEMS cantilever control system.* Journal of Micromechanics and Microengineering, 2004. **14**: p. 1064.

21. Petersen, K.E., *Dynamic micromechanics on silicon: techniques and devices.* IEEE Transactions on electron devices, 1978. **25**(10): p. 1241-1250.
22. Xie, W.C., H.P. Lee, and S.P. Lim, *Nonlinear dynamic analysis of MEMS switches by nonlinear modal analysis.* Nonlinear dynamics, 2003. **31**(3): p. 243-256.
23. Taylor, S.W. and S.C.B. Yau, *Boundary control of a rotating Timoshenko beam.* ANZIAM Journal, 2002. **44**.
24. Kaajakari, V., et al., *Nonlinear mechanical effects in silicon longitudinal mode beam resonators.* Sensors and Actuators A: Physical, 2005. **120**(1): p. 64-70.
25. Ishii, Y., T. Thümmel, and M. Horie, *Dynamic characteristic of miniature molding pantograph mechanisms for surface mount systems.* Microsystem Technologies, 2005. **11**(8): p. 991-996.
26. Takamatsu, H. and T. Sugiura, *Nonlinear Vibration of Electrostatic MEMS under DC and AC Applied Voltage.* 2005.
27. Lim, S.H., et al., *Design and fabrication of a novel bimorph microoptomechanical sensor.* Microelectromechanical Systems, Journal of, 2005. **14**(4): p. 683-690.
28. Lee, C.Y., et al., *Elastic–plastic modeling of heat-treated bimorph micro-cantilevers.* Microsystem Technologies, 2006. **12**(10): p. 979-986.
29. Chu, W.H., M. Mehregany, and R.L. Mullen, *Analysis of tip deflection and force of a bimetallic cantilever microactuator.* Journal of Micromechanics and Microengineering, 1993. **3**: p. 4.
30. Huang, C., Y.Y. Lin, and T.A. Tang, *Study on the tip-deflection of a piezoelectric bimorph cantilever in the static state.* Journal of Micromechanics and Microengineering, 2004. **14**: p. 530.
31. Lu, P. and K.H. Lee, *An alternative derivation of dynamic admittance matrix of piezoelectric cantilever bimorph.* Journal of Sound and Vibration, 2003. **266**(4): p. 723-735.
32. Cho, Y.H., et al., *Fabrication and optimization of bimorph micro probes for the measurement of individual biocells.* Microsystem Technologies, 2005. **12**(1): p. 30-37.
33. Peroulis, D. and L.P.B. Katehi, *Spring-loaded DC-contact RF MEMS switches.* International Journal of RF and Microwave Computer-Aided Engineering, 2004. **14**(4): p. 345-355.
34. Baykara, C., U. Guven, and I. Bayer, *Large deflections of a cantilever beam of nonlinear bimodulus material subjected to an end moment.* Journal of Reinforced Plastics and Composites, 2005. **24**(12): p. 1321-1326.
35. MichiganTechnologicalUniversity, *Strength of Sandwich Structures.* 2006.
36. Garcia, E. and N. Lobontiu, *Induced-strain multimorphs for microscale sensory actuation design.* Smart Materials and Structures, 2004. **13**: p. 725.
37. Argyrakis, P., et al., *Fabrication and characterization of a wind sensor for integration with a neuron circuit.* Microelectronic Engineering. **84**(5-8): p. 1749-1753.
38. Mortet, V., et al., *Diamond – Application to piezoelectric bimorph cantilever sensors.* physica status solidi (a), 2006. **203**(12): p. 3185-3190.
39. Napoli, M., B. Bamieh, and K. Turner. *Mathematical modeling, experimental validation and observer design for a capacitively actuated microcantilever*. 2005.

40. Al Aioubi, M.Y., et al., *Deflection and load characterisation of bimorph actuators for bioMEMS and other applications.* Microelectronic Engineering, 2004. **73-74**: p. 898-903.
41. Liew, L.A., A. Tuantranont, and V.M. Bright, *Modeling of thermal actuation in a bulk-micromachined CMOS micromirror.* Microelectronics Journal, 2000. **31**(9-10): p. 791-801.
42. Yang, J.P., X.C. Deng, and T.C. Chong, *An electro-thermal bimorph-based microactuator for precise track-positioning of optical disk drives.* Journal of Micromechanics and Microengineering, 2005. **15**: p. 958.
43. Pamula, V.K., A. Jog, and R.B. Fair. *Mechanical property measurement of thinfilm gold using thermally actuated bimetallic cantilever beams*. 2001.
44. Han, L.-H. and S. Chen, *Wireless bimorph micro-actuators by pulsed laser heating.* Sensors and Actuators A: Physical, 2005. **121**(1): p. 35-43.
45. Popa, D.O., et al. *Dynamic modeling and input shaping of thermal bimorph MEMS actuators*. 2003: IEEE.
46. Wang, D. and A.I. El-Sheikh, *Large-deflection mathematical analysis of rectangular plates.* Journal of Engineering Mechanics, 2005. **131**: p. 809.
47. Little, G.H., *Large deflections of rectangular plates with transverse edges remaining straight.* Computers & Structures, 1999. **71**(3): p. 353-357.
48. Little, G.H., *Efficient large deflection analysis of rectangular plates with general transverse form of displacement.* Computers & Structures, 1999. **71**(3): p. 333-352.
49. Civalek, O. and A. Yavas, *Large Deflection Static Analysis of Rectangular Plates On Two Parameter Elastic Foundations.* International Journal of Science & Technology, 2006. **1**(1): p. 43-50.
50. Xin-zhi, W., et al., *Unsymmetrical nonlinear bending problem of circular thin plate with variable thickness.* Applied Mathematics and Mechanics, 2005. **26**(4): p. 423-430.
51. Shen, H.S., *Nonlinear bending of simply supported rectangular Reissner-Mindlin plates under transverse and in-plane loads and resting on elastic foundations.* Engineering Structures, 2000. **22**(7): p. 847-856.
52. Shen, H.S., *Nonlinear analysis of simply supported Reissner-Mindlin plates subjected to lateral pressure and thermal loading and resting on two-parameter elastic foundations.* Engineering Structures, 2000. **22**(11): p. 1481-1493.
53. Kim, K.Y. and W. Sachse, *Nonlinear elastic equation of state of solids subjected to uniaxial homogeneous loading.* Journal of Materials Science, 2000. **35**(13): p. 3197-3205.
54. Bao, Z., et al., *Nonlinear vibrations of beams, strings, plates, and membranes without initial tension.* Journal of applied mechanics, 2004. **71**(4): p. 551-559.
55. Chen, R. and D.F. Baldwin, *Displacement Theory for Fixturing Design of Thin Flexible Circuit Board Assembly.* TRANSACTIONS-AMERICAN SOCIETY OF MECHANICAL ENGINEERS JOURNAL OF ELECTRONIC PACKAGING, 2001. **123**(4): p. 388-393.
56. Nayfeh, A.H., M.I. Younis, and E.M. Abdel-Rahman, *Dynamic pull-in phenomenon in MEMS resonators.* Nonlinear dynamics, 2007. **48**(1): p. 153-163.
57. Nayfeh, A.H. and M.I. Younis, *Dynamics of MEMS resonators under superharmonic and subharmonic excitations.* Journal of Micromechanics and Microengineering, 2005. **15**: p. 1840.

58. Vogl, G.W. and A.H. Nayfeh, *A reduced-order model for electrically actuated clamped circular plates.* Journal of Micromechanics and Microengineering, 2005. **15**: p. 684.
59. Mukherjee, S., et al., *Nonlinear mechanics of MEMS plates with a total Lagrangian approach.* Computers & Structures, 2005. **83**(10-11): p. 758-768.
60. Rinaldi, G., M. Packirisamy, and I. Stiharu, *Dynamic Synthesis of Microsystems Using the Segment Rayleigh–Ritz Method.* Microelectromechanical Systems, Journal of, 2008. **17**(6): p. 1468-1480.
61. Cao, D.Q., D. Liu, and C.H.T. Wang, *Nonlinear dynamic modelling for MEMS components via the Cosserat rod element approach.* Journal of Micromechanics and Microengineering, 2005. **15**: p. 1334.
62. Chen, J., et al., *Reduced-order modeling of weakly nonlinear MEMS devices with Taylor-series expansion and Arnoldi approach.* Microelectromechanical Systems, Journal of, 2004. **13**(3): p. 441-451.
63. Bushyager, N., B. McGarvey, and M.M. Tentzeris. *Adaptive numerical modeling of RF structures requiring the coupling of Maxwell's, mechanical, and solid-state equations*: Citeseer.
64. Hui, C.Y., J.L. Yeh, and N.C. Tien, *Calculation of electrostatic forces and torques in MEMS using path-independent integrals.* Journal of Micromechanics and Microengineering, 2000. **10**: p. 477.
65. Wittwer, J.W., T. Gomm, and L.L. Howell, *Surface micromachined force gauges: uncertainty and reliability.* Journal of Micromechanics and Microengineering, 2002. **12**: p. 13.
66. Pan, F., J. Kubby, and J. Chen, *Numerical simulation of fluid-structure interaction in a MEMS diaphragm drop ejector.* Journal of Micromechanics and Microengineering, 2002. **12**: p. 70.
67. Yan, D., A. Khajepour, and R. Mansour, *Modeling of two-hot-arm horizontal thermal actuator.* Journal of Micromechanics and Microengineering, 2003. **13**: p. 312.
68. Baskaran, R. and K.L. Turner, *Mechanical domain coupled mode parametric resonance and amplification in a torsional mode micro electro mechanical oscillator.* Journal of Micromechanics and Microengineering, 2003. **13**: p. 701.
69. Bao, M., et al., *Modified Reynolds' equation and analytical analysis of squeeze-film air damping of perforated structures.* Journal of Micromechanics and Microengineering, 2003. **13**: p. 795.
70. Yang, Y.J. and K.Y. Shen, *Nonlinear heat-transfer macromodeling for MEMS thermal devices.* Journal of Micromechanics and Microengineering, 2005. **15**: p. 408.
71. Yang, Y.J., S.Y. Cheng, and K.Y. Shen, *Macromodeling of coupled-domain MEMS devices with electrostatic and electrothermal effects.* Journal of Micromechanics and Microengineering, 2004. **14**: p. 1190.
72. Su, Y.C., J. Shah, and L. Lin, *Implementation and analysis of polymeric microstructure replication by micro injection molding.* Journal of Micromechanics and Microengineering, 2004. **14**: p. 415.
73. Yan, D., A. Khajepour, and R. Mansour, *Design and modeling of a MEMS bidirectional vertical thermal actuator.* Journal of Micromechanics and Microengineering, 2004. **14**: p. 841.

74. Brissaud, M., *Modelling of non-symmetric piezoelectric bimorphs.* Journal of Micromechanics and Microengineering, 2004. **14**: p. 1507.
75. Borucki, L.J., et al., *A theory of pad conditioning for chemical-mechanical polishing.* Journal of Engineering Mathematics, 2004. **50**(1): p. 1-24.
76. Wu, J. and L.R. Carley. *Table-based numerical macromodeling for MEMS devices*. 2001.
77. Avdeev, I.V. and M.R. Lovell, *Modeling in-plane misalignments in lateral combdrive transducers.* Journal of Micromechanics and Microengineering, 2003. **13**: p. 809.
78. Kuang, J.H. and C.J. Chen, *Dynamic characteristics of shaped micro-actuators solved using the differential quadrature method.* Journal of Micromechanics and Microengineering, 2004. **14**: p. 647.
79. Hon, Y.C., L. Ling, and K.M. Liew, *Numerical analysis of parameters in a laminated beam model by radial basis functions.* CMC Computers, Materials and Continua, 2005. **2**(1): p. 39-50.
80. Younes, *Investigation of the mechanical behaviors of microbeam-base MEMS devices*, in *Mechanical Engineerig*. 2001, Virginia Polytechnic Institute: Virginia.
81. Zhou, S.A., *On forces in microelectromechanical systems.* International Journal of Engineering Science, 2003. **41**(3-5): p. 313-335.
82. Hu, Y.C., C.M. Chang, and S.C. Huang, *Some design considerations on the electrostatically actuated microstructures.* Sensors and Actuators A: Physical, 2004. **112**(1): p. 155-161.
83. Sasayama, T., et al., *Highly reliable silicon micromachined physical sensors in mass production.* Sensors and Actuators A: Physical, 1996. **54**(1-3): p. 714-717.
84. Lee, S., et al., *Reliability testing of flexible printed circuit-based RF MEMS capacitive switches.* Microelectronics Reliability, 2004. **44**(2): p. 245-250.
85. McCarthy, B., et al., *A dynamic model, including contact bounce, of an electrostatically actuated microswitch.* Microelectromechanical Systems, Journal of, 2002. **11**(3): p. 276-283.
86. Millet, O., et al., *Electrostatic actuated micro gripper using an amplification mechanism.* Sensors and Actuators A: Physical, 2004. **114**(2-3): p. 371-378.
87. Schiele, I., et al., *Surface-micromachined electrostatic microrelay.* Sensors and Actuators A: Physical, 1998. **66**(1-3): p. 345-354.
88. Megregany, M., et al. *Operation of microfabricated harmonic and ordinary side-drive motors*. 2002: IEEE.
89. Guckel, H., et al. *A first functional current excited planar rotational magnetic micromotor*. 2002: IEEE.
90. Hung, E.S. and S.D. Senturia, *Extending the travel range of analog-tuned electrostatic actuators.* Microelectromechanical Systems, Journal of, 2002. **8**(4): p. 497-505.
91. Zhang, W.M. and G. Meng, *Nonlinear dynamic analysis of electrostatically actuated resonant MEMS sensors under parametric excitation.* Sensors Journal, IEEE, 2007. **7**(3): p. 370-380.
92. Castaner, L.M. and S.D. Senturia, *Speed-energy optimization of electrostatic actuators based on pull-in.* Microelectromechanical Systems, Journal of, 2002. **8**(3): p. 290-298.

93. Casta er, L., et al., *Pull-in time-energy product of electrostatic actuators: comparison of experiments with simulation.* Sensors and Actuators A: Physical, 2000. **83**(1-3): p. 263-269.
94. Osterberg, P.M. and S.D. Senturia, *M-TEST: A test chip for MEMS material property measurement using electrostatically actuated test structures.* Microelectromechanical Systems, Journal of, 2002. **6**(2): p. 107-118.
95. Quévy, E., et al., *Large stroke actuation of continuous membrane for adaptive optics by 3D self-assembled microplates.* Sensors and Actuators A: Physical, 2002. **95**(2-3): p. 183-195.
96. Nadal-Guardia, R., et al., *Current drive methods to extend the range of travel of electrostatic microactuators beyond the voltage pull-in point.* Microelectromechanical Systems, Journal of, 2002. **11**(3): p. 255-263.
97. Chan, E.K. and R.W. Dutton, *Electrostatic micromechanical actuator with extended range of travel.* Microelectromechanical Systems, Journal of, 2002. **9**(3): p. 321-328.
98. Legtenberg, R., et al., *Electrostatic curved electrode actuators.* Microelectromechanical Systems, Journal of, 2002. **6**(3): p. 257-265.
99. Tang, W.C., M.G. Lim, and R.T. Howe, *Electrostatic comb drive levitation and control method.* Journal of Microelectromechanical Systems, 1992. **1**(4): p. 170-178.
100. Wenjing, Y., S. Mukherjee, and N.C. MacDonald, *Optimal shape design of an electrostatic comb drive in microelectromechanical systems.* Microelectromechanical Systems, Journal of, 1998. **7**(1): p. 16-26.
101. Busta, H., et al., *A MEMS shield structure for controlling pull-in forces and obtaining increased pull-in voltages.* Journal of Micromechanics and Microengineering, 2001. **11**: p. 720.
102. Zhang, W. and G. Meng, *Nonlinear dynamical system of micro-cantilever under combined parametric and forcing excitations in MEMS.* Sensors and Actuators A: Physical, 2005. **119**(2): p. 291-299.
103. Liu, S., A. Davidson, and Q. Lin. *Simulating nonlinear dynamics and chaos in a MEMS cantilever using Poincare mapping*. 2003: IEEE.
104. Adams, S.G., et al., *Independent tuning of linear and nonlinear stiffness coefficients [actuators]*. Microelectromechanical Systems, Journal of, 2002. **7**(2): p. 172-180.
105. Zhang, W., R. Baskaran, and K.L. Turner, *Effect of cubic nonlinearity on auto-parametrically amplified resonant MEMS mass sensor.* Sensors and Actuators A: Physical, 2002. **102**(1-2): p. 139-150.
106. Li, G. and N.R. Aluru, *Linear, nonlinear and mixed-regime analysis of electrostatic MEMS.* Sensors and Actuators A: Physical, 2001. **91**(3): p. 278-291.
107. Senturia, S.D., et al., *A computer-aided design system for microelectromechanical systems (MEMCAD).* Microelectromechanical Systems, Journal of, 2002. **1**(1): p. 3-13.
108. Aluru, N.R. and J. White, *An efficient numerical technique for electrochemical simulation of complicated microelectromechanical structures* 1.* Sensors and Actuators A: Physical, 1997. **58**(1): p. 1-11.
109. Younis, M.I., E.M. Abdel-Rahman, and A. Nayfeh, *A reduced-order model for electrically actuated microbeam-based MEMS.* Microelectromechanical Systems, Journal of, 2003. **12**(5): p. 672-680.

110. Li, G.Y. and L. Wang, *Influence of bonding parameters on electrostatic force in anodic wafer bonding.* Thin Solid Films, 2004. **462**: p. 334-338.
111. Thomson, W., *Theory of vibration with applications*. 2004: Taylor & Francis.
112. Pamidighantam, S., et al., *Pull-in voltage analysis of electrostatically actuated beam structures with fixed–fixed and fixed–free end conditions.* Journal of Micromechanics and Microengineering, 2002. **12**: p. 458.
113. Cantwell, B.J. and T.H. Moulden, *Introduction to symmetry analysis.* Applied Mechanics Reviews, 2004. **57**: p. B4.
114. Hydon, P.E., *Symmetry methods for differential equations: a beginner's guide*. 2000: Cambridge Univ Pr.
115. Emanuel, G., *Solution of ordinary differential equations by continuous groups*. 2001: CRC Press.
116. Bluman, G.W. and S. Kumei, *Symmetries and differential equations.* 1989.
117. Cheb-Terrab, E.S., L.G.S. Duarte, and L. Da Mota, *Computer algebra solving of first order ODEs using symmetry methods.* Computer Physics Communications, 1997. **101**(3): p. 254-268.
118. Baumann, G., *Symmetry analysis of differential equations with Mathematica.* Mathematical and computer modelling, 1997. **25**(8-9): p. 25-37.
119. Cheb-Terrab, E.S., L.G.S. Duarte, and L. Da Mota, *Computer algebra solving of second order ODEs using symmetry methods.* Computer Physics Communications, 1998. **108**(1): p. 90-114.
120. Olver, P.J., *Applications of Lie groups to differential equations*. 2000: Springer Verlag.
121. Bluman, G.W. and S.C. Anco, *Symmetry and integration methods for differential equations*. 2002: Springer Verlag.
122. Stephani, H. and M.A.H. MacCallum, *Differential equations: their solution using symmetries*. 1989: Cambridge Univ Pr.
123. Roark, R.J., et al., *Roark's formulas for stress and strain*. 2002: McGraw-Hill New York.
124. Rinaldi, G., M. Packirisamy, and I. Stiharu, *Dynamic testing of micromechanical structures under thermo-electro-mechanical influences.* Measurement, 2007. **40**(6): p. 563-574.
125. Zhang, W.M., G. Meng, and D. Chen, *Stability, nonlinearity and reliability of electrostatically actuated MEMS devices.* Sensors, 2007. **7**(5): p. 760-796.
126. Liu, C., *Foundations of MEMS*. 2006: Pearson/Prentice Hall.
127. Rinaldi, G., *Dynamic Analysis and Validation of Cantilever MEMS subjected to Electro-Thermo-Mechanical influences*, in *MIE*. 2007, Concordia University: Montreal. p. 301.
128. Wang, T.M., S.L. Lee, and O.C. Zienkiewicz, *A numerical analysis of large deflections of beams.* International Journal of Mechanical Sciences, 1961. **3**(3): p. 219-228.
129. Kemper, J.D., *Large deflections of tapered cantilever beams.* International Journal of Mechanical Sciences, 1968. **10**(6): p. 469-478.
130. Lewis, G. and F. Monasa, *Large deflections of cantilever beams of non-linear materials of the Ludwick type subjected to an end moment.* International Journal of Non-Linear Mechanics, 1982. **17**(1): p. 1-6.

131. Lee, K., *Large deflections of cantilever beams of non-linear elastic material under a combined loading.* International Journal of Non-Linear Mechanics, 2002. **37**(3): p. 439-443.
132. Dado, M. and S. Al-Sadder, *A new technique for large deflection analysis of non-prismatic cantilever beams.* Mechanics Research Communications, 2005. **32**(6): p. 692-703.
133. Wang, J., J.K. Chen, and S. Liao, *An explicit solution of the large deformation of a cantilever beam under point load at the free tip.* Journal of Computational and Applied Mathematics, 2008. **212**(2): p. 320-330.
134. Shvartsman, B.S., *Large deflections of a cantilever beam subjected to a follower force.* Journal of Sound and Vibration, 2007. **304**(3-5): p. 969-973.
135. Olver, P.J., *Equivalence, invariants, and symmetry*. 1995: Cambridge Univ Pr.
136. Banerjee, A., B. Bhattacharya, and A.K. Mallik, *Large deflection of cantilever beams with geometric non-linearity: Analytical and numerical approaches.* International Journal of Non-Linear Mechanics, 2008. **43**(5): p. 366-376.
137. Chia, C.Y., *Nonlinear analysis of plates*. 1980: McGraw-Hill Inc., US.
138. Ugural, A.C., *Stresses in plates and shells*. 1981: McGraw-Hill New York.
139. Kármán, T.v., *Festigkeitsprobleme in Maschinenbau.* Encyklopädie der Mathematischen Wissenschaften, 1910. **4**(4): p. 348-352.
140. http://en.wikipedia.org/wiki/Finite_element_method. *Finite element method*. 12-31-2010 12-31-2010 [cited.
141. Reddy, J.N., *Mechanics of laminated composite plates and shells: theory and analysis*. 2004: CRC.
142. Petit, P.H. and M.E. Waddoups, *A method of predicting the nonlinear behavior of laminated composites.* Journal of Composite Materials, 1969. **3**(1): p. 2.
143. Hahn, H.T., *Nonlinear behavior of laminated composites(Nonlinear tension and buckling stress behavior of angle ply unidirectional laminated composites).* Journal of Composite Materials, 1973. **7**: p. 257-271.
144. Noor, A.K., W.S. Burton, and J.M. Peters, *Assessment of computational models for multilayered composite cylinders.* International Journal of Solids and Structures, 1991. **27**(10): p. 1269-1286.
145. Townsend, P.H., D.M. Barnett, and T.A. Brunner, *Elastic relationships in layered composite media with approximation for the case of thin films on a thick substrate.* Journal of Applied Physics, 1987. **62**: p. 4438.
146. Icardi, U. and M. Di Sciuva, *Large-deflection and stress analysis of multilayered plates with induced-strain actuators.* Smart Materials and Structures, 1996. **5**: p. 140-164.
147. Jatlaoui, M.M., P. Pons, and H. Aubert. *Pressure micro-sensor based on Radio-Frequency transducer*. 2008: IEEE.
148. Jin, J. and Z. Zhou. *Simulation and Modeling of Micro Pressure Sensor Array*. 2002.
149. Kovács, A., M. Pogány, and U. Mescheder, *Mechanical investigation of perforated and porous membranes for micro-and nanofilter applications.* Sensors and Actuators B: Chemical, 2007. **127**(1): p. 120-125.
150. Charavel, R., B. Olbrechts, and J.P. Raskin. *Stress release of PECVD oxide by RTA*. 2003.
151. Ganji, B.A. and B.Y. Majlis. *Modeling of diaphragms for micromachined condenser microphones*. 2006: IEEE.

152. Ganji, B.A. and B.Y. Majlis. *The Effect of Design Parameters on Static and Dynamic Behaviors of the MEMS Microphone*. 2007: IEEE.
153. Ngo, H.D., et al. *Corner rounding to strengthen silicon pressure sensors using DRIE*. 2008: IEEE.
154. Ko, H.S., C.W. Liu, and C. Gau. *A Novel Fabrication for Pressure Sensor with Polymer Material and Its Characteristic Testing*. 2007: IEEE.
155. Belavic, D., et al. *PZT thick films for pressure sensors: Characterisation of materials and devices*. 2008: IEEE.
156. Janssen, G.C.A.M., et al., *Celebrating the 100 th anniversary of the Stoney equation for film stress: Developments from polycrystalline steel strips to single crystal silicon wafers.* Thin Solid Films, 2009. **517**(6): p. 1858-67.
157. Kim, J.S., K.W. Paik, and S.H. Oh, *The multilayer-modified Stoney's formula for laminated polymer composites on a silicon substrate.* Journal of Applied Physics, 1999. **86**: p. 5474.
158. Kim, J.S., et al. *Thermo-mechanical stresses in laminated polymer films on silicon substrates*. 2002: IEEE.
159. Berry, B.S. and W.C. Pritchet, *Internal stress and internal friction in thin‐layer microelectronic materials.* Journal of Applied Physics, 1990. **67**(8): p. 3661-3668.
160. Chiou, J.A. and S. Chen, *Thermal hysteresis analysis of MEMS pressure sensors.* Microelectromechanical Systems, Journal of, 2005. **14**(4): p. 782-787.
161. Ghasemi, M.N., C. Pan, and H. Feng, *Intrinsic strain modeling and residual stress analysis for thin-film processing of layered structures.* Journal of Electronic Packaging, 2003. **125**: p. 4.
162. Huang, S. and X. Zhang, *Extension of the Stoney formula for film--substrate systems with gradient stress for MEMS applications.* Journal of Micromechanics and Microengineering, 2006. **16**: p. 382-389.
163. Klein, C.A., *How accurate are Stoney's equation and recent modifications.* Journal of Applied Physics, 2000. **88**: p. 5487.
164. N.Schwarzer, F.R., *on the determination of film stress from substrate bending: Storey's formula and its limits.* TU Chemnitz, Faculty of Science 2006.
165. Prof, C.B.A., *Thermomechanical Stress Analysis of Multi-Layered Electronic Packaging.* Journal of Electronic Packaging, 2003. **125**: p. 134.
166. Heller, R.A., *Interlaminar shear stress in sandwich beams.* Experimental Mechanics, 1969. **9**(9): p. 413-418.
167. Asme, M., C. Pan, and H. Feng, *Intrinsic strain modeling and residual stress analysis for thin-film processing of layered structures.* Journal of Electronic Packaging, 2003. **125**: p. 4.
168. Campbell, S.A., *Fabrication engineering at the micro and-nanoscale*: University Press.
169. Zhang, X.C., et al., *Error analyses on some typically approximate solutions of residual stress within a thin film on a substrate.* Journal of Applied Physics, 2005. **98**: p. 053516.
170. Jahn, J., *Introduction to the theory of nonlinear optimization*. 2007: Springer Verlag.

APPENDICES

Appendix A:

Failure of numerical method for solving the ODE

Below, an example to prove the lack of solution for a practical problem is presented. For the micro-cantilever beam which is studied in the second chapter and has the property below:

$$m = 1.84 \times 10^{-11}[Kg], \xi = 0.1, k = 0.85[\frac{N}{m}], \omega_n = 4.3551 \times 10^5 [\frac{Rad}{Sec}]$$
$$g = 4.0 \times 10^{-6}[m], V_0 = 1.0[V], A = 4 \times 10^{-9}[m^2]$$

The equation (2.3) can be written as:

$$\frac{d^2 y(t)}{dt^2} + 87102.67140 \frac{dy(t)}{dt} + 1.8967188411 \times 10^{11} y(t) = \frac{9.619565215 \times 10^{-10}}{(4 \times 10^{-6} - y(t))^2} \qquad \text{(A.1)}$$

The research revealed that any kind of numerical solution using Maple module for ODE could not solve this specific equation. Table (A-1) shows these results. As one can see in the cases that y values are same y' values are not equal. Each solution was done for three different tolerances, $10^{-7}, 10^{-10}, 10^{-14}$ respectively. However, lsode algorithm provided a good result to this specific problem.

Table A-2. Illustration of the solution availability for equation (A.1) using Maple solving models for ODE

Method of solution	y	y'
Runge-Kutta 4-5th order	Fail/Fail/Fail	Fail/Fail/Fail
Dverk interpolation	.317030720e-9/=/Fail	-.7449807e-6/.64462e-17/Fail
Dverk pair	.31703339e-9/=/Fail	.23652e-9/.674977e-11/Fail
Gear single step rational/polynomial	Fail/Fail/Fail	Fail/Fail/Fail
Rosenbrock stiff	.31703072e-9/=/=	-.374454e-25/-.12698e-31/.108e-34
Livermore Adams Jacobian	.31703072e-9/=/=	.299e-23/-.2573e-24/-.1421e-25
Adam iterative	Fail/Fail/Fail	Fail/Fail/Fail
Adams diagonal	Fail/Fail/Fail	Fail/Fail/Fail
BDF iterative	Fail/Fail/Fail	Fail/Fail/Fail
BDF Jacobean	Fail/.31703e-9/=	Fail/-.7818e-25/-.825e-25
BDF diagonal	Fail/Fail/Fail	Fail/Fail/Fail
Taylor Lazy/dsolve	Fail/Fail/Fail	Fail/Fail/Fail
BDF implicit	.31703e-9	.659e-81
Fixed step method	Fail/Fail/Fail	Fail/Fail/Fail

Appendix B:

Method of calculating C_i coefficients in (2.24) for equation (2.20):

By expanding (2.25) one has:

$$\begin{aligned}&\alpha C_6 y' - 2C_2\alpha y' - 3\alpha C_3 y'^2 + \beta C_6 y - 2\beta C_2 y - 3\beta C_3 yy' = \\ &\beta C_4 + \beta C_5 x + \beta C_6 y + \alpha C_2 + \alpha C_6 y' - \alpha C_2 y' - \alpha C_3 y'^2\end{aligned} \tag{B.1}$$

Coefficients of y'^2 in left hand and right hand must be equal:

$$-3C_3\alpha = -C_3\alpha \tag{B.2}$$

therefore:

$$C_3 = 0 \tag{B.3}$$

As above, coefficients of y' in left hand and right hand must be equal:

$$\alpha C_6 - 2\alpha C_2 - 3\beta C_2 = \alpha C_6 - \alpha C_2 \tag{B.4}$$

Simplifying it gives:

$$-C_2\alpha - 3C_2\beta = 0 \tag{B.5}$$

$$C_2 = 0 \tag{B.6}$$

Coefficients of x in left hand and right hand must be equal:

$$C_5 = 0 \tag{B.7}$$

By considering (B.3), (B.6) and (B.7) equation (B.1) becomes:

$$\beta C_6 y = \beta C_4 + \beta C_6 y \tag{B.8}$$

So:

$$C_4 = 0 \tag{B.9}$$

Appendix C:

Contact form for equation (2.53)[120]:

Generally if (x,u) and $(y=u, w=x)$. One can write :

$$w_y = \frac{dw}{dy} \tag{C.1}$$

or:

$$dw - w_y dy = dx - w_y du = -w_y(du - \frac{1}{w_y} dx) = 0 \tag{C.2}$$

therefore:

$$u_x = \frac{1}{w_y} \quad \text{or} \quad w_y = \frac{1}{u_x} \tag{C.3}$$

For second derivative:

$$w_{yy} = \frac{dw_y}{dy} \tag{C.4}$$

$$dw_y - w_{yy}dy = -\frac{1}{u_x^2}du_x - w_{yy}du \tag{C.5}$$

therefore:

$$dw_y - w_{yy}dy = -\frac{1}{u_x^2}(du_x + w_{yy}u_x^3 dx) - w_{yy}(du - u_x dx) \tag{C.6}$$

For $w_{xx} = \frac{du_x}{dx}$, one can write:

$$du_x - u_{xx}dx = 0 \tag{C.7}$$

By comparing the first parenthesis of (C.6) with (C.7):

$$u_{xx} = -w_{yy}u_x^3 \tag{C.8}$$

or:

$$u_{xx} = -\frac{w_{yy}}{w_y^3} \tag{C.9}$$

By substituting of y, t, r, v in equation (2.53) with u, x, y, w in equation (C.9), one will reach the equation (2.3).

Appendix D:

In this part, it is shown that a transformation like (2.24) doesn't give a symmetric for equation (2.55).A transformation like (2.24) has to satisfy (2.16), as it is shown in section 2.3.4. $\omega(r, v(r))$ in equation (2.16) is defined as:

$$\omega(r,v) = 2\xi\omega_n v^2 + (\omega_n{}^2 r - \frac{\varepsilon_0 A V^2}{2(r-g)^2 m})v^3 \tag{D.1}$$

If one substitute (2.24) and (D.1) in (2.16), will have:

$$\begin{aligned}
&-\frac{1}{(g-r)^4}(4c_3\xi^2\omega_n^2v^4g^4 + 4c_3\xi\omega_n^3v^5r^5 - 12c_4\omega_n^2v^2r^4g + 18c_4\omega_n^2v^2r^3g^2 \\
&-12c_4\omega_n^2v^2r^2g^3 + 3c_4\omega_n^2v^2rg^4 + 6c_4v^2rg\frac{\varepsilon_0AV^2}{2m} \\
&-12c_5\omega_n^2v^2r^5g + 18c_5\omega_n^2v^2r^4g^2 - 12c_5\omega_n^2v^2r^3g^3 + 3c_5\omega_n^2v^2r^2g^4 \\
&+6c_5v^2r^2g\frac{\varepsilon_0AV^2}{2m} - 3c_5v^2rg^2\frac{\varepsilon_0AV^2}{2m} + 6c_1\omega_n^2v^3r^2g^2 \\
&-4c_1\omega_n^2v^3rg^3 - 4c_3\omega_n^2v^4r^3g + 6c_3\omega_n^2v^4r^2g^2 - 4c_3\omega_n^2v^4rg^3 + ...) = 0
\end{aligned} \tag{D.2}$$

Any set of $C_i's$ doesn't satisfy (D-2). For example even if one considers the simple transformation like (2.49), equation (D-2) will simplify to:

$$\frac{v^3(\omega_n^2r^3 - 3\omega_n^2r^2g + 3\omega_n^2rg^2 - \omega_n^2g^3 + 2\frac{\varepsilon_0AV^2}{2m})}{(-r+g)^3} \tag{D.3}$$

which is non-zero.

Appendix E:

Definitions and theorems

Group:

A group is an ordered pair $(G,\times)$ such that G is a set, $\times$ is an associative binary operation on G, and $\exists e \in G$ such that:

a) if $a \in G$, then $a \times e = a$

b) is $a \in G$, then $\exists a^{-1} \in G$ such that $a \times a^{-1} = e$.

Manifold:

Let $k > 0$. Suppose that M is a subspace of R^n having the following property: for each $p \in M$, there is a set V containing p that is open in M, a set U that is open in R^k, and a continuous map $\alpha : U \to V$ carrying U onto V in a one-to-one fashion, such that:

a) α is of class C^r.

b) $\alpha^{-1} : U \to V$ is continuous.

c) $D\alpha(x)$ has rank k for each $x \in U$.

Then M is called a k-manifold without boundary in R^n, of class C^r. The map α is called a coordinate patch on M about p.

r-parameters Lie group :

An r-parameter Lie group is a group G which also carries the structure of an R-dimensional smooth manifold in such a way that both the group operation:

$$m: G \times G \to G, m(h,h) = g \times h, \quad g,h \in G \tag{E.1}$$

and the inversion

$$i: G \to G, \; i(G) = g^{-1} \quad g \in G \tag{E.2}$$

are smooth maps between manifolds.

Local group of transformations:

A transformation group acting on a smooth manifold M is determined by a Lie group G and smooth map $\phi: G \times M \to M$ denoted by $\phi(g,x)g.x$, which satisfies

$$e.x = x \;\; g.(h.x) = (g.h).x \;\; for \;\; \forall x \in M, \quad \forall g,h \in G \tag{E.3}$$

Tangent vector:

C is a smooth curve on a manifold M, parameterized by $\phi: I \to M$, where I is a subinterval of R. In local coordinates $x = (x^1, ..., x^m)$, C is given by m smooth functions $\phi(\varepsilon) = (\phi^1(\varepsilon), ..., \phi^m(\varepsilon))$ of the real variable ε. At each point $x = \phi(\varepsilon)$ of C the curve has a tangent vector, namely the derivative

$$\dot{\phi}(\varepsilon) = \frac{d\phi}{d\varepsilon} = (\dot{\phi}^1(\varepsilon), ..., \dot{\phi}^m(\varepsilon)) \tag{E.4}$$

Tangent space:

A tangent vector to a manifold M at a point $x \in M$ is geometrically defined by the tangent to a (smooth) curve passing through x

Vector field:

A vector field v on M assigns a tangent vector $v|_x \in TM|_x$ to each point $x \in M$, with $v|_x$ varying smoothly from point to point. In local coordinates $x = (x^1, ..., x^m)$, a vector field has the form

$$v|_x = \xi^1(x)\frac{\partial}{\partial x^1} + ... + \xi^m(x)\frac{\partial^m}{\partial x^m} \tag{E.5}$$

where each $\xi^i(x)$ is a smooth function of x.

Flows:

If v is a vector field, we denote the parameterized maximal integral curve passing through x in M by $\Psi(e,x)$ and call Ψ the flow generated by v.

Infinitesimal generator:

The flow generated by a vector field is the same as a local group action of the Lie group R on the manifold M is often called a one-parameter group of transformations. The vector field v is called the infinitesimal generator of the action since by Taylor's theorem, in local coordinates:

$$\Psi(\varepsilon,x)=x+\varepsilon\xi(x)+O(\varepsilon^2) \tag{E.6}$$

where $\xi=(\xi^i,...,\xi^m)$ are the coefficients of v. If $\Psi(\varepsilon,x)$ is any one-parameter group of transformations acting on M, then its infinitesimal generator is obtained by:

$$\left.\frac{d}{d\varepsilon}\right|_{\varepsilon=0}\Psi(\varepsilon,x) \tag{E.7}$$

Symmetry group:

A group G is called a symmetry group of a system of k equations

$$F_1(x)=\cdots=F_k(x)=0 \tag{E.8}$$

if and only if the variety $S_F = \{x | F_1(x) = \cdots = F_k(x) = 0\}$ is a *G*-invariant subset of *M*.

Invariant function:

G is a local group of transformations acting on a manifold *M*. A function $F: M \to N$, where *N* is another manifold, is called a *G*-invariant function if for all $x \in M$ and all $g \in G$ such that $x.g$ is defined:

$$F(g.x) = F(x) \tag{E.9}$$

Invariant function:

If G acts on M, and $F: M \to R^1$ is a smooth function, then *F* is a *G*-invariant function if and only if every level set $\{F(x) = c\}, c \in R^l$ is a G-invariant subset of M.

Invariant of differential equation:

Let φ be a system of differential equations. A symmetry group of the system φ is a local group of transformations G acting on an open subset M of the space of independent and dependent variables for the system with the property that whenever $u = f(x)$ is a

solution of φ, and whenever $g.f$ is defined for $g \in G$, then $u = g.f(x)$ is also a solution of the system.

Prolongation:

Any diffeomorphism,

$$\Gamma : (x, y, y', ..., y^{(n)}) \mapsto (\hat{x}, \hat{y}, \hat{y}', .., \hat{y}^{(n)}) \tag{E.10}$$

acting on the plane ,where

$$\hat{y}^{(k)} = \frac{d^{(k)}\hat{y}}{d\hat{x}^k} \quad \text{k=1,…,n.} \tag{E.11}$$

This mapping is called n^{th} prolongation of Γ.

Canonical coordinate:

A change of coordinates:

$$y = Y(x) = (y_1(x), y_2(x), ..., y_n(x)) \tag{E.12}$$

defines a set of canonical coordinates for the one-parameter Lie group of transformations $x^* = X(x, \varepsilon)$ if in terms of such coordinates the group $x^* = X(x, \varepsilon)$ becomes:

$$y_i^* = y_i \qquad i = 1,2,...,n-1$$

$$y_n^* = y_n + \varepsilon \tag{E.13}$$

Theorem for reduction of order of an ODE:

Assume that the nontrivial one-parameter Lie group transformations

$$\begin{aligned} x^* &= X(x,y;\varepsilon) = x + \varepsilon\xi(x,y) + O(\varepsilon^2) \\ y^* &= Y(x,y;\varepsilon) = y + \varepsilon\eta(x,y) + O(\varepsilon^2) \end{aligned} \tag{E.14}$$

with infinitesimal generator

$$Xf = \xi(x,y)\frac{\partial f}{\partial x} + \eta(x,y)\frac{\partial f}{\partial y} \tag{E.15}$$

is admitted by the nth order ODE:

$$y^{(n)} = f(x,y,y',...,y^{(n-1)}) \quad n \geq 2 \tag{E.16}$$

Let $(r(x,y), s(x,y))$ be corresponding canonical coordinates satisfying $Xr = 0$, $Xs = 1$.

Then solving the nth order ODE reduces to solving an (n-1) order ODE:

$$\frac{d^{n-1}z}{dr^{n-1}} = G(r, z, \frac{dz}{dr}, ..., \frac{d^{n-2}z}{dr^{n-2}}) \tag{E.17}$$

where:

$$\frac{ds}{dr} = z \tag{E.18}$$

Suppose that Lie symmetry of a first order ODE $y' = \omega(x, y)$ is given, and then the ODE can be reduced to quadrature by rewriting it in terms of canonical coordinates as fallow:

$$\frac{ds}{dr} = \frac{s_x + \omega(x, y)s_y}{r_x + \omega(x, y)r_y} \tag{E.19}$$

the ODE (E.19) is of the form:

$$\frac{ds}{dr} = \Omega(r) \tag{E.20}$$